Universitat Politècnica de Catalunya

PhD program in Photonics

Nonlinear optics with a Rydberg ensemble for quantum information processing purposes

---

Author:
Jan Lowinski

Supervisor:
Prof. Dr. Hugues de Riedmatten

A thesis submitted to obtain the title of Doctor
by the Universitat Politècnica de Catalunya

in the

QPSA – Quantum Photonics with Solids and Atoms *group,*
ICFO – The Institute of Photonic Sciences

November 10, 2023

UNIVERSITAT POLITÈCNICA DE CATALUNYA
BARCELONATECH

ICFO

Abstract

Photons have emerged as the main candidates for carrying quantum information due to their weak interaction with the environment. Unfortunately, their limited interaction with one another poses challenges for photonic quantum information processing. One of the possible solutions lies in the unique behavior of interacting Rydberg excitations in cold atomic ensembles, where strong nonlinearities enable engineering interactions among individual photons. This phenomenon makes Rydberg ensembles a promising platform for quantum information applications, notably in long-distance quantum communication. This thesis presents a series of experiments that explore and exploit Rydberg-mediated interactions, all with the long-term objective of building an efficient quantum repeater.

The thesis begins with a concise theory overview of Rydberg and ensemble physics. This is followed by an explanation of the experimental setup. I discuss how, building upon a previously existing setup, we improved the stability and spectral properties of our laser system, along with enhancing the quality of the atomic ensemble. A comprehensive modification to the laser locking system was implemented by adopting a drift-resistant spectroscopy technique together with a transfer cavity. Simultaneously, thanks to the introduction of a crossed dipole trap, we increased of the atomic ensemble's density while reducing its physical size. The introductory section of the thesis concludes with a description of two different single-photon generation methods and an in-depth review of various decoherence mechanisms impacting Rydberg ensemble excitations. The single-photon generation performance has been improved by the modifications implemented in the setup, resulting in higher generation rates and better single-photon purity. Supported by experimental data and a careful analysis of experimental parameters, we identify the most probable sources of significant decoherence and suggest potential strategies for mitigation.

In our initial experiment, we achieve the storage and subsequent retrieval of an on-demand single photon. This photon is generated through the collective excitation of Rydberg states in one cold atomic ensemble, and it is stored in a low-noise Raman quantum memory situated in another cold atomic ensemble. Our results show the capability to store and retrieve these single photons while maintaining a high signal-to-noise ratio of up to 26 and preserving strong antibunching characteristics. We also explore the built-in temporal beam splitting capabilities of the Raman memory

and successfully use the memory to control the single photon waveshape.

In the second experiment, we demonstrate for the first time an interaction and storage of single photons in a highly non-linear medium based on cold Rydberg atoms. We employ the DLCZ protocol in a cold atomic ensemble to create single photons, guiding them to another ensemble for storage in a highly excited Rydberg state under conditions of electromagnetically induced transparency. By studying the statistics of the light retrieved from the Rydberg atoms, we show for the first time single-photon filtering with non-classical input light. Moreover, through Monte Carlo simulation, we get an intuitive understanding of the effect of the (partial) Rydberg blockade upon the Fock state distribution of arbitrary input light pulses. This allows us to conclude that the response of the medium is determined by the input Fock state distribution, what confirms the established understanding of Rydberg ensemble nonlinearity. This demonstration can be seen as a step towards realization of deterministic photon-photon gates based on Rydberg ensembles with single photon inputs.

The results presented in this thesis affirm the potential of Rydberg ensembles to become central elements of future quantum networks, both as single photon sources and processing nodes. Furthermore, auxiliary outcomes provide an additional understanding of the Rydberg ensemble physics and offer insight into limitations that we need to overcome to improve further our setup.

Resum

Els fotons han sorgit com els principals candidats per transportar informació quàntica a causa de la seva feble interacció amb el medi ambient. Malauradament, la seva interacció limitada entre ells planteja reptes per al processament de la informació quàntica fotònica. Una de les possibles solucions rau en el comportament únic de les excitacions de Rydberg interactuants en conjunts atòmics freds, on les fortes no linealitats permeten interaccions d'enginyeria entre fotons individuals. Aquest fenomen fa que els conjunts de Rydberg siguin una plataforma prometedora per a aplicacions d'informació quàntica, especialment en la comunicació quàntica de llarga distància. Aquesta tesi presenta una sèrie d'experiments que exploren i exploten les interaccions mediades per Rydberg, tots amb l'objectiu a llarg termini de construir un repetidor quàntic eficient.

La tesi comença amb una visió general concisa de la teoria de Rydberg i la física de conjunts atòmics. Tot seguit s'explica la configuració experimental. Parlo de com, a partir d'una configuració existent anteriorment, hem millorat l'estabilitat i les propietats espectrals del nostre sistema làser, juntament amb la millora de la qualitat del conjunt atòmic. Es va implementar una modificació integral del sistema de bloqueig làser mitjançant l'adopció d'una tècnica d'espectroscòpia resistent al desviament juntament amb una cavitat de transferència. Simultàniament, gràcies a la introducció d'una trampa de dipols creuats, vam augmentar la densitat del conjunt atòmic alhora que vam reduir la seva mida física. La secció introductòria de la tesi conclou amb una descripció de dos mètodes diferents de generació de fotons únics i una revisió en profunditat de diversos mecanismes de decoherència que afecten les excitacions del conjunt de Rydberg. El rendiment de la generació de fotons únics s'ha millorat amb les modificacions implementades a la configuració, donant lloc a taxes de generació més altes i una millor puresa dels fotons únics. Amb el suport de dades experimentals i una anàlisi acurada dels paràmetres experimentals, identifiquem les fonts més probables de decoherència significativa i proposem estratègies potencials per a la seua mitigació.

En el nostre experiment inicial, aconseguim l'emmagatzematge i la posterior recuperació dels fotons únics sota demanda. Aquest fotó es genera mitjançant l'excitació col·lectiva dels estats de Rydberg en un conjunt atòmic fred i s'emmagatzema en una memòria quàntica de Raman de baix soroll situada en un altre conjunt atòmic fred. Els nostres resultats mostren la capacitat d'emmagatzemar i recuperar aquests

fotons únics mantenint una alta relació senyal-soroll de fins a 26 i conservant fortes característiques antiagrupament. També explorem les capacitats de divisió del feix temporal incorporades de la memoria de Raman i utilitzem la memòria amb èxit per controlar la forma d'ona del fotó únic.

En el segon experiment, demostrem per primera vegada una interacció i emmagatzematge de fotons únics en un medi altament no lineal basat en àtoms freds de Rydberg. Utilitzem el protocol DLCZ en un conjunt atòmic fred per crear fotons únics, guiant-los a un altre conjunt per emmagatzemar-los en un estat de Rydberg molt excitat en condicions de transparència induïda electromagnèticament. En estudiar les estadístiques de la llum recuperada dels àtoms de Rydberg, mostrem per primera vegada el filtratge del fotó únic amb llum no clàssica d'entrada. A més, mitjançant la simulació de Monte Carlo, obtenim una comprensió intuïtiva de l'efecte del bloqueig (parcial) de Rydberg sobre la distribució d'estat de Fock dels polsos arbitraris de llum d'entrada. Això ens permet concloure que la resposta del medi està determinada per la distribució d'estat de Fock d'entrada, la qual cosa confirma la comprensió establerta de la no linealitat del conjunt de Rydberg. Aquesta demostració es pot veure com un pas cap a la realització de portes fotons-fotons deterministes basades en conjunts de Rydberg amb entrades d'un sol fotó.

Els resultats presentats en aquesta tesi afirmen el potencial dels conjunts de Rydberg per convertir-se en elements centrals de futures xarxes quàntiques, tant com a fonts de fotons individuals com nodes de processament. A més, els resultats auxiliars proporcionen una comprensió addicional de la física del conjunt de Rydberg i ofereixen una visió de les limitacions que hem de superar per millorar encara més la nostra configuració.

Acknowledgments

First, I would like to thank my parents and family. For being always there when I needed support and backing me in all my life decisions. Even though some of them looked simply terrible from their perspective. And maybe most importantly in the context of this thesis, thank you for making it possible for me to study abroad what, in a long run, led me to ICFO and my PhD.

Next in the line are my friends, many of them. Some acquired during my time at ICFO, like my lovely flatmates Max and Tymek (and lately also Giuliana), ex-quasi-flatmate Flor, and not-flatmates Kora, Mel, Zeynep, Krystian, but some also coming from long before, high school or even middle school, Maciek, Andrzej (aka Żądza), Bańdo, Precel and quite a few others. They were surprisingly willing to listen to all my whining about how horrible it is to be a PhD student and offer help in vengeance or simply try to cheer me up. All these moments, when we got baked, drunk or neither of those and went dancing, singing, bush walking or simply chilled on the terrace, will stay with me for long. Hopefully very long.

However, the main responsible for why I endured these four years is QPSA. I love the vibe and energy of our group and how each of us can be different but still be very welcome. I should start from Hugues who assembled this very fine bunch, and, probably more importantly, gave me the opportunity to take on this PhD. Thank you for giving me the chance to learn about cold atoms and Rydberg physics, and support when I asked for it. Then Auxi, Lukas and Felix, my lab mates, but also dear friends. Auxi should be praised for her inexplicable patience – towards the experimental setup and crucially towards me, and teaching me probably 85 % of what I know about Rydberg physics. Lukas was my most faithful lab companion. I'm still surprised of how good friends we became, despite he tended to listen to Rammstein full on in our lab. Felix is the most recent acquisition of our lab, and sometimes we have some fierce disagreements. But quoting the classic: "Felix, I think it's a beginning of a beautiful friendship".

I also cannot forget to mention other members of our group: Edu for whom things have always two sides, bright sides, Stefano who lifted complaining to the level of art, Dario whose honesty and loudness form an explosive mix, Jelena and Ale who simply cannot be not loved, Chetan who never missed a point when counting them during our Friday afternoon volleyball sessions, Sam who is always willing to help and join any discussion, Soeren whose opinions during lunch debates surprised me many times (which is a good thing!), Bernardo who hates cockroaches (I'm still sorry!), and all the other comrades who, without an exception, are great people! All the daily chats, making fun of ICFO and ranting about academia meant heaps to me! Love you, guys!

Although I acknowledge them only towards the end, I'm indebted to them a lot as they made my PhD life way smoother – ICFO workshops and administration. In particular, I would like to thank Dani, José Carlos and the whole crew of electronic workshop for spending infinite hours on my request to repair things or make them best ever, and the mechanical workshop for creating magic out of my sloppy designs. The help of logistics was also indispensable – super reliable but mostly invisible, as they would start and finish early in the morning, before I would even enter the lab. Human resources created an almost impenetrable shield that screened me from all the conundrums of Spanish bureaucracy and especially Anne, who is like a God mother to all PhD students. I'm not sure how I will survive without them after leaving ICFO. And blessings to Dolors and the deep back office, who patiently helped us organize YAO 2023.

I also want to express my gratitude to Laura, Carles and all people in comité de empresa who continue the efforts to make ICFO an even better place.

Finally, I would like to voice my appreciation to the referees of my thesis, Darrick, Stephan, and Stewart, for their dedicated effort and time spent reviewing my work and providing valuable feedback, what substantially improved the quality of this manuscript.

Contents

Abbreviations

A list of abbreviations used in this thesis:

AOM	acousto-optic modulator
ARP	adiabatic rapid passage
BS	beam splitter
BSM	Bell state measurement
CMOT	compressed magneto-optical trap
DAC	digital-to-analog converter
DLCZ	Duan, Lukin, Cirac and Zoller (protocol)
EIT	electromagnetically induced transparency
EOM	electro-optical modulator
ES	error signal
FMS	frequency modulation spectroscopy
FWHM	full width at half maximum
FWM	four-wave mixing
GHZ	Greenberger-Horne–Zeilinger (state)
HBT	Hanbury-Brown and Twiss (setup)
HOM	Hong–Ou–Mandel
HWP	half-wave plate
MOT	magneto-optical trap
MTS	modulation transfer spectroscopy
OD	optical depth
OR	off-resonant (excitation)
PBS	polarizing beam splitter
PD	photodetector
PDF	probability density function
PDH	Pound-Drever-Hall
PSD	power spectral density
PWM	pulse-width modulation
QIP	quantum information processing
QKD	quantum key distribution
QM	quantum memory
QWP	quarter-wave plate

RAM	residual amplitude modulation
rEIT	Rydberg EIT
RMS	root mean square
SAS	saturated absorption spectroscopy
SHG	second-harmonic generation
SNR	signal-to-noise ratio
SNSPD	superconducting nanowire single-photon detector
SPD	single-photon detector
vdW	van der Waals
WCS	weak coherent state

Chapter 1

Introduction

We find ourselves amidst what is being hailed as *the second quantum revolution* [1]. Whether one chooses to fully embrace this notion or dismiss it as an overhyped buzzword, the fact remains that there is a significant amount of attention, funding, and research being directed towards quantum technologies. This surge in interest is evident not only in numerous blogs, newspapers, and research articles[1], but also in the substantial investments being made by funding agencies and the private sector. Quantum internet is one such technology that is capturing the imagination and resources of many.

1.1 Quantum networks

The quantum internet [3] is envisioned as a network of interconnected nodes, such as quantum computers, with links that enable the transmission, processing, and reception of information encoded in quantum states. The quantum internet is not intended to replace the currently existing internet, but rather to offer additional capabilities, including quantum cryptography and quantum cloud computing [4].

The consensus is that the quantum internet would employ photons as the carriers of quantum information, transmitted through satellites or existing fiber optic infrastructure [4]. Photons are a natural choice due to their fast propagation and weak interaction with the environment, offering relative protection against environmental noise that can corrupt encoded information.

The primary obstacle to achieving a functional large-scale quantum internet are transmission losses. Signal amplification, commonly used to compensate for losses in classical networks, is not possible due to the no-cloning theorem [5, 6]. It prohibits the perfect copying of an unknown quantum state, effectively preventing any type of amplification of a quantum signal. This means that there is a limit resulting from

---

[1] At the moment of writing this thesis, a Google search of "quantum technology" gave 715 million results. To compare, the first agricultural revolution, considered by some as one of the most important developments in human history [2], scored 122 million results.

the transmission losses to how far quantum information can be directly transmitted. For optical fibers operating at telecom wavelengths, where attenuation is minimal, this distance is typically on the order of a few hundred kilometers.

In 1993, Bennett et al. proposed a solution to overcome the limitations imposed by the no-cloning theorem [7]. They introduced the *quantum teleportation* protocol, which enables the transfer of an unknown quantum state from one party to another at the cost of a classical bit and an entangled pair shared between the parties. This effectively shifts the challenge from sending quantum information directly between the parties to distributing entanglement between them. However, transmission losses still impose a maximum rate at which entanglement can be directly distributed [8].

In 1998, Briegel et al. proposed a complementary approach known as the *quantum repeater* protocol to distribute quantum entanglement over long distances [9]. The transmission channel is divided into multiple shorter elementary links, where entanglement is generated through direct photon transmission between nodes. Subsequently, entanglement between increasingly distant nodes is achieved via *entanglement swapping* [10]. A schematic representation of the protocol can be seen in fig. 1.1.

Over the years, numerous protocols have been proposed to realize quantum repeaters [11–19]. These protocols generally require single- or entangled-photon sources, quantum memories, and entanglement swapping[2]. While all these elements are available, their performances are far from what is necessary for practical quantum repeaters.

Generating single photons deterministically is challenging, and many realizations rely on probabilistic pair sources. However, in such cases, the photon emission probability needs to be kept low to avoid multi-photon pulses. Otherwise, the distributed entanglement is of low quality, making it unusable for quantum communication purposes. This results in low entanglement distribution rates.

Most entanglement swapping implementations utilize linear optics, which limits the success probability to 50 % [21]. As a result, the overall success probability of establishing entanglement across a chain of N quantum repeaters is reduced by a factor of 2^N. This again results in low entanglement distribution rates.

Many solutions have been proposed to overcome these limitations. Interestingly, there is a platform that holds promise in addressing both challenges: a highly nonlinear medium of a Rydberg atomic ensemble [22, sec. 5].

1.2 Nonlinear media

Entanglement swapping rely on Bell state measurements (BSM), i.e. a projection on Bell states. BSM, which can be viewed as a specific type of quantum logical gate followed by a measurement, presents a challenge in quantum information processing. As any two-photon gate, it requires photon-photon interactions. However,

---

[2] There exists quantum repeater protocols where no quantum memories or entanglement swapping is necessary, e.g. [20], however, the quantum states required for such protocols cannot be efficiently generated at the moment.

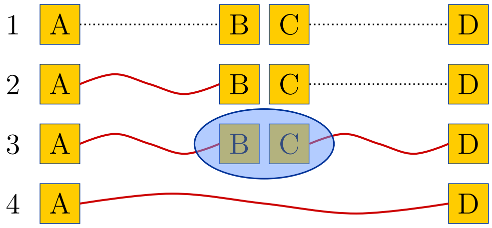

Figure 1.1: Entanglement distribution between node A and node D. (1) Nodes A + B and C + D try to establish entanglement. (2) Due to losses and other imperfections, the elementary links get entangled at different times. Quantum memories allow for storage of entanglement and synchronization of the network. (3) As soon as entanglement is established between the neighboring links, one performs the entanglement swapping (in this case between nodes B and C). (4) Successful swapping results in entanglement between nodes A and D.

photons typically do not interact with each other [3]. Yet, it is possible to mediate photon-photon interactions through light-matter interactions, where a suitable medium exhibits nonlinear behavior. In this scenario, photon arriving later to the medium experience different conditions than earlier photons, effectively resulting in an interaction between them [23]. However, there are no readily available media that exhibit a nonlinearity at the desired single-photon level.

One approach to engineer such nonlinearity is the Knill, Laflamme, and Milburn (KLM) proposal [24], which achieves single-photon level nonlinearity through post-selection using only linear optics and photon detectors. Although this method offers simplicity, its success probability is low as some results are ambiguous and must be discarded. In the case of BSM of two qubits, the success probability is limited to a maximum of 50 % [21][3].

An alternative approach is to use systems that naturally possess single-photon level nonlinearity, such as atoms or quantum dots (an atom can absorb only one photon at a time). However, their coupling to the optical field is typically weak, significantly limiting the probability of photon-photon interaction. One common strategy to overcome this limitation is to place the single emitter within a high-finesse cavity [25]. Unfortunately, this approach significantly increases experimental complexity.

One could think, instead, of enhancing the interaction probability by increasing the number of emitters. This, however, weakens the nonlinearity (two atoms can absorb two photons at a time). Unless, one engineers an interaction between the emitters, which allows all of them to interact with the photons, but, once one emitter interacts, others are unable to do so or do that differently. This would allow the system to have a high light-matter interaction probability, while maintaining the desired level of nonlinearity. One of a few examples of systems exhibiting such

---

[3] If additional auxiliary photons are employed, the efficiency of BSM can approach 1 [**Olivo2018**]. Nevertheless, achieving high efficiencies would necessitate exceptionally efficient single-photon sources to enhance entanglement distribution rates.

behavior are Rydberg atomic ensembles [26].

1.3 QIP with Rydberg ensembles

Rydberg atoms are atoms where the most outer electrons are excited to some high energy state [27]. Such atomic systems hold significant promise for various quantum technologies [28]. They possess unique, exaggerated properties that can be controlled by state selection and the application of external electromagnetic, what makes them highly tunable quantum systems.

There are several reasons why Rydberg atoms are appealing for quantum technologies. Firstly, atoms are inherently stable quantum systems that exhibit consistent behavior within the same species and environment. Additionally, the physics of Rydberg states bears resemblance to that of hydrogen, providing physicists with an intuitive model even for complex multielectron Rydberg systems. However, the most captivating aspect of Rydberg atoms lies in their strong and long-range tunable interactions. These interactions make them attractive candidates, in particular, for quantum simulators and quantum computing [29–31].

In this thesis, we investigate and utilize an ensemble of cold Rydberg atoms for quantum information processing (QIP) purposes. We engineer the Rydberg interactions to dominate over other relevant energy scales in the system, such as the Rabi frequency of the excitation field. In this regime, the interaction between Rydberg atoms becomes so strong that the simultaneous creation of two Rydberg excitations within the ensemble becomes highly unlikely. This phenomenon, known as the *Rydberg blockade* effect [32], effectively results in the nonlinearity at the single photon level discussed earlier. When the first photon enters the medium and promotes an atom to the Rydberg state, it creates a Rydberg excitation that blocks the entire ensemble. Subsequent photons cannot be promoted to the Rydberg level, in other words, experience a different response from the medium compared to the first photon.

The potential of utilizing Rydberg atoms and the blockade for quantum gates was recognized in 2000 [33]. Since then, the observation of entanglement between individual Rydberg atoms has been achieved [34], and the first quantum gates with Rydberg atoms have been demonstrated [35–37]. However, for quantum networking purposes, gates based on Rydberg ensembles are more suitable due to their stronger coupling to the photonic field compared to single atoms. Numerous theoretical proposals have been put forward over the years [32, 38–47], but it was only recently that the first Rydberg-ensemble-based photon-photon gate was demonstrated [48]. A subsequent realization, reported from last year, significantly improved the gate performance by employing a Rydberg ensemble in an optical cavity [49], setting a record efficiency of 41 % for a photonic CNOT gate.

Ensemble-based Rydberg-mediated interactions have also been employed in several single-photon photonic components, such as switches [50, 51], transistors [52, 53], and photon subtractors [54, 55]. All the above demonstrations were conducted using weak coherent states (WCS) rather than true single photons.

The concept of a Rydberg-ensemble-based single-photon source was initially proposed in 2002 [56], but it was only in 2012 that the anti-bunching of photons, a signature of single-photon emission, was observed. For both, well-defined pulses [57] and a continuous stream of photons [58]. Subsequently, the single-photon source was extended to include long-term storage capability [59], and the photons were shown to be highly indistinguishable in a Hong-Ou-Mandel interference experiment with photons obtained from trapped ions [60]. During this time, a limitation in the brightness of the Rydberg photon source due to so-called pollutants was discovered [61], although it is believed not to be a fundamental constraint[4]. In 2018, a room-temperature Rydberg-ensemble-based source was demonstrated [63], but it requires very large Rabi frequencies of the coupling beam to prevent motional dephasing. To date, the best Rydberg-based single-photon source was reported in [62], with an autocorrelation $g^{(2)}(0)$ of 2×10^{-4} and a generation probability in a single trial of 40 % (resulting in an overall generation rate of 1.1 kHz). A similarly performing source was used to demonstrate the highest fidelity quantum gate based on the KLM protocol with a fidelity of 99.84 % [64]. Recently, Rydberg ensembles have also been utilized to generate entangled photon pairs [65] and entangled photon trains with Greenberger-Horne-Zeilinger (GHZ) type of entanglement [66]. Additionally, an entanglement filter was recently demonstrated, where an input product state of two WCS is converted into an entangled photon pair [67].

Another approach utilizing Rydberg ensembles for QIP involves using two different Rydberg states to encode a qubit. It has been shown that such a qubit is robust against external perturbations, and high-fidelity single-qubit rotations can be performed using a microwave field [68]. Using such qubits, the capability of creating high-fidelity atom-photon entanglement has been demonstrated, along with a nondestructive qubit readout scheme [69, 70]. Recently, also a qubit between the ground state and a Rydberg state was reported with a coherence time of 20 µs [71].

It is worth noting that there exists a substantial body of literature that experimentally investigates the properties of Rydberg ensembles, with a particular focus on the interactions between Rydberg excitations and photon interactions mediated by the ensemble. Numerous non-trivial effects have been explored, including the enhancement of three-body losses [72], the study of three-body interactions and bound states [73, 74], and the creation of Rydberg molecules [75]. Recent research has also documented repulsive and attractive photonic interactions [76], investigated the transient dynamics of photons interacting via the Rydberg medium [77, 78], studied interaction-induced dephasing of multiple Rydberg excitations [79] and reported storage-enhanced nonlinear response of the ensemble [80].

The extensive experimental investigations, together with a multitude of theoretical studies and proposals, highlight the potential of Rydberg ensembles as a promising

---

[4] One proposed solution to overcome this limitation is the application of strong electric field pulses to remove the pollutants from the cloud [62].

tool in the quantum toolbox. As they are, in general, complex many-body systems of interacting Rydberg excitations, the theoretical understanding of certain phenomena is still missing, and numerical methods are currently limited to quasi-one-dimensional systems [61]. However, for the same reasons, one can anticipate that many more intriguing findings will emerge.

1.4 Thesis outline

This thesis explores the utilization of a disordered ensemble of cold rubidium atoms excited to a Rydberg state as a single photon source and investigates its properties within the context of quantum information processing. The following chapter provides the necessary theoretical background to comprehend the experimental results discussed later on.

A brief overview of the experimental setup is provided, acknowledging the comprehensive documentation by previous students who have worked on this setup. However, specific developments accomplished during this thesis, including a new locking setup - a major improvement to our experiment, are discussed in greater detail. Subsequently, we discuss the single photon detection and the impact of the detection noise on our measurements.

The following chapter explains different single-photon generation methods, which we use in our experimental works. A particular emphasis is placed on understanding the decoherence mechanisms that impose limitations on the efficiency of our source.

Shifting gears, we focus on the two main experimental results of this PhD research. The first result involves the realization of a building block of a specific quantum repeater protocol, where our single photon source is combined with another cold-atomic setup serving as a quantum memory. The second outcome involves the first investigation of the interactions between non-classical light and a Rydberg medium exhibiting single-photon-level nonlinearity. In this case, our Rydberg ensemble acts as the nonlinear medium, while single photons are generated using another cold-atomic ensemble.

Lastly, the thesis concludes with reflections about future directions that our experiment could take.

Chapter 2

Rydberg atoms and ensembles

In this chapter, we explore the theoretical concepts essential for understanding our investigation of Rydberg physics with ensembles. We address key aspects, starting with the intriguing properties of Rydberg atoms, particularly focusing on their dipole-dipole interactions, which make them promising for quantum information applications. We then examine how these interactions manifest in disordered atomic ensembles, shedding light on their behavior as complex systems. By acquiring a solid grasp of these theoretical foundations, not only we get some insight into Rydberg physics with ensembles, but also understand the associated challenges encountered in our research.

2.1 Rydberg atoms

Rydberg atoms are atoms excited to a high principal quantum number state and exhibit unique and exaggerated properties. Below, I start with describing their single-atom properties to later focus on interactions between them and resulting dipole blockade.

2.1.1 Single-atom properties

Understanding Rydberg atoms' properties, particularly for alkali atoms, involves considering an electron in a modified Coulomb potential. This makes Rydberg atoms similar to hydrogen atoms, however, there are several important factors that need to be taken into account to make this analogy useful [27, ch. 2].

Firstly, spin-orbit coupling, which is often neglected in the textbook hydrogen model, must be included. Secondly, the finite extent of the atomic core (nucleus together with the closed shells) results in a non-negligible probability for the valence electron to penetrate it, especially for low angular momentum states. Lastly, the valence electron polarizes the core electrons, leading to an effect on the valence electron itself.

All of these considerations modify the potential experienced by the valence electron compared to the hydrogen model[1]. Consequently, the well-known scaling laws from the hydrogen model no longer hold. However, it is possible to recover these scaling laws by introducing the concept of *quantum defect* δ, as seen in the Rydberg formula for the binding energy:

$$E_{nlj} = -hc\frac{R_M}{(n-\delta)^2}, \tag{2.1}$$

where h is the Planck's constant, c is the speed of light, n, l, and j are the principal, orbital angular momentum, and total orbital angular momentum quantum numbers, respectively. R_M represents the specific Rydberg constant for the given element [83]. The quantum defect is an empirical constant that depends on n, l, and j, but for large values of n, its dependence on n becomes negligible. In the case of ^{87}Rb, for S-states with $n > 10$, it can be approximated with $\delta = 3.131$. For more precise values, please refer to [84].

With the recovery of the scaling laws, summarized in Table 2.1, some general observations can be made about Rydberg atoms. They possess very large orbits, as depicted in fig. 2.1 (left), and are loosely bound to the nucleus, making them easily ionizable. The energy spacing between nearby states decreases with n, while their transition dipole moment increases, as illustrated in fig. 2.1 (right), enabling the addressing of transitions between these states with a microwave field. The transition dipole moment with the ground state decreases with n, resulting in long lifetimes[2]. However, in practice, lifetimes are limited by black body radiation [27, p. 53-55], but even then they are larger than 50 µs for Rydberg states with $n > 50$ [29, fig. 6].

2.1.2 Rydberg interactions

Rydberg atoms exhibit strong dipole-dipole interactions between each other, due to their large dipole matrix elements.

When two atoms are both excited to Rydberg levels, this interaction causes a change in their energies. To understand this phenomenon, we start by considering the potential experienced by two interacting atoms at a distance $\boldsymbol{r}$. It can be expressed as[3] [29, sec. IIB] [87]

$$V_{dd} = \frac{1}{4\pi\epsilon_0|\boldsymbol{r}|^3}\left(\boldsymbol{d}_1\cdot\boldsymbol{d}_2 - 3\left(\boldsymbol{d}_1\cdot\frac{\boldsymbol{r}}{|\boldsymbol{r}|}\right)\left(\boldsymbol{d}_2\cdot\frac{\boldsymbol{r}}{|\boldsymbol{r}|}\right)\right) \equiv \frac{C_3}{|\boldsymbol{r}|^3}, \tag{2.2}$$

---

[1] Typically used model potential was derived in [81]. A nice and detailed explanation of how to obtain Rydberg wave functions for this model potential was given in [82, sec. 2.1.2].

[2] We are mostly concerned about the decay to the ground state (or the lowest $P_{3/2}$ state in the case of Rydberg $S_{1/2}$ states), because the Einstein A coefficient describing the spontaneous decay process is proportional to the third power of the states' energy difference (and only directly proportional the transition dipole moment). Hence, the lifetime is mostly limited by the decay to the ground state.

[3] It's important to note that this expression is valid only when the inter-atomic distance is much larger than the electronic wave functions of the two atoms.

Property	Scaling	$5S_{1/2}$	$90S_{1/2}$
Binding energy E_{n^*}	$(n^*)^{-2}$	$4.18\,\mathrm{eV}$	$1.8\,\mathrm{meV}$
Orbit radius $\langle r\rangle$	$(n^*)^2$	$298\,\mathrm{pm}$	$532\,\mathrm{nm}$
Level spacing $E_{n^*} - E_{n^*+1}$	$(n^*)^{-3}$	$605\,\mathrm{THz}$	$9.87\,\mathrm{GHz}$ ($91S_{1/2}$)
Dipole moment between adjacent states	$(n^*)^2$	$4.23\ ea_0$ ($5P_{3/2}$)	$4701\ ea_0$ ($89P_{3/2}$)
Lifetime τ	$(n^*)^3$	$26.2\,\mathrm{ns}$	$271\,\mathrm{\mu s}$ (at $300\,\mathrm{K}$)
Dipole moment $5P_{3/2}$ to Rydberg states	$(n^*)^{-3/2}$	–	$0.0032\ ea_0$
Van der Waals coefficient C_6	$(n^*)^{11}$	$6.76\times10^{-7}\,\mathrm{Hz\mu m^6}$	$1.64\times10^{13}\,\mathrm{Hz\mu m^6}$
Polarizability α	$(n^*)^7$	$79.4\,\mathrm{mHz\,cm^2/V^2}$	$3.17\,\mathrm{GHz\,cm^2/V^2}$

Table 2.1: Summary of scaling laws for Rydberg atoms together with example values for ^{87}Rb. Transition dipole moments are the reduced matrix elements in the total angular momentum J basis, defined in asymmetric notation. e is the electron charge and a_0 is the Bohr radius. Scaling laws were taken from [22], the ground state values from [83] and the $90S_{1/2}$ values were calculated with ARC [85] and with pairinteraction [86].

where $\boldsymbol{d}_i$ represents the dipole operators of atom i, which couple the initial Rydberg state to other dipole-coupled states. C_3 is a distance-independent but angle-dependent factor (however, for S-states, which are of main interest in this thesis, the angle dependence is very weak).

To examine the effects of dipole-dipole interactions on the energy of two Rydberg atoms, we consider the case where both atoms are excited to the same Rydberg state, which is a typical scenario in our experiments. When the atoms are very far apart ($r \to \infty$), they can be described by a product state: $|\psi\rangle = |nlj, nlj\rangle$, where $|nlj\rangle$ represents a specific fine structure level.

The dipolar interaction given by eq. 2.2 couples $|\psi\rangle$ to other two-atom states $|n_1l_1j_1, n_2l_2j_2\rangle$, following the usual dipole selection rules, i.e., $l_1, l_2 = l \pm 1$ and $j_1, j_2 = j \pm 0, 1$. While there are infinitely many dipole-coupled states, in practice, the dipole-dipole interaction strength is primarily determined by a few energetically nearby two-atom states. This is due to two factors: the small energy difference between the two-atom states (which becomes evident later in this section) and the requirement of non-negligible dipole matrix elements. The dipole matrix elements are significantly suppressed for large differences in principal quantum numbers [88, sec. IIIA], as illustrated in fig. 2.1(right).

Let's consider the case where we restrict for simplicity our analysis to only two two-atom states. We can write the interaction Hamiltonian as follows [29, sec. IIB]:

$$H_{\text{int}} = \begin{pmatrix} 0 & V_{dd} \\ V_{dd} & \Delta \end{pmatrix}, \tag{2.3}$$

where Δ represents the energy mismatch between the two states $\Delta = E_{n_1l_1j_1} + E_{n_2l_2j_2} - 2E_{nlj}$, often referred to as the *Förster defect*. The eigenenergies resulting

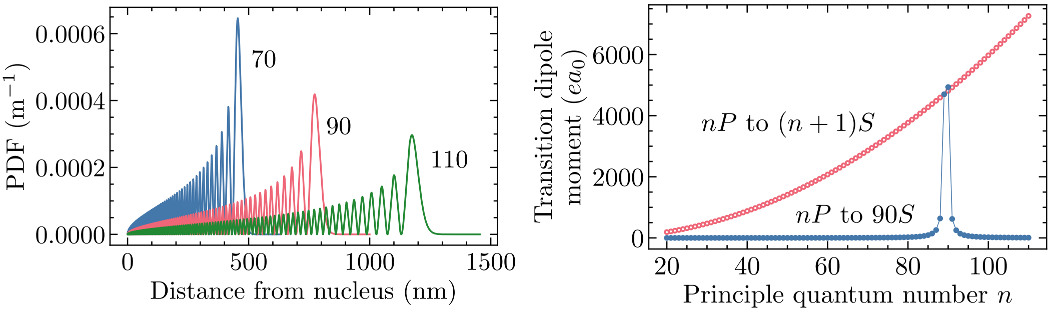

Figure 2.1: (left) Dependence of probability density function (PDF) of finding the valence electron on the distance from the nucleus for three different principal quantum numbers. One can appreciate the size of Rydberg atoms can more than 1000 times larger than ground-state atoms. (right) Transition dipole moment between state $\left|nP_{3/2}, m_J = 3/2\right\rangle$ and a neighboring state $\left|(n+1)S_{1/2}, m_J = 1/2\right\rangle$ (pink) or state $\left|90S_{1/2}, m_J = 1/2\right\rangle$ (blue). Transition dipole moments between the neighboring states grow like $(n^*)^2$. One should compare the plotted values with the ground state $\left|5S_{1/2}, F = 2, m_F = +2\right\rangle$ to the excited state $\left|5P_{3/2}, F = 3, m_F = +3\right\rangle$ transition dipole moment, which is 2.99 ea_0. In blue, one can also see that often there are very few dominant neighbors that couples very strongly to a given state, while other states are much more weakly coupled.

from this Hamiltonian are given by:

$$V_{\pm}(r) = \frac{\Delta}{2} \pm \mathrm{sign}(\Delta)\sqrt{\frac{\Delta^2}{4} + \frac{C_3^2}{r^6}}. \tag{2.4}$$

In the limit of small inter-atomic distances and/or small Förster defects, the original states become heavily mixed, and the eigenenergies can be approximated as:

$$V_{\pm}(r) \approx \mathrm{sign}(\Delta)\frac{C_3}{r^3}. \tag{2.5}$$

However, we are not concerned with this regime, as our atomic cloud is too dilute to exhibit such strong interactions. Usually, one refers to this regime as (resonant) dipolar interactions.

In the opposite limit of large inter-atomic distances, the deviation from the original energy is small, resulting in what is known as *the van der Waals* (vdW) interaction:

$$V_{\mathrm{vdW}} \approx -\frac{C_3^2}{\Delta r^6} = \frac{C_6}{r^6}. \tag{2.6}$$

It's worth noting that the C_6 coefficient for Rydberg states can be either positive or negative, depending on the sign of the Förster defect[4].

It should be mentioned that it is possible to alter the nature of the interaction from van der Waals to dipolar at large distances. This can be achieved through

---

[4] For atoms in the ground state, the van der Waals interaction is always attractive.

the application of external electric fields [89–91], which corresponds to tuning Δ to approach zero, usually called *Förster resonance*, as well as with microwave fields [92–94].

In general, there exist numerous two-atom states that contribute to the interaction between two Rydberg atoms. Since the vdW interactions have a small effect on the original states, perturbation theory can be employed. It turns out, after some massaging, that the result can be expressed with the same simple formula as in eq. 2.6 [82, sec. 2.2]:

$$V_{\mathrm{vdW}}(r) = \sum_{ij} \frac{|\langle\psi| V_{dd} |i,j\rangle|^2}{2E - E_i - E_j} \tag{2.7}$$

$$= \frac{C_6}{r^6}, \tag{2.8}$$

with the coefficient C_6 describing now interaction with many two-atom states. $|i\rangle$ and $|j\rangle$ denote different unperturbed single-atom states, and E_i, E_j are their respective energies.

From the above paragraphs, it is evident that the C_6 coefficient depends on the dipole matrix elements (to the power 4), which are notably large for Rydberg atoms, and the Förster defects, which diminish for larger principal quantum numbers. From Table 2.1, one can easily see that C_6 scales with the principal quantum number as $(n^*)^{11}$. It's clear that one should expect strong interactions between Rydberg atoms, as shown in fig. 2.2(right).

Dipole blockade

The interactions between Rydberg atoms give rise to a phenomenon known as *dipole blockade*, which inhibits multiple excitations. Let us again consider a pair of Rydberg atoms at a distance r. The energy shift experienced by them depends on r, as demonstrated in the previous section. When the atoms are close to each other, this energy shift can exceed the excitation linewidth. Consequently, if they were in their ground states, only one of them can be excited to the Rydberg state, as the laser used for excitation is not resonant with the transition from a singly excited state to a doubly excited state, as illustrated in fig. 2.2(left).

The dipole blockade effect is characterized by a characteristic length known as the *blockade radius*, denoted as r_b. The specific expression for r_b varies depending on the context[5], but it is typically defined as the distance at which the interaction $V_{\mathrm{vdW}}(r)$ is equal to the excitation linewidth Ω, i.e., $V_{\mathrm{vdW}}(r_b) = \hbar\Omega$. For a weak

---

[5] The determination of the blockade radius depends on the specific circumstances. For instance, different formulas apply when considering a direct excitation to a Rydberg state using a π-pulse, compared to the case of Rydberg electromagnetically induced transparency (EIT), which will be discussed later in this thesis. The situation gets even more complicated if one studies complex phenomena such as the few-body physics of Rydberg polaritons, as explored in works like [95] or [96].

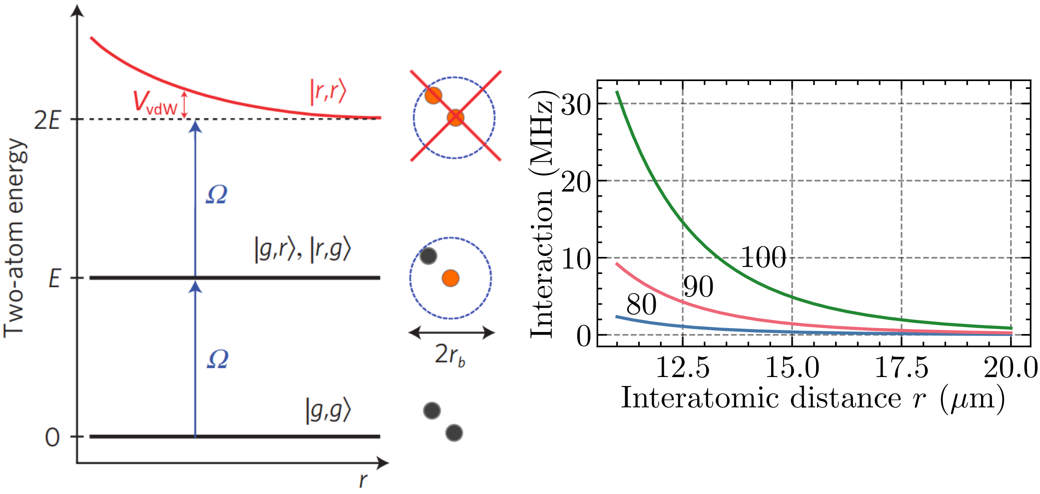

Figure 2.2: (left) Schematic representation of the blockade effect. When atoms are far away, they can be both excited from their ground state $|g\rangle$ to the Rydberg state $|r\rangle$. However, when they get closer, the van der Waals interaction starts shifting the doubly excited state $|r,r\rangle$. At the blockade radius, r_b this shift is so large that the driving field Ω is not resonant with the transition from singly to doubly excited state. Effectively, if the atoms are closer than r_b, only one of them can be excited to the Rydberg state. Image adopted from [97]. (right) Strength of the van der Waals interaction as a function of the interatomic distance for different Rydberg levels of ^{87}Rb, $80S_{1/2}$, $90S_{1/2}$ and $100S_{1/2}$. Calculations were performed with pairinteraction [86].

driving Ω is simply the laser linewidth, for strong driving, due to power broadening, it would correspond to the excitation field Rabi frequency. This yields the formula:

$$r_b = \sqrt[6]{\frac{C_6}{\hbar\Omega}}, \tag{2.9}$$

from which one can see that $r_b \propto (n^*)^{11/6}$. In our experiments, the typical blockade radius is approximately 13 µm for a Rydberg state with $n = 90$.

The concept of dipole blockade can also be applied to ensembles. In particular, when the size of the ensemble is smaller than the blockade radius, only a single Rydberg excitation can exist, irrespectively of the number of atoms in the ensemble. We will discuss this scenario in the next section.

2.2 Rydberg atomic ensembles

In our experiment, we investigate an ensemble of atoms, which leads to intriguing implications. Firstly, I will explain the directional emission of photons from the ensemble in a well-defined mode. This phenomenon is closely related to the concept of spin waves. Later, I will focus on electromagnetically induced transparency (EIT) and its notable properties. Throughout the discussion, I examine how Rydberg interactions and dipole blockade influence these phenomena.

2.2.1 Spin waves

Let us imagine an ensemble of atoms at which we shine a resonant laser field. The interaction of the laser fields with multiple atoms simultaneously results in shared, delocalized excitations among the atoms. These collective excitations, often referred to as *spin waves*[6], can be viewed as coherent superpositions of excitations present in the individual atoms. For simplicity, let's assume that all atoms are equally coupled to the laser field, i.e. we ignore the fact that the excitation field has a finite extent, and that we create exactly one excitation. The latter assumption holds true for specific systems, such as a perfect quantum memory with a single photon at the input or ensembles in which only one excitation can exist due to interatomic interactions. As we discussed earlier, our system belongs to the second category. In such a case, a state describing this single excitation in the ensemble, consisting of N atoms, can be expressed as follows [56]:

$$|R\rangle = \frac{1}{\sqrt{N}} \sum_i e^{i\boldsymbol{k}\cdot\boldsymbol{r}_i} |g_1 g_2 \ldots r_i \ldots g_N\rangle , \tag{2.10}$$

where $|g_i\rangle$, $|r_i\rangle$, and $\boldsymbol{r}_i$ represent the ground state, the Rydberg state, and the position of the atom i, respectively. $\boldsymbol{k}$ is the wave vector of the exciting field (or the net wave vector of all the exciting fields). It's important to note that there exists a well-defined phase relation between the single-atom excitation states, determined by the wave vectors of the exciting field and the atoms' positions in the ensemble, i.e. the term $e^{i\boldsymbol{k}\cdot\boldsymbol{r}_i}$.

To understand why this state leads to directed emissions, we can follow a similar approach to the one described in reference [56]. Let's imagine that we transfer the excitation $|R\rangle$ to a short-lived excited state $|e\rangle$ using a π-pulse from an additional field with wave vector $\boldsymbol{k}_c$. The resulting collective state is (assuming here that $|e\rangle$ has lower energy than $|r\rangle$ and, hence, the minus sign in the phase factor exponent)

$$|E\rangle = \frac{1}{\sqrt{N}} \sum_i e^{i(\boldsymbol{k}-\boldsymbol{k}_c)\cdot\boldsymbol{r}_i} |g_1 g_2 \ldots e_i \ldots g_N\rangle . \tag{2.11}$$

This state will emit radiation into various modes, with all atoms returning to the ground state and a single photon propagating in the direction $\boldsymbol{k}_e$. Although it is not a fully correct picture, one can imagine N atoms that start emitting radiation simultaneously due to spontaneous decay. The radiation from each atom interferes with the radiation from others, and based on the well-defined phase relation between these fields, i.e. all the atoms were in a superposition state, certain modes are favored

---

[6] "Wave" refers to the phase factor which changes its value depending on the atom's position, as explained in the paragraph below.

over others. The probability of emitting a photon into the mode $\boldsymbol{k}_e$ can be expressed as:

$$P_e \propto \frac{1}{N}\left|\sum_i e^{i(\boldsymbol{k}-\boldsymbol{k}_c-\boldsymbol{k}_e)\cdot\boldsymbol{r}_i}\right|^2, \tag{2.12}$$

where it was assumed that the single-atom emission is isotropic.

When $\boldsymbol{k}-\boldsymbol{k}_c-\boldsymbol{k}_e$ is nonzero, different terms in the summation partially cancel each other due to the atoms' different positions. However, when the phase matching condition is satisfied, i.e., $\boldsymbol{k}-\boldsymbol{k}_c-\boldsymbol{k}_e=0$, all the phase factors add constructively, resulting in the maximum value of P_e. Therefore, one gets strongest emission in the direction given by $\boldsymbol{k}_e=\boldsymbol{k}-\boldsymbol{k}_c$. It is also worth noting that the suppression of non-phase-matched emission increases with the atoms number. This means that to achieve high directed retrieval efficiency, we want a system which has a high optical depth [98, sec. III]. A spin wave state is also robust against the particle loss and its fidelity with the initial state decreases by a factor of $1/N$ for each lost atom, where N is the atom number [99, sec. IIIC]. All the above-mentioned properties make spin waves a very useful tool for quantum information processing.

2.2.2 Rydberg super-atom

The blockade effect, which was discussed in sec. 2.1.2, can be extended to an ensemble of N atoms, where only one excitation is allowed within the blockaded volume[7]. This effect leads to the emergence of a two-level *super-atom* [32], with a ground state $|G\rangle = |g_1 \dots g_N\rangle$ and an excited state $|R\rangle$ defined in eq. 2.10.

When the ensemble is driven, it exhibits Rabi oscillations only between these two states, with a collective Rabi frequency that is enhanced by a factor of $\sqrt{N}$ compared to the single-atom Rabi frequency:

$$\begin{aligned}\langle G|\boldsymbol{d}|R\rangle &= \frac{1}{\sqrt{N}}\sum_i^N \langle g_i|\boldsymbol{d}|r_i\rangle \langle g_1 \dots g_{j-1}g_{j+1}\dots g_n \mid g_1 \dots g_{j-1}g_{j+1}\dots g_n\rangle \\ &= \sqrt{N}\langle g|\boldsymbol{d}|r\rangle,\end{aligned} \tag{2.13}$$

where $\boldsymbol{d}$ represents the dipole operator.

The blockade effect allows a single photon to saturate the absorption of the atomic medium, while the shared collective excitation enhances the coupling to the driving field. These properties make the super-atom concept a powerful tool for various quantum applications. For example, the effective two-level system has been utilized to investigate quantum electrodynamics effects in free-space, achieving strong light-matter coupling without the need for an optical cavity [100]. In the realm of quantum technologies, these effects have been leveraged to realize single-photon sources [57, 62, 64], entanglement sources [65, 67], single-photon transistors [52, 53], collective qubits [68, 69], and quantum gates [48, 49, 101]. As a result, Rydberg ensembles have emerged as a promising platform for quantum networking.

---

[7] This is why we considered only one collective excitation in the previous section.

2.2.3 Electromagnetically induced transparency

Let's switch gears and explore a fascinating phenomenon known as electromagnetically induced transparency (EIT), which we use to engineer interactions between light and an atomic ensemble. For instance, it can transform an initially opaque medium into a transparent one, as a result of the destructive interference of different transitions pathways in a multilevel system. However, let's proceed step by step.

I'll provide some intuitive understanding of why EIT occurs, while sparing the reader from detailed calculations that have been extensively covered before. Interested readers can refer to a comprehensive and comprehensible chapter on EIT in the thesis of Ornelas-Huerta [82, sec. 3.1][8].

EIT occurs in three-level systems where one transition between two states is very weak, while another transition is driven by a strong coupling field. Typically, this phenomenon is observed in so-called lambda systems, as depicted in fig. 2.3(top left), where the weak transition corresponds to a transition between hyperfine states of the same ground state which is dipole-forbidden. However, in our case, we are primarily interested in ladder systems, as shown in fig. 2.3(bottom left), where the weak transition is between the ground state and a Rydberg state, also dipole-forbidden in our configuration.

Consider the scenario illustrated in fig. 2.3(right). In this case, a strong coupling field Ω_c connects the excited state $|e\rangle$ with the Rydberg state $|r\rangle$, while a weak probe field Ω_p couples the ground state $|g\rangle$ with the excited state. Both fields can be detuned from their respective resonances, with Δ_p representing the probe detuning and Δ_c representing the coupling detuning. For this setup, one can derive under the rotating wave approximation the interaction Hamiltonian[9], which takes the form:

$$H = \frac{\hbar}{2} \begin{pmatrix} 0 & \Omega_p^* & 0 \\ \Omega_p & -2\Delta_p & \Omega_c^* \\ 0 & \Omega_c & -2\delta \end{pmatrix}, \tag{2.14}$$

where $\delta = \Delta_p + \Delta_c$ is the two-photon detuning.

Let's begin by considering the case where both fields are on-resonance ($\Delta_p = \Delta_c = 0$), which is a typical experimental condition. In this case, the Hamiltonian

---

[8] Presented there derivation does not include purely dephasing effects, which may be relevant in our context. However, the obtained results can be easily modified by following the derivation in a review by Firstenberg et al. [26, sec. 3.2]. It is important to note that different authors may adopt different conventions for defining relevant quantities such as Rabi frequencies, decay rates, and dephasing rates. Fortunately, the two cited sources employ the same convention. Another good reference to learn about EIT is [102] which, in general, are a great lecture notes covering almost any topic of atomic optics.

[9] Which means neglecting the kinetic part of the Hamiltonian.

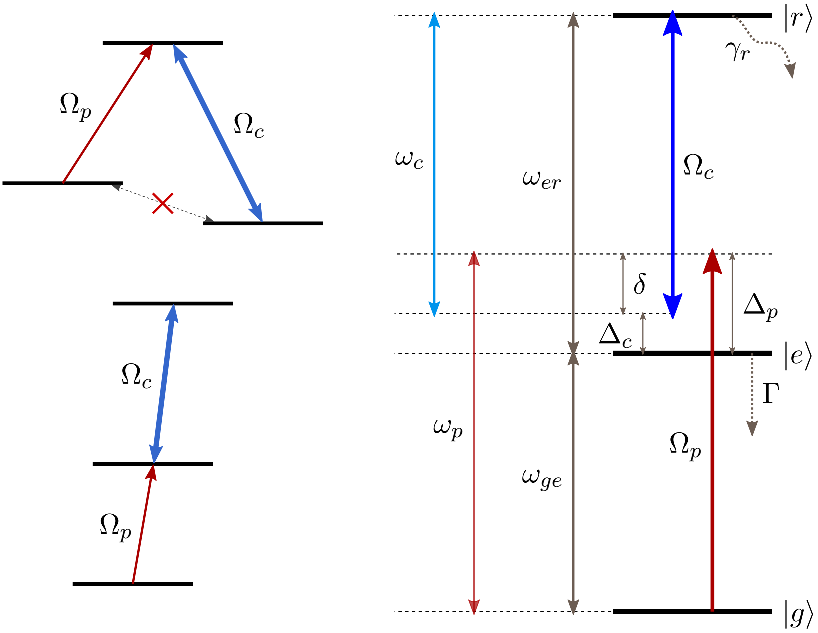

Figure 2.3: EIT atomic level schemes. (left) Two typical systems in which one can observe EIT, a lambda system in the top and a ladder system in the bottom. (right) Ladder system of interest. Relevant states are the ground state $|g\rangle$, the excited state $|e\rangle$ with decay rate Γ, and the metastable Rydberg state $|r\rangle$ with dephasing rate γ_r. A weak probe field with frequency ω_p couples $|g\rangle$ and $|e\rangle$ with a detuning $\Delta_p = \omega_p - \omega_{ge}$. A strong control field with frequency ω_c drives the transition $|e\rangle \rightarrow |r\rangle$ with a detuning $\Delta_c = \omega_c - \omega_{er}$. The two-photon detuning is $\delta = \Delta_p + \Delta_c$.

has three eigenvectors and their corresponding eigenenergies:

$$\begin{aligned} |D\rangle &= \cos\theta|g\rangle - \sin\theta|r\rangle & \hbar\omega_D &= 0 \\ |+\rangle &= \frac{1}{\sqrt{2}}(\sin\theta|g\rangle + |e\rangle + \cos\theta|r\rangle) & \hbar\omega_+ &= \frac{\hbar}{2}\sqrt{\Omega_c^2 + \Omega_p^2} \\ |-\rangle &= \frac{1}{\sqrt{2}}(\sin\theta|g\rangle - |e\rangle + \cos\theta|r\rangle) & \hbar\omega_- &= -\frac{\hbar}{2}\sqrt{\Omega_c^2 + \Omega_p^2}, \end{aligned} \tag{2.15}$$

where θ is the *mixing angle* given by:

$$\cos\theta = \frac{\Omega_c}{\sqrt{\Omega_c^2 + \Omega_p^2}}, \qquad \sin\theta = \frac{\Omega_p}{\sqrt{\Omega_c^2 + \Omega_p^2}}. \tag{2.16}$$

There are two important observations to make. Firstly, while the state $|D\rangle$ remains at zero energy, the states $|+\rangle$ and $|-\rangle$ are shifted up and down, respectively. Secondly, the states $|+\rangle$ and $|-\rangle$ contain components from all the bare atomic states, while the state $|D\rangle$ has no contribution from $|e\rangle$ and is therefore the *dark state*. If the atom is prepared in this state, there is no possibility of excitation to $|e\rangle$ and subsequent spontaneous emission.

To observe EIT, a typical scenario involves shining a coupling light on an ensemble of atoms initially in the ground state $|g\rangle$. At $\Omega_p = 0$, one can identify that $|D\rangle = |g\rangle$. Then, a weak probe light is shined, which changes the EIT eigenstates and gives some $|g\rangle$ component to $|+\rangle$ and $|-\rangle$. However, as the whole process happens adiabatically, the atoms remain in state $|D\rangle$, which is a dark state and cannot absorb any light. Therefore, the ensemble appears transparent to the probe light, despite the probe is resonant with the $|g\rangle$-to-$|e\rangle$ transition. Moreover, if the probe detuning Δ_p were included, one could show that the ensemble would be maximally absorptive when Δ_p matches the energy shift of either $|+\rangle$ or $|-\rangle$.

This discussion presents a simplified picture where spontaneous decay from $|e\rangle$ and $|r\rangle$, as well as other sources of decoherence, were neglected. To include these effects, one would typically use the master equation in Lindblad form to compute the non-unitary dynamics of the system. This leads to a system of six differential equations, as detailed in [82, sec. 3.1][10].

Under the assumptions of a weak probe field (implying that most of the atoms remain in $|g\rangle$) and the system being in a steady state (where the populations and coherences between the states do not evolve in time), one can determine the susceptibility of the atomic ensemble[11]. For a near resonant probe, the susceptibility can be expressed as:

$$\chi = \frac{\varrho\sigma_0}{k_0} \frac{i\Gamma\left(2\gamma_r - 2i\delta\right)}{\left(\Gamma - 2i\Delta_p\right)\left(2\gamma_r - 2i\delta\right) + \Omega_c^2}, \tag{2.17}$$

where $\sigma_0 = \frac{3\lambda_0^2}{2\pi}$ is the resonant cross-section of the $|g\rangle$-to-$|e\rangle$ transition, $k_0 = \frac{2\pi}{\lambda_0}$ is its wave number and ϱ is the atomic density. As depicted in fig. 2.3(right), Γ is the decay rate from $|e\rangle$ to $|g\rangle$ and γ_r describes an energy-conserving[12] dephasing processes of the Rydberg state.

Now, let's explore what all of this means for the propagation of the probe light in the atomic ensemble. The susceptibility is related to the complex refractive index n_*, which determines the optical properties of the medium. Approximately, we have:

$$n_* = \sqrt{1+\chi} \approx 1 + \chi/2. \tag{2.18}$$

Assuming a uniform density for the ensemble of a length L, the relation between the

---

[10] The most appropriate derivation for our case is given in [102, sec. 6.2.2], although it does not explicitly show all the differential equations, making it difficult to appreciate the complexity of the problem. To map their problem to ours, one should identify $|g_1\rangle$ with $|r\rangle$ and set the decay constant Γ_1 to zero. Also in [26, sec. 3.2], one can find appropriate equations, however, it does not provide much insight to how to solve them.

[11] To understand how the density matrix from the Lindblad equation relates to the susceptibility of the ensemble, I recommend reading [103, sec. 4.2].

[12] Meaning there is no decay from $|r\rangle$, just loss of coherence.

output probe field and the input field is given by:

$$\frac{E_{\text{out}}}{E_{\text{in}}} = e^{in_* k_0 L} = e^{-\operatorname{Im}\{\chi\}k_0 L/2} e^{i(1+\operatorname{Re}\{\chi\}/2)k_0 L}. \tag{2.19}$$

The first term describes the attenuation of the input field, while the second term accounts for dispersion, resulting in a phase shift of the output field relative to the input field.

When considering the transmission of light through the ensemble, we define the transmission coefficient, denoted as t, as the ratio of the output intensity I_{out} to the input intensity I_{in} of the probe, $I_{\text{out}} = tI_{\text{in}}$. In the case of EIT, the transmission coefficient is given by the expression:

$$t = \exp\left(-\text{OD}\,\operatorname{Im}\left\{\frac{i\Gamma\left(2\gamma_r - 2i\delta\right)}{\left(\Gamma - 2i\Delta_p\right)\left(2\gamma_r - 2i\delta\right) + \Omega_c^2}\right\}\right), \tag{2.20}$$

where $\text{OD} = \varrho\sigma_0 L$ represents the usual two-level optical depth of the ensemble. One can see a typical EIT transmission curve in fig. 2.4. The resonant transmission of EIT ($\Delta_c = \Delta_p = 0$) is given by:

$$t = \exp\left(-\frac{\text{OD}}{1 + \frac{\Omega_c^2}{2\Gamma\gamma_r}}\right). \tag{2.21}$$

One can see that, in the absence of dephasing ($\gamma_r = 0$), the EIT transparency would be always 1. However, in the presence of dephasing, the transparency is decreased and influenced by the optical depth, the Rabi coupling frequency, and the excited state decay rate.

Moreover, the EIT transparency peak for resonant coupling can be well approximated with a Gaussian function with the amplitude given by eq. 2.21 and width (understood as the standard deviation) given by

$$\Gamma_{\text{EIT}} = \frac{\Omega_c^2}{\Gamma\sqrt{8\text{OD}}}, \tag{2.22}$$

where for simplicity we neglected the dephasing in the Rydberg level[13].

Another notable property of EIT is the phenomenon of *slow light*, where the speed of light propagation in the medium is significantly reduced due to strong dispersion around the EIT resonance, as one can see in fig. 2.4(right). This effect leads to an

---

[13] Otherwise the formula gets more complicated:

$$\Gamma_{\text{EIT}} = \sqrt{\frac{\left(2\Gamma\gamma_r + \Omega_c^2\right)^3}{8\Gamma\text{OD}\left(\Gamma\Omega_c^2 + 4\Omega_c^2\gamma_r - 8\gamma_r^3\right)}} \tag{2.23}$$

.

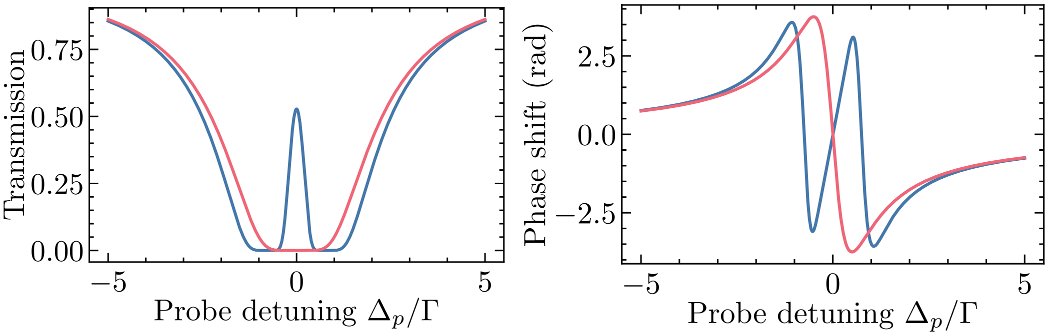

Figure 2.4: Transmission and phase shift for a probe propagating through a medium with $OD = 15$ under EIT conditions (blue) and with normal two-level susceptibility, i.e. without the control field (red). Parameters typical for our experiment were used to plot the figures: resonant coupling $\Delta_c = 0$, $\Omega_c = 1.5\Gamma$ and $\gamma_r = 0.05\Gamma$.

extended interaction time between the light and the ensemble. To see why it occurs, let us recall the group refractive index n_g given by:

$$n_g = n + \omega_p \frac{\partial n}{\partial \omega_p} \approx 1 + \frac{\mathrm{Re}\{\chi\}}{2} + \frac{\omega_p}{2} \frac{\partial\, \mathrm{Re}\{\chi\}}{\partial \omega_p}, \tag{2.24}$$

where $n = \mathrm{Re}\{n_*\}$ is the real part of the refractive index as in eq. 2.18. In the case of EIT, the last term dominates the expression. The group velocity $v_g = c/n_g$ is used to define the group delay τ_d, which quantifies the additional time it takes for a pulse to travel through the ensemble compared to vacuum $\tau_d = L(1/v_g - 1/c) \approx L/v_g$. By using the expression for χ from eq. 2.17 and the last term of the equation for n_g, we obtain for resonant probe and coupling ($\Delta_c = \Delta_p = 0$):

$$\tau_d = \mathrm{OD} \frac{\Gamma\Omega_c^2 - 8\Gamma\gamma_r^2}{(2\Gamma\gamma_r + \Omega_c^2)^2}. \tag{2.25}$$

Assuming a negligible dephasing rate γ_r (which is not entirely true for our system, but I find it instructive), we can simplify the equation further to:

$$\tau_d = \frac{\mathrm{OD}\,\Gamma}{\Omega_c^2}. \tag{2.26}$$

In our experiment, the typical group delay is around 70 ns[14], corresponding to an average group velocity of 410 m/s. This means that the light travels in our ensemble about 1,400,000 times slower than the speed of light in vacuum.

---

[14] This value was measured for parameters given in Table 3.1. However, estimating the group delay is somewhat challenging due to the complex propagation dynamics of short pulses under rEIT conditions [77, 78]. Moreover, if one were to naively use eq. 2.25 and calculate the expected group delay, the result would be more than 10 times larger than the measured value.

From the expressions for the transmission coefficient, eq. 2.21, and the group delay, eq. 2.26, it becomes apparent that optimizing EIT is not a straightforward task. On one hand, we aim to achieve a large group delay to extend the interaction time with the ensemble, which requires a high OD and a small coupling Rabi frequency. However, these factors also lead to a decrease in EIT transparency. In our case, working with high-lying Rydberg levels which have small transition dipole moments to the excited state, the maximum achievable coupling Rabi frequency is typically used, although it may not always be the optimal scenario.

2.2.4 Dark state polariton

So far, we have been treating the probe field in a classical manner. However, in order to account for the quantum nature of the probe field and work with single photons, we introduce the concept of a *polariton*. A polariton is a quasi-particle that arises from a coherent superposition of an electromagnetic field and an atomic excitation. In the context of EIT, polaritons do not couple to the excited state[15] and therefore cannot emit radiation, so they are referred to as *dark-state polaritons*. The mathematical description of EIT polaritons was developed in [104, 105], and I will provide a brief summary of the most relevant properties here. For a detailed and easily understandable derivation, I recommend referring to the thesis by Ornelas-Huerta [82, sec. 3.2].

Let's consider the same scenario as in the previous section, depicted in fig. 2.3. We assume that the probe light propagates along the z-direction and is described by an amplitude operator $\hat{\mathcal{E}}^\dagger(z)$, which creates a photon at position z. The collective excitations shared among the atoms in the medium are described by operators $\hat{\mathcal{P}}^\dagger(z)$ and $\hat{\mathcal{S}}^\dagger(z)$, which create atomic excitations at position z in the $|e\rangle$ and $|r\rangle$ states, respectively. It can be shown that the creation operator for the polariton field takes the form [104]:

$$\hat{\Psi}^\dagger(z) = \frac{\Omega_c \hat{\mathcal{E}}^\dagger(z) - g\sqrt{N}\hat{\mathcal{S}}^\dagger(z)}{\sqrt{\Omega_c^2 + g^2 N}}, \tag{2.27}$$

where g describes the single-atom coupling of probe photons to the $|g\rangle$-to-$|e\rangle$ transition (proportional to the transition dipole moment rescaled) and N is the number of atoms participating in the formation of the polariton.

Several observations can be made based on this expression. First, it bears a resemblance to the dark eigenstate in eq. 2.15, as they are different descriptions of the same phenomenon. Second, the coupling g is enhanced by a factor of $\sqrt{N}$, signifying that the probe field couples to a *collective* atomic excitation. Third, $\hat{\mathcal{P}}^\dagger(z)$ is absent, indicating that the polariton does not couple to the excited state and therefore cannot emit light[16]. It is a dark excitation. Finally, the polariton comprises

---

[15] In the scenario relevant to us, but in principle they can couple to the excited state.

[16] We assume here that the lifetime of $|r\rangle$ much longer than other time scales in the system, which is a valid assumption in our system. In reality, a radiative decay from $|r\rangle$ is possible, however, very unlikely.

both electromagnetic and atomic (Rydberg) excitations, inheriting characteristics from both types of excitations. Its dynamics stem from the photonic component, resulting in propagation, while the spin-wave component can give rise to interactions with other polaritons or external fields.

Intuitively, as we decrease Ω_c, the polariton becomes more Rydberg-like, leading to a decrease in the group velocity. Conversely, as we increase Ω_c, the polariton becomes more photon-like, resulting in an increase in the group velocity. In fact, one can show [104] that the group velocity of the polariton is $v_g = c/(1 + g^2 N/\Omega_c^2)$, which agrees with our intuition and, in fact, is equal to the group velocity derived in the previous section.

In the extreme case where we turn off the control field, the polariton is entirely mapped to a Rydberg excitation. By subsequently turning the control field back on, we can retrieve the pure Rydberg excitation as a propagating polariton in the probe mode. This coherent conversion of a propagating polariton into an atomic excitation and vice versa is the principle behind EIT quantum memories, which are known for their high storage efficiencies [106, 107] and long storage times [108].

2.2.5 Rydberg polaritons

In the previous sections on EIT, we focused mainly on the effects of EIT, without considering the interactions between Rydberg atoms. Now, let's discuss what happens when light propagates through an atomic ensemble where both phenomena, dipole interactions between atoms and EIT, are present.

Based on eq. 2.27, we know that polaritons propagating in an EIT medium have an admixture of the Rydberg state. This implies that polaritons should also interact with each other and, interestingly, these polariton-polariton interactions allow us to engineer optical nonlinearities, which can even occur at the single-photon level in extreme cases (by which we should understand that any subsequent photon arriving to the ensemble propagates under different conditions than the first photon).

To understand this behavior intuitively, let's consider a pair of photons sent into the medium one after the other. The first photon propagates through the medium as a polariton, with a reduced group velocity v_g. When the second photon enters the medium, the Rydberg level is shifted due to the van der Waals potential of the already existing polariton. If the second photon arrives close enough to the first photon, within the so-called blockade time $\tau_b = r_b/v_g$, where r_b is the blockade radius, the dipole interaction shifts the Rydberg level so much that the control field is no longer resonant with the $|e\rangle$ to $|r\rangle$ transition. Then, the second photon sees an ensemble of two-level atoms to which it is resonant and, therefore, will likely be scattered. Consequently, the probability of multiple photons simultaneously exiting the medium is suppressed.

This phenomenon was observed as a decrease in EIT transparency with increasing probe power [109]. Subsequently, it was discovered that light leaving a Rydberg-EIT (rEIT) ensemble exhibits strong antibunching features [58], indicating that the photons are well-separated in time by at least the blockade time. In our research group, we demonstrated that the nonlinear response can be enhanced by storing photons in the Rydberg state [80], as it extends the interaction time and selectively filters out photons that did not interact with the ensemble.

To explain these observations, a significant body of theoretical work has been developed, just to give some examples [41, 110–112]. For a didactic introduction to the theoretical framework commonly used to describe interacting Rydberg polaritons, I recommend referring to the work by Bienias et al. [113].

Moreover, more exotic phenomena have been observed. For example, resonant enhancement of three-body losses has been documented [72]. Furthermore, when deviating from single-photon resonance, a plethora of interesting and non-trivial effects emerge, such as conditional phase shifts [114, 115], three-body interactions and bound states [73, 74], as well as repulsive and attractive photonic interactions [76].

Chapter 3

Experimental setup

In this chapter, I'll walk you through our experimental setup, which is specifically designed for creating and manipulating disordered ensembles of Rubidium atoms and exciting them to Rydberg states. We use standard cold-atomic techniques and some custom-made solutions tailored to the specific needs of our experiment.

To achieve nonlinear effects at the single-photon level, we have a few requirements to fulfill. First, we need a strong interaction between light and matter, which means our optical depth must be large. Second, we ensure that the atoms are tightly confined so that only one, or at most a few, blockade spheres can fit within the atomic ensemble. Lastly, we require our excitation lasers to have small linewidths and good frequency stability to address narrow atomic transitions.

In our experiment, we achieve a dense and compact atomic cloud of ^{87}Rb atoms by loading them into a dipole trap from a magneto-optical trap. This provides us with the necessary conditions to proceed with an interrogation of the atoms. We turn off the dipole beam and introduce a probe beam with a counter-propagating coupling beam to excite them to a Rydberg level. Finally, the photons emitted by the system are detected using single-photon detectors, as discussed in more detail in ch. 4.

Many parts of the setup are only briefly discussed as they were already described in detailed in theses of my predecessors, Emanuele [116, ch. 4] and Auxi [117, ch. 3]. Part that were developed during my PhD are depicted in more detail.

3.1 Trapping and cooling the atoms

We use a fairly standard experimental setup to trap and cool ^{87}Rb atoms. We chose to work with ^{87}Rb because it is a relatively simple and easy-to-handle species, making it a good choice for studying the physics of Rydberg atom ensembles. The used techniques for trapping and cooling this atomic species are well-established and include magneto-optical trapping, optical molasses, and dipole trap. Our primary objective is to create a small cloud, comparable with the blockade radius, with an

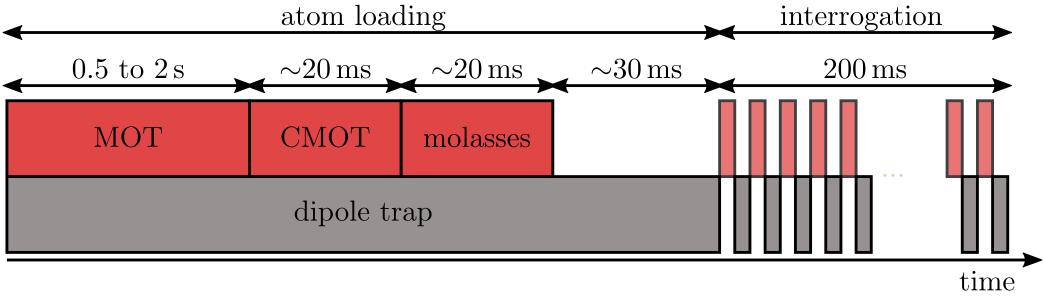

Figure 3.1: A typical experimental sequence. The experimental sequence begins with the atom loading phase, which includes magneto-optical trapping (MOT) followed by compressed MOT (CMOT) and optical molasses. The dipole trap is kept on during this entire process. After the loading phase is complete, the interrogation phase begins. During this phase, the dipole trap is pulsed and, depending on the experiment, the probe light may also be used.

optical depth much larger than 1. In our setup, we typically work with a cloud that has a diameter of about 15 µm (FWHM) and optical depth 10 to 14. To achieve this, we follow a typical experimental sequence, which is illustrated in fig. 3.1, and described in the following sections.

3.1.1 Magneto-optical trapping and cooling

Below, I will provide a brief overview of the main mechanism of laser cooling and then describe the different stages of the loading phase. For a more comprehensive explanation, I recommend reading Foot's textbook [118, ch. 9] or the theses of my predecessors, Auxi [117, sec. 3.4] and Emanuele [116, sec. 4.1].

Laser cooling techniques rely on radiation forces to trap and cool atoms. These forces arise from the scattering of photons, which carry momentum $\hbar\boldsymbol{k}$, where $\boldsymbol{k}$ is the laser field wave vector, that is transferred to the atoms, when a photon is absorbed. Since the remission of the photons happens in random directions, there is a net force that slows down the atoms. By shining three pairs of counter-propagating red-detuned laser beams along the Cartesian axes, one can slow down the atoms in all three directions, achieving so-called optical molasses[1]. The ultimate limit for this kind of cooling is equal to a few times the recoil temperature, T_r which is given by [118, p. 208]

$$k_B T_r = \frac{(\hbar|\boldsymbol{k}|)^2}{m_A}, \tag{3.1}$$

where k_B is the Boltzmann constant and m_A is the atomic mass. For ^{87}Rb, $T_r = 362\,\mathrm{nK}$. A comprehensive explanation of this effect can be found in [102, sec. 1.4.2]

---

[1] At first glance, one might think that the forces coming from counter-propagating laser beams would balance each other out and have no effect on the atoms. However, this is only the case for stationary atoms. When the Doppler effect is taken into account for moving atoms, it can be shown that the forces become imbalanced. The resulting force resembles friction, with a magnitude proportional to the atom's velocity.

or [118, sec. 9.1].

Our typical atom loading phase begins with a magneto-optical trap (MOT), which consists of a magnetic field gradient generated by two coils arranged in an anti-Helmholtz configuration and the six laser beams described earlier[2]. This setup not only slows down the atoms, but also traps them in a region of zero magnetic field [118, sec. 9.4]. After a variable time, typically around 500 ms, we obtain a dilute cloud of atoms with a diameter of approximately 2.5 mm (FWHM) and a temperature of 300 µK. Typically, we do not focus much on the specific parameters of this loading stage. Instead, we optimize it by monitoring the brightness of the cloud's fluorescence.

The next phase in our experiment is the compressed magneto-optical trap (CMOT), which enables us to increase the atomic density beyond that achieved in the MOT without significantly raising the cloud temperature [119]. To achieve this, we gradually increase the magnetic field gradient to confine the atoms in a tighter potential and decrease the intensity of the laser beams to reduce the fluorescence radiation pressure. Again, we optimize it by monitoring the brightness of the cloud's fluorescence and, crucially, ensuring that its center aligns with the center of the dipole trap.

The loading phase concludes with optical molasses, which enables us to reduce the temperature of the cloud at the expense of losing some atoms. During this phase, the magnetic field gradient is turned off, which is necessary for the molasses to work but leads to the loss of trapped atoms, and the laser beam power is further reduced. As a result, we obtain a cloud with a diameter of around 1.3 mm (FWHM) and a temperature of approximately 35 µK, as confirmed by a time-of-flight measurement [120, appendix A].

3.1.2 Dipole trap

In order to obtain a small cloud that is comparable with the blockade radius, we use a far-detuned dipole trap. This trap also allows us to interrogate the atoms for long periods of time without losing optical depth. The dipole trap is kept on during the whole loading phase and for another 30 ms so that all the atoms that did not fall into the dipole trap would have time to fly away (due to the gravity).

Atoms in the dipole trap experience attractive or repulsive dipole force, which is a result of the gradient of the intensity of the laser light. The explanation of this force is beyond the scope of this thesis, but a didactic explanation can be found in [118, sec. 9.5] or in [102, sec. 1.4.1].

In general, the magnitude of the dipole potential depends linearly on the laser

---

[2] To be precise, we use one additional laser in our setup, called a repumper. Since ^{87}Rb has two ground states and only one of them participates in the MOT process, the repumper ensures that all the atoms are in the desired ground state.

intensity, I

$$U_{\text{dipole}} \approx \frac{\hbar\Gamma^2}{8\delta}\frac{I}{I_{\text{sat}}}, \tag{3.2}$$

where we assumed that there is one dominant transition (the dipole trap laser is detuned far from resonance, but much closer to one specific resonance than all the others)[3]. Γ stands for the spontaneous decay rate of this transition, δ is the laser detuning (negative for a red-detuned light), and I_{sat} is the transition saturation intensity. If δ takes a negative value, the potential energy U_{dipole} exhibits a minimum at the location of highest intensity, i.e. it forms a potential well that attracts atoms. However, there is another important factor to consider, which is the scattering rate, R_{scatt}

$$R_{\text{scatt}} \approx \frac{\Gamma^2}{8\delta^2}\frac{I}{I_{\text{sat}}}. \tag{3.3}$$

This rate determines how often the atoms absorb photons and effectively how quickly get heated up. Fortunately, the scattering rate scales differently with the detuning, δ than the dipole potential, so for sufficiently far-detuned light, the scattering is negligible.

The choice of the dipole trap is typically dictated by the trade-off between the dipole potential depth and the scattering rate, as well as the availability of high-power lasers. In our experiment, we found that using a laser with a wavelength of 852 nm was a good choice.

During my PhD, we made a significant improvement to our setup by switching from a single-pass dipole trap to a crossed dipole trap. This change allowed us to reduce the cloud size from 40 µm to 15 µm (FWHM diameter) while increasing the optical depth from 9 to 18 (at 2 s MOT loading time).

However, we had to adapt an awkward geometry for the dipole trap due to lack of space in the setup. The original beam was kept at a shallow angle of 21° with respect to the probe (in the horizontal plane), and we added an independent vertical beam intersecting both the first dipole trap beam and the probe beam at a right angle, as shown in fig. 3.2. The beams have powers of around 820 mW and 990 mW, respectively. The horizontal beam is cylindrical and focused to a waist of $w_0 = 34\,\mu\text{m}$, while the vertical beam is elliptical and has waists of $w_{0,x} = 34\,\mu\text{m}$ and $w_{0,y} = 68\,\mu\text{m}$. The ellipticity of the vertical beam simplified the dipole trap's alignment in the vacuum chamber. Moreover, acousto-optical modulators that gate the dipole trap beams are driven at two different frequencies to avoid interference between the fields. For the above values and taking into account that both beams are linearly polarized, we calculated the trap potential to be $U_{\text{dipole}}/k_B \approx 330\,\mu\text{K}$, which is deep enough to observe long trapping times, as shown in fig. 3.3(right).

To avoid anti-trapping of Rydberg atoms and the inhomogeneous AC Stark shift, both discussed in sec. 5.2.1, the dipole trap is turned off when atoms are probed,

---

[3] This assumption does not hold true for ^{87}Rb since both D_1 and D_2 lines contribute to the dipole potential. Nonetheless, we mention this consideration for explanatory purposes rather than for computing precise values.

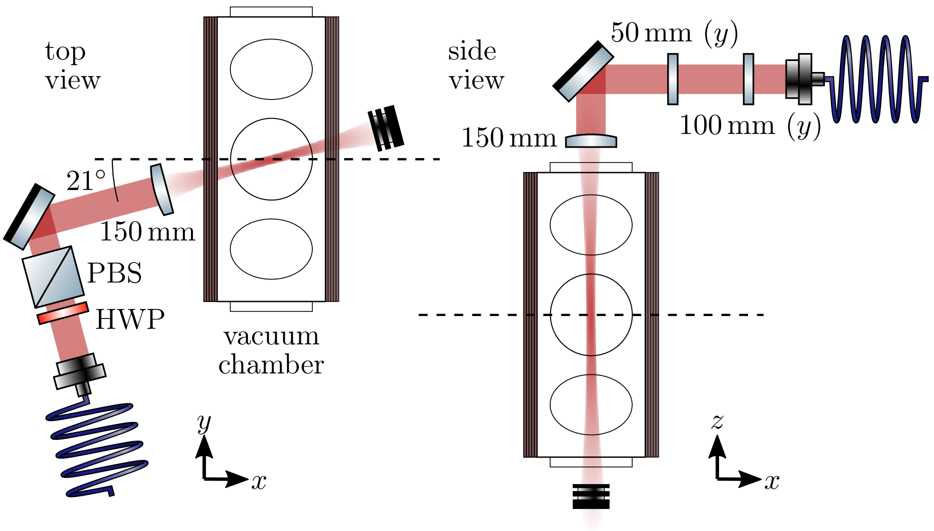

Figure 3.2: Geometry of the dipole trap. From a top view, the dipole trap's original horizontal beam is visible, intersecting with the probe mode (represented by a black dashed line) at an angle of 21°. In the side view, only the vertical beam can be observed. Before being focused with a 150 mm-focal-length lens, the vertical beam passes through a telescope consisting of two cylindrical lenses, which reduces the beam size in the y direction and results in an elliptical beam shape. This simplifies the dipole trap's alignment in the vacuum chamber.

typically for 2.5 µs. It means that both dipole-trap beams are pulsed during the interrogation phase, with a duty cycle of around 50 %.

Using the method described above, we achieve a cloud that meets our requirements. The cloud's size of 15 µm (FWHM) is comparable to the blockade radius and has a sufficient density to give an optical depth much larger than 1. Moreover, depending on the specific experiment's needs, we can easily adjust its optical depth between 0 and 18 by varying the duration of the MOT, as demonstrated in fig. 3.3(left).

The reported cloud size might be surprising when compared to the dipole trap beam sizes. One would anticipate that the size of the potential well formed by the intersection of the two dipole trap beams, known as the dipole trap potential well, would have a diameter of $2w_0 = 68\,\mu\text{m}$. However, the reported size of the cloud is much smaller than this. There are two reasons for this disparity.

Firstly, the beam waists, denoted as w_0, are typically defined as the half-width at $1/e^2$ of the light intensity, which is related to the full width at half maximum (FWHM) by the equation $2w_0 = 1.699\,\text{FWHM}$. Therefore, the estimated potential well size based on the beam waists appears larger.

Secondly, the cloud size is usually smaller than the trap well size because the cloud does not completely fill the potential well. This can be described by the *filling factor* $\zeta \equiv k_B T / U_{\text{dipole}}$, where T represents the temperature of the cloud and U_{dipole} corresponds to the depth of the dipole trap potential well. The size of the

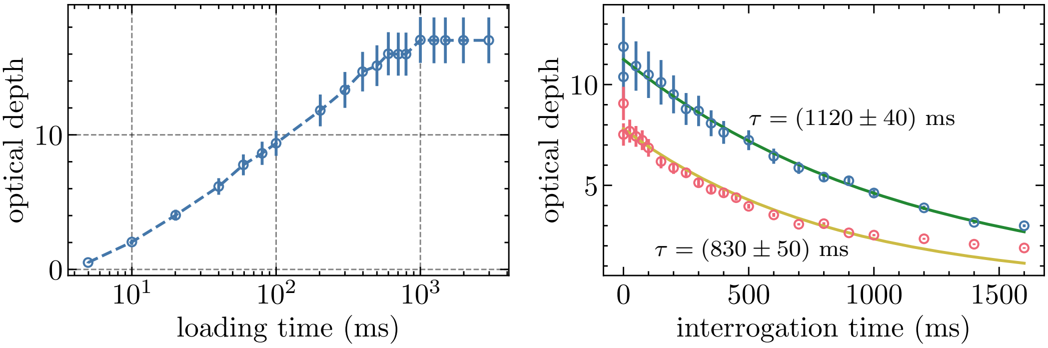

Figure 3.3: (left) Optical depth of the cloud hold in the dipole trap depends on the duration of MOT (loading time). (right) Optical depth as a function of the interrogation time for two different loading times, 60 ms (red circles) and 150 ms (blue circles). Optical depth decreases during the interrogation time (we typically work with interrogation time of 200 ms). The main reason for this is the fact that the dipole trap is pulsed, as the scattering rate is estimated to be very low, less than 10 events per second. The solid lines are fits to function $Ae^{-\tau}$. In both plots, optical depth was measured with the probe transmission.

atomic cloud, denoted as w_a, is related to the trap size (under the harmonic potential approximation) by the equation $w_a = \sqrt{\zeta} w_0$ [121, sec. 3.3.1]. Taking into account the measured values from our experiment and considering the distinction between FWHM and $1/e^2$ widths, the expected cloud size is calculated to be approximately 13 µm, which aligns well with the observed value.

3.2 Laser system

Now that we have discussed how we prepare our atomic ensemble, let's turn our attention to the technicalities of our laser system. To create all the necessary fields, which are schematically shown in fig. 3.4, we need four different lasers at different wavelengths. Some of these lasers have already been described in detail by my predecessor, Emanuele [116, sec. 4.2], so I will only mention them briefly here.

The lasers we use are: a fiber laser at 1560 nm whose light is frequency doubled to obtain the 780 nm light for the probe and to drive the MOT, a diode laser at 780 nm which serves as the repumper, a diode laser at 479 nm that allows us to excite our atoms to Rydberg states, and a diode laser at 852 nm which serves as the dipole trap. We will now describe each laser in more detail and discuss its role in our experimental setup.

3.2.1 iXblue laser at 780 nm

The MOT light and the probe light used in our experiment are derived from a 780 nm laser from iXblue and addresses the $F = 2$ to $F' = 3$ transition of the D_2 line. Its

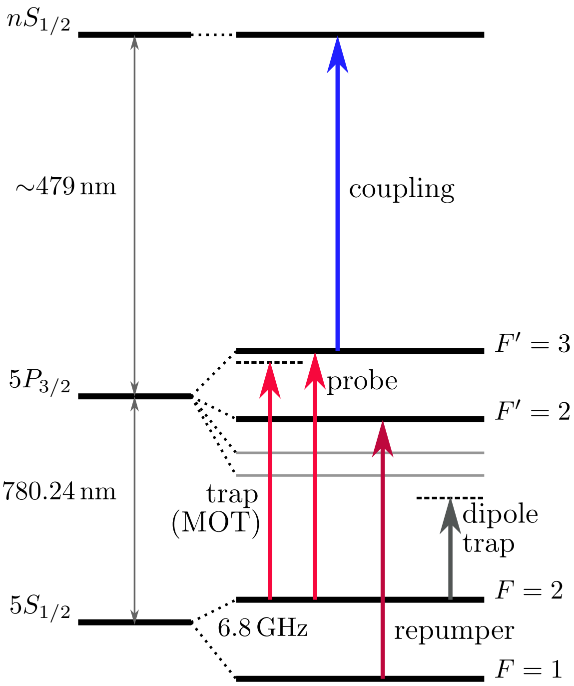

Figure 3.4: Schematic representation of the fields involved in our experiments and the relevant atomic transitions. The dipole trap light is far off-resonant to any relevant transition and is represented only symbolically.

frequency is stabilized with modulation transfer spectroscopy (MTS), as explained in detail in sec. 3.3.1.

The laser is based on an amplified fiber laser at 1560 nm, whose light is then converted to 780 nm using a fiber second-harmonic-generation (SHG) chip. We specifically chose this laser for its overall stability and low noise, which is particularly relevant for high-fidelity π-pulses, as discussed in sec. 5.2. The locking setup, described in sec. 3.3, also relies on the stability of the laser.

This laser is claimed to have a narrow linewidth and very low phase noise at higher frequencies[4]. The linewidth of the 1560 nm laser, according to the test sheet, is less than 3 kHz, which means that we expect a linewidth of less than 6 kHz at 780 nm. The laser delivers more than 950 mW of power at 780 nm, which is more than sufficient for our experimental needs. Due to its limited tunability of around 24 GHz, this laser is only suitable for addressing the D_2 line of ^{87}Rb. Overall, we are very happy with this laser, as it has proven to be reliable and stable over long

---

[4] We have not independently verified these claims, but we have found its overall performance to be very good, especially when compared to our previous diode laser, which was also supposed to have a narrow linewidth of few tens of kHz.

periods of time.

I'd like to note that the initial experiments discussed in this thesis were carried out using a different diode laser[5], which had its light amplified by an optical amplifier[6]. This laser notoriously mode-hopped, and its controller unintentionally introduced environmental RF noise into the laser light. Furthermore, its beam alignment was consistently shifting, requiring frequent realignment of the fiber in-coupling. Due to these challenges, we decided to invest in a more costly yet more reliable 780 nm laser system described above.

3.2.2 Repumper laser

We generate the repumper light using a home-built laser which is based on a distributed feedback diode laser from EagleYard[7]. It delivers up to 80 mW with linewidth of around 2 MHz. The repumper laser addresses the $F = 1$ to $F' = 2$ transition and its frequency is actively stabilized using the frequency of the trap laser as a reference. We achieve this by employing light beating spectroscopy [122]. The RF signal sent to an AOM allows us to control both the frequency and intensity of the repumper laser. For more details on the laser construction and the particular implantation of the lock, see Emanuele Distante's thesis [116, sec. 4.2.2].

3.2.3 Coupling laser

We use a commercial SHG laser from Toptica[8] to provide the coupling light at a wavelength of 479 nm, which connects the intermediate excited state to the Rydberg state, and its wavelength can be adjusted to address different Rydberg states. It's composed of a tunable external-cavity diode laser at 959 nm, an amplifier and an SHG cavity, and delivers up to 340 mW of power at 479 nm. Although it is not inherently low noise, we employ a locking setup described in sec. 3.3 to achieve stable and low-noise performance. This is important because any noise in the laser introduces dephasing, and the coupling laser needs to be stable in its central frequency since the transitions to Rydberg levels are narrow. The coupling light intensity and frequency are controlled with a double-pass AOM.

3.2.4 Dipole trap laser

The dipole trap light at 852 nm is generated by a home-built laser and then amplified using two free-space amplifiers from Toptica[9]. The laser is based on a distributed feedback diode laser from EagleYard, with the design similar to the repumper laser, and produces an output power of 40 mW which acts as a seed for the amplifiers.

---

[5] Radiant Dyes NarrowDiode

[6] Toptica BoosTA

[7] EYP-DFB-0780

[8] Toptica TA/DL SHG pro

[9] Toptica BoosTA pro

The amplified beams with 2.2 W and 2.6 W of power are then gated by two AOMs driven at different frequencies to prevent interference between them. Since the dipole trap laser is not resonant with any atomic transition, it does not require frequency stabilization.

3.3 Locking setup

In the previous section, we explored the laser system used in our experimental setup. However, in order to effectively address the narrow atomic transitions[10], it is crucial to stabilize the absolute frequency of our lasers. Additionally, to minimize unwanted dephasing effects, we employ active noise reduction techniques for the coupling laser light (for a discussion on various dephasing effects, see sec. 5.2).

During my PhD, we made significant changes to how we lock our lasers. The previous iteration of setup had notable limitations arising from the chosen spectroscopic methods used to stabilize the 780 nm and 479 nm lasers.

For the 780 nm laser, we used to use frequency modulation spectroscopy (FMS), which offers a strong error signal. However, the presence of a non-zero offset made it prone to drifting, resulting in shifts of the locking point. This effectively translates to a drift of the laser frequency, which we want to avoid.

The 479 nm laser was locked using EIT spectroscopy to a Rydberg level in a vapor cell. However, due to the diminishing dipole moment of higher Rydberg levels, the error signal strength was very weak. Moreover, we were loosing some power of 479 nm light in this setup, which anyway is limited. Furthermore, the lock's bandwidth was quite restricted, making it unsuitable for narrowing the laser's linewidth.

Our current locking system was designed to solve these issues and is composed of three interconnected elements. The first element is modulation transfer spectroscopy (MTS), which allows us to lock the probe laser to the desired atomic transition, $F = 2$ to $F' = 3$. The second element of our locking setup is an actively stabilized cavity. The length of this cavity is actively controlled using the Pound-Drever-Hall (PDH) method, which relies on a feedback loop referenced to the probe light. This cavity serves as a stable reference for the Pound-Drever-Hall lock of the 960 nm seed laser used in the coupling process, the third element of our locking system.

By cascading these three locks, we achieve a highly stable and precisely controlled frequency for the probe and coupling lasers. In the following sections, we will delve

---

[10] It's truly impressive to consider the level of precision we aim for in laser stabilization. Take the probe light, for instance, with a frequency of around 3.84×10^{14} Hz. We strive to make it more stable than the transition width, which is about 6.07×10^{6} Hz. That's nearly eight orders of magnitude! But wait, the transitions to the Rydberg states are even narrower, estimated to be only about 2×10^{4} Hz. And the frequency difference between the ground state and the $n = 90$ Rydberg state is 1.01×10^{15} Hz, which amounts to almost eleven orders of magnitude of difference. It is a bit like having a ruler as long as the distance from Earth to Sun and operate it with a mm precision. I find it remarkable how precise our laser stabilization needs to be to explore such intricate atomic phenomena.

into the details of each locking element, explaining their principles and the techniques employed to achieve the desired stability and accuracy in frequency control.

3.3.1 Modulation transfer spectroscopy

We employ modulation transfer spectroscopy (MTS) [123] as a robust method to lock our probe laser and obtain a highly stable absolute frequency reference. MTS operates on the principle of four-wave mixing with a pump beam and a probe beam, utilizing a frequency modulation imposed on the pump light to transfer the modulation to the probe light. By demodulating the beating signal between the probe carrier and the imprinted sidebands, we extract an error signal that serves as feedback on the laser current to maintain laser frequency stability.

One of the advantages of MTS is its offset-free error signal, which makes it a favorable choice compared to frequency modulation spectroscopy (FMS) in many applications, as one can see in fig. 3.5(left). As a result, the zero-crossings of the MTS signals align precisely with the corresponding atomic transitions, assuring the accuracy of the frequency stabilization.

In the following paragraphs, I provide an intuitive explanation of the underlying physics that gives rise to the characteristic modulation transfer spectroscopy (MTS) signal. I then provide the details of our implementation and the optimization procedures we undertook to enhance its performance.

Four-wave mixing in modulation transfer spectroscopy

To understand the principles of MTS, let's consider a simple toy model of a two-level atom. This model is sufficient to grasp the underlying physics of MTS. In a typical MTS setup (shown in the top right of fig. 3.5), a modulated pump beam counter-propagates with an unmodulated probe beam.

In our setup, we shift the pump carrier frequency by $2\omega_{\mathrm{aom}}$ relative to the probe frequency. This allows us to effectively lock our laser away from the atomic resonance, which is necessary when using AOMs to control the laser beams[11].

For simplicity, let's limit our consideration only to the first sidebands. Additionally, we need to account for the motion of the atoms; we denote their velocities as v. As the pump and probe counter-propagate, they will experience opposite Doppler shifts for the same velocity class.

All in all, the pump field carries the following frequencies (as seen from a perspective of an atom) $\omega_{\mathrm{pump}} = \{\omega_{\mathrm{c}} + kv,\ \omega_{\mathrm{c}} + \Omega_{\mathrm{mod}} + kv,\ \omega_{\mathrm{c}} - \Omega_{\mathrm{mod}} + kv\}$, where $\omega_{\mathrm{c}} = \omega - 2\omega_{\mathrm{aom}}$ is the pump carrier frequency, ω is the laser frequency, $k = \omega/c$ is the corresponding wave vector length and Ω_{mod} is the modulation frequency. On the other hand, the counter-propagating unmodulated probe light has a frequency of $\omega_{\mathrm{probe}} = \omega - kv$.

---

[11] It's worth noting that we could have shifted both fields in frequency to keep the laser off-resonant with the atomic transition, but this would have required an AOM operating at a different frequency, which we didn't have available at the time of building the setup.

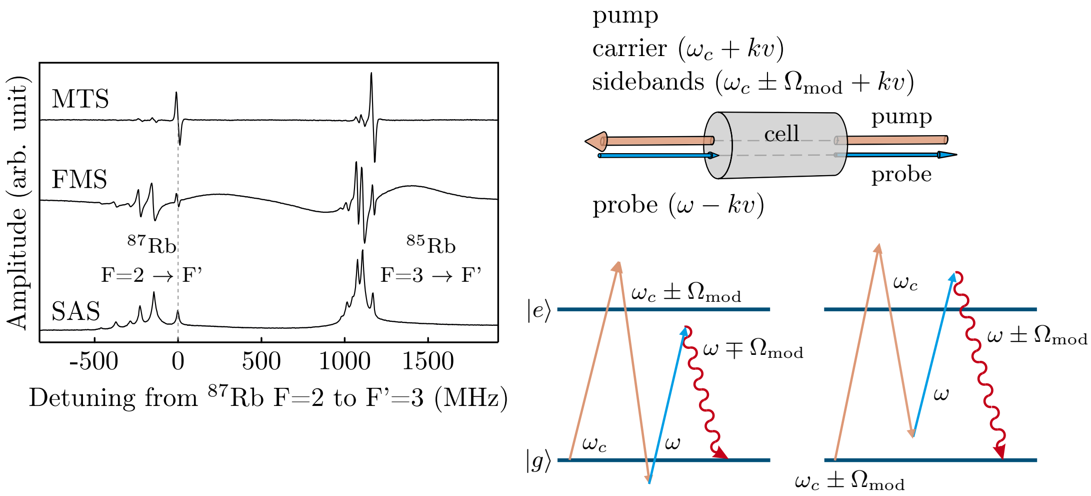

Figure 3.5: (left) Typical MTS error signal compared to a typical frequency modulation spectroscopy (FMS) error signal. Saturated absorption spectroscopy (SAS) signal is given for reference. One can clearly see in the MTS signal strongly pronounced features from the cycling transitions. Figure was reproduced after [123]. (right top) Schematic diagram of modulation transfer spectroscopy. Doppler shift seen by the atoms have opposite signs for the pump and the probe light. (right bottom) Schematic representation of the FWM process in MTS for a two-level atom. There exist two distinct possible process that give rise to two different resonance conditions. Doppler shifts were omitted for the clarity of the image. Both were adopted from [124].

In this system, there are two possible four-wave mixing (FWM) processes occurring, as depicted in the bottom right of fig. 3.5. The maximum intensity of the FWM process is expected when both single-photon absorption and three-photon absorption are resonant with the atomic transition for the same velocity class [125]. We can consider the left case (of the two in the bottom right of fig. 3.5), which leads to a simple set of equations:

$$\begin{cases} \omega_0 = \omega_{\text{c}} + kv \\ \omega_0 = (\omega_{\text{c}} + kv) - (\omega_{\text{c}} \pm \Omega_{\text{mod}} + kv) + (\omega - kv) \end{cases} \tag{3.4}$$

Here, ω_0 represents the atomic resonance frequency. Solving these equations yields a unique resonance condition:

$$\omega = \omega_0 + \omega_{\text{aom}} \pm \frac{\Omega_{\text{mod}}}{2} \tag{3.5}$$

for a specific velocity class:

$$kv = \pm\frac{\Omega_{\text{mod}}}{2} - \omega_{\text{aom}}. \tag{3.6}$$

For the right case, a similar analysis leads to $\omega = \omega_0 + \omega_{\text{aom}} \mp \Omega_{\text{mod}}$.

There are two important observations to make. Firstly, despite the pump light being shifted by $-2\omega_{\text{aom}}$, the laser light, when locked to the MTS signal, is only ω_{aom} away from resonance. Secondly, the two different processes result in two distinct resonance conditions. This leads to a doublet structure that may decrease the slope of the error signal or even invert its slope [123]. To mitigate this, it is advisable to keep the modulation frequency below the transition linewidth. However, it should not be too low, as it can limit the lock bandwidth and might introduce undesirable amplitude modulation that affects the error signal [126].

When working with real atoms that have more than just two levels, we observe that MTS provides a strong signal specifically for cycling transitions, as depicted in fig. 3.5(left). This is because the atoms have a longer interaction time with the laser beam for cycling transitions compared to non-cycling transitions, as explained in [124]. For a detailed quantum mechanical analysis of MTS in ^{87}Rb, I suggest referring to [127].

MTS setup

Let's now explore our MTS setup, which is illustrated in the left panel of fig. 3.6. We guide light from the trap laser into a polarization-maintaining fiber, ensuring careful alignment to minimize power fluctuations in the MTS setup. The light is collimated[12] to a beam with a diameter of 1.6 mm. By adjusting the angle of a half-wave plate (HWP), we can control the power ratio between the reflected probe beam (via a polarizing beam splitter, PBS) and the transmitted pump beam.

To enhance the signal, we enlarge the probe beam diameter by a factor of 3, before directing it to the Rubidium reference cell[13]. The cell is wrapped in mu-metal to minimize effects of magnetic field variations, and passively heated up to increase atomic density[14]. On the other hand, the pump beam undergoes frequency shifting using an acousto-optic modulator (AOM)[15] in a double-pass configuration, resulting in a frequency shift of 454 MHz. To match the expected mode size and reduce the optical path length, we utilize an uncollimated telescope prior to the AOM. This particular frequency shift was chosen to align with the frequencies of existing AOMs in our setup. To maintain frequency stability, the AOM is driven by a highly stable fixed-frequency source[16].

---

[12] Schafter und Kirchoff 60FC-4-8A-07

[13] Thorlabs GC19075-RB

[14] The exact temperature to which we heat up the cell is unknown. To determine the optimal temperature, we performed an optimization procedure by adjusting the current flowing through the heaters and monitoring the amplitude of the error signal. For this purpose, we utilize flexible heaters from Omega Engineering, the KHLVA-102/10 model. These heaters are designed to minimize the magnetic field they generate. To further enhance magnetic field cancellation, we employ a configuration where two heaters are stuck to each other with the current flowing in opposite directions.

[15] AA Opto-electronic MT200-B100A0.5-800

[16] AA Opto-electronic MODA227-B51k-34

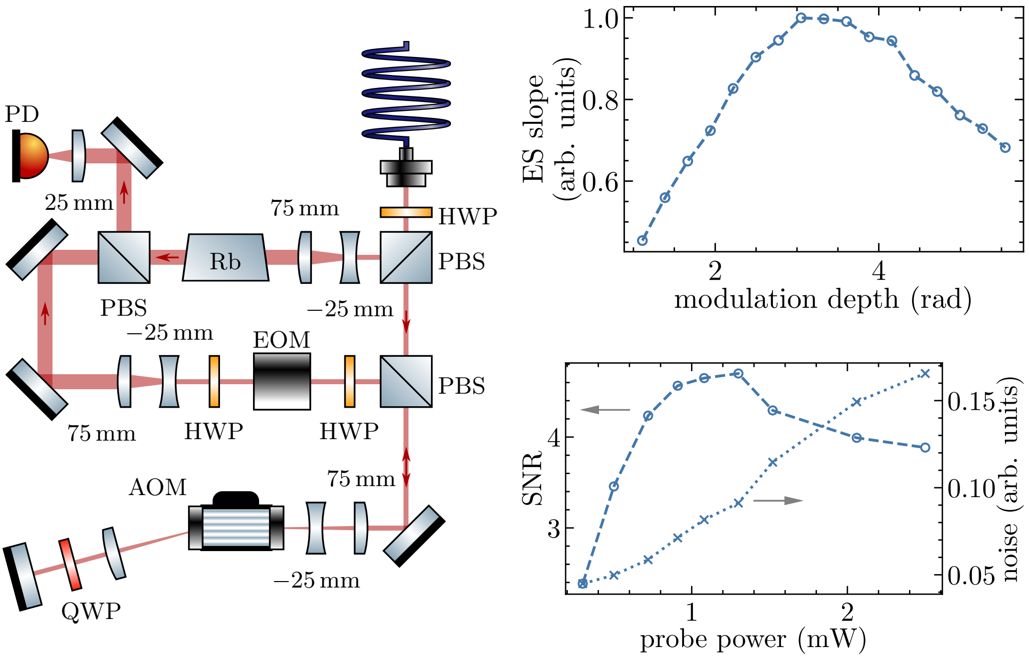

Figure 3.6: (left) Schematic representation of the modulation transfer spectroscopy setup. Pump light first goes to the AOM where its frequency is shifted by 454 MHz and then passes through the EOM which imprints sidebands at 4.5 MHz. The side bands are transferred to the probe light in FWM process inside the Rb cell. Beating of the carrier frequency with the side bands is detected at the amplified photodetector (PD). (right) Optimization curves of the MTS lock. (top) The error signal (ES) slope as a function of the EOM modulation depth. The modulation depth of the maximum slope agrees well with the prediction of [128]. (bottom) The ES-slope-to-noise ratio (SNR) and noise as a function of the probe power. As expected, the noise is proportional to the probe power (it is given in units proportional to $V/\sqrt{Hz}$). Similar results were presented in [129].

Next, the pump beam passes through a wedged electro-optic modulator (EOM)[17], which has a resonance frequency of 4.5 MHz. This specific frequency was selected to optimize the steepness of the error signal, as discussed in the optimization section sec. 3.3.1. The modulation signal is generated by a Red Pitaya[18] and amplified with a medium-power amplifier[19]. The wedged crystal design of the EOM helps minimize the etalon effects, which have been reported to impact MTS performance [129].

Once the sidebands are imprinted, the pump beam propagates through the Rubidium cell, where the process of four-wave mixing (FWM) takes place. The probe beam, with the sidebands transferred, is reflected off a PBS and directed to a photodetector (PD)[20]. To separate the saturated absorption spectroscopy (SAS)

---

[17] Qubig PM7-NIR_4.5

[18] STEMlab 125-14 Low Noise

[19] Mini-Circuits ZX60-100VH+

[20] Thorlabs PDA10A-EC

signal (DC component) from the MTS signal (AC component), the PD output is fed through a bias-tee[21]. The MTS signal is then amplified using a low-noise amplifier[22] and fed into a Red Pitaya, which internally mixes it with the modulation signal. This process generates the error signal, which is utilized to generate a feedback signal to the laser, also within the Red Pitaya. To control the Red Pitaya, we employ the Linien software [130] and we are very satisfied with its performance[23]!

Optimization of the MTS error signal

Let's now turn our attention to the optimization of an MTS lock, where two key parameters come into play: the slope of the error signal (ES) and the presence of residual amplitude modulation (RAM).

The ES slope governs the sensitivity of the lock to laser frequency changes and determines the minimum detectable frequency shift that the feedback loop can effectively track. Thus, the ratio of the ES slope to the noise floor can be regarded as the signal-to-noise ratio (SNR), which we aim to maximize to enhance the lock's performance.

RAM is a common phenomenon that can impact various locking methods, albeit with different underlying causes[24]. Many locking techniques rely on demodulating a signal from a photodiode, which ideally should exhibit no component at the modulation frequency (or they perfectly cancel each other due to opposite phases) when the laser light precisely matches the desired frequency. In this ideal case, the ES would be zero. However, due to spurious effects, the signal may undergo amplitude modulation at the modulation frequency, resulting in an offset in the demodulated ES. This unintended modulation is known as residual amplitude modulation (RAM).

Unfortunately, RAM can be particularly challenging to deal with, as its strength often fluctuates over time for unknown reasons. Moreover, monitoring RAM during lock operation is virtually impossible. Therefore, our objective is to minimize RAM as much as possible to ensure the stability and reliability of the lock.

To maximize the ES slope, we followed an approach presented in [128]. Their work allows finding the optimal modulation depth for a given modulation frequency. Keeping in mind challenges associated with achieving large modulation depths using an EOM (for our EOM the maximum modulation depth is less than 6), as well as the need to avoid resolving the doublet structure discussed in the previous section, we chose to modulate our pump at a frequency of 4.5 MHz. We then optimized the ES slope by adjusting the modulation depth, as shown in the top right of fig. 3.6.

---

[21] Mini-Circuits ZFBT-6GW+

[22] Mini-Circuits ZFL-500LN+

[23] We tried different available pieces of software for Red Pitaya suitable for spectroscopy and locking - PyRPL [131] and Lock-in+PID [132], and we found Linien to be the easiest and most reliable of them.

[24] It is worth noting that the issue of RAM primarily arises when one is concerned about the absolute frequency of the laser light. However, if the purpose is simply to narrow the linewidth using techniques like Pound-Drever-Hall (PDH) locking, RAM becomes less of a concern.

The next step in our optimization process was to adjust the probe power to maximize SNR, as discussed in [129]. While increasing the probe power is expected to increase the ES slope, it also leads to higher noise due to power fluctuations. Therefore, it was important to examine how the SNR behaved with varying probe power. We recorded the ES slope and the mean power spectral density (PSD) of the ES within the frequency range of 50 to 150 kHz for several probe power values, as illustrated in fig. 3.6 (bottom right).

Having optimized the ES slope, we turned our attention to RAM. The problem of RAM in MTS has been extensively discussed in literature [129, 133, 134] and the key takeaway is that the pump light sidebands' amplitudes should be symmetrical, and they should be uniformly imprinted in space (in the pump beam cross-section).

To achieve this, we used an EOM instead of an AOM, which effectively solved the frequency symmetry issue[25]. However, the use of an EOM introduced another challenge: polarization RAM arising from the strong birefringence of the EOM crystal. Fortunately, this problem can be mitigated by using an EOM with a wedged crystal[26].

The second challenge, related to spatial uniformity, remains less understood. Typically, it is addressed by carefully aligning the probe and pump beams to achieve perfect overlap. In our experiments, we observed only a weak dependence of RAM on the alignment of the beams.

Possible improvements

Before we wrap up, I wanted to mention a few ideas we came across while researching and building the setup, which could potentially improve its performance.

Firstly, instead of heating the cell, which adds complexity and the risk of unwanted magnetic fields, we could have used a cell with a higher concentration of ^{87}Rb isotope, which would naturally enhance the signal.

To address the issue of spatially nonuniform sidebands, one interesting approach we found in a study by Long et al. [135] involved coupling the light from the electro-optic modulator (EOM) into a single-mode optical fiber. Another idea was to place the frequency-shifting acousto-optic modulator (AOM) before the spectroscopy setup, which would have simplified the alignment process and made the overall setup more compact.

In terms of stability, Long et al. [135] reported that working with a magnetically insensitive cycling transition, such as the $F = 1, m_F = 0$ to $F' = 0$ transition, along with a magnetic bias field, could potentially improve long-term stability. However,

---

[25] We encountered challenges in our initial setup where the sidebands were imprinted using an acousto-optic modulator (AOM), which posed two significant problems. Firstly, precise alignment of the probe and pump beams was crucial to mitigate RAM since the sidebands were not uniformly imprinted across the cross-section of the pump beam, as previously observed in [134]. Secondly, we faced long-term drifts that necessitated periodic realignment of the probe and pump beams.

[26] Another source of RAM might be etalon effects in the EOM, but this can be again mitigated by having a wedged crystal.

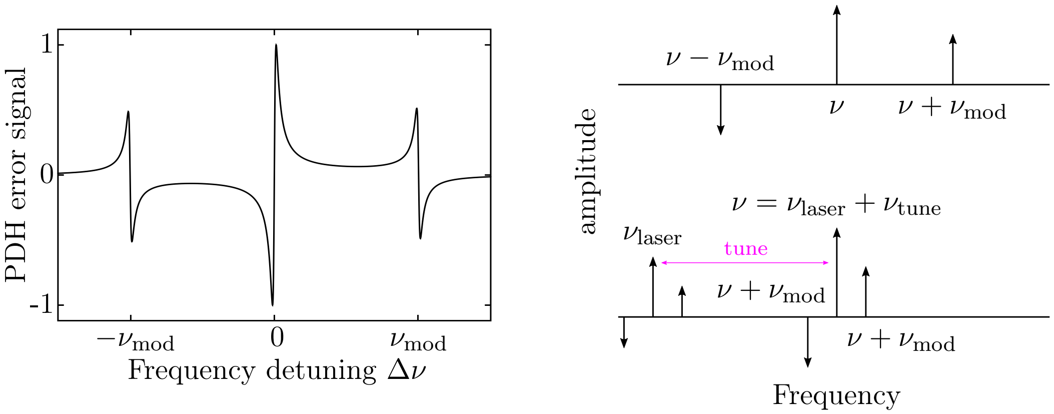

Figure 3.7: (left) A typical error signal of PDH technique for the optimal modulation depth of 1.08. One can appreciate the steepness of the error signal around the zero crossing point. (right) Graphical representation of the spectrum of a phase modulated light with modulation frequency ν_{mod} used in a typical PDH technique (top) and in offset sideband locking technique (bottom). Opposite pointing of the arrows represent opposite phases carried by the sidebands. In the offset sideband locking technique, one can tune the frequency shift ν_{tune} such that the sideband at frequncy $\nu = \nu_{\mathrm{laser}} + \nu_{\mathrm{tune}}$ becomes resonant with the cavity. Then this sideband becomes the usual carrier for the PDH technique depicted above.

an interesting counterpoint was presented by Lee et al. [129], who achieved even better stability with a simpler setup that didn't require a bias field.

Our MTS setup demonstrates very good performance, though, we are not able to directly verify its stability, as it would require either an additional highly stable laser or an ultra-stable reference cavity, which are currently unavailable to us. Nonetheless, the observed results indicate the robustness and effectiveness of our MTS implementation.

3.3.2 Actively stabilized reference cavity

The second element of our locking setup is an actively stabilized medium finesse optical cavity. This cavity acts as a frequency reference for the 960 nm seed light of the coupling laser, and we control its length using the Pound-Drever-Hall (PDH) method, locking the 780 nm light to the MTS lock. The optical cavity provides good stability with only small long-term drifts, as discussed in sec. 3.3.2.

A brief introduction to PDH method

To give a brief introduction to PDH and discuss important design considerations for a locking system, PDH's main objective is to reliably detect changes in cavity length or laser frequency. We achieve this by illuminating an optical cavity with phase-modulated light near its resonance and monitoring the reflected signal. We mix the reflected signal with the modulation frequency to generate the error signal (ES). An example of a typical PDH ES can be seen in fig. 3.7(left).

The magic of PDH lies in phase modulation[27]. Through phase modulation, we generate sidebands, as depicted in fig. 3.7(top right), with opposite phases – a crucial distinction compared to amplitude modulation, where the sidebands share the same phase. When the laser light perfectly matches the optical cavity's resonance, the reflected signal consists of the sidebands and a residual portion of the carrier. The beatings between the carrier and the sidebands cancel each other out due to their opposite phases, resulting in an ES value of zero. However, if the cavity length changes or the laser frequency drifts, one sideband is more strongly reflected while the other is less reflected. When the modulation frequency is in phase with the less reflected sideband, we observe positive values in the ES. Conversely, negative values are obtained in the opposite case. Thus, by employing phase modulation of the laser light, we can reliably determine the "direction" of changes in cavity length or laser frequency.

One can approximate the ES, denoted as ϵ, near the resonance as a linear function of detuning from the cavity resonance, $\Delta\nu$ [137]:

$$\epsilon = -8\sqrt{P_c P_s}\frac{\Delta\nu}{\delta\nu}, \tag{3.7}$$

where P_c and P_s represent the optical powers in the carrier and one of the first sidebands, respectively, and $\delta\nu$ corresponds to the cavity linewidth. To achieve optimal lock performance, maximizing the slope is crucial.

Two important points should be noted. Firstly, a narrower cavity linewidth leads to a steeper ES and higher responsivity of the locking system. However, it is important to consider that very high-finesse cavities may come with drawbacks such as increased cost and alignment challenges. Secondly, there exists an optimal modulation depth of 1.08, which maximizes the $\sqrt{P_c P_s}$ factor. For a more comprehensive theoretical treatment of the Pound-Drever-Hall (PDH) method, I recommend referring to the works of Black [137] or Nagourney [138, sec. 4.7].

The advantage of this method lies in the fact that the locking point remains independent of the laser power (at least in principle), and power fluctuations mainly affect the slope of the ES. Additionally, it's worth noting that the ES slope is proportional to the optical power, while shot noise only grows with the square root of power. Therefore, it's advantageous to provide more power to the locking setup for optimal performance.

However, achieving excellent long-term stability requires attention to certain small details. These considerations will be discussed in the following section.

---

[27] It took me some time to realize that phase modulation and frequency modulation are essentially the same thing, just parameterized differently, and both can be referred to as angle modulation. This concept is nicely explained in [136, sec. 6.1]. In the context of PDH, we primarily focus on phase modulation since it's easier to achieve high-quality phase modulation, mostly with EOMs, compared to frequency modulation.

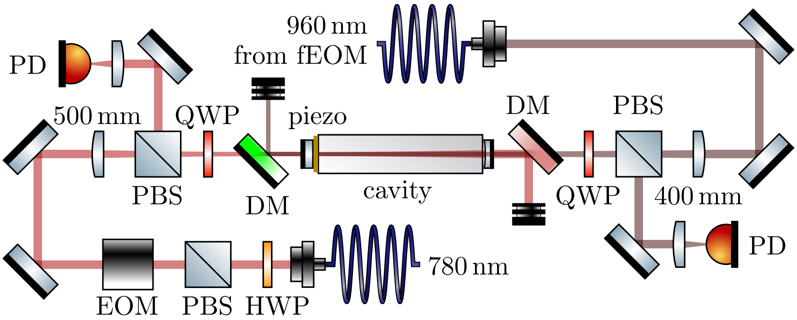

Figure 3.8: Schematic representation of the cavity setup. 780 nm and 960 nm impinge on the cavity from opposite sides and are separated by dichroic mirrors (DM). 960 nm light is modulated in the laser and in the fiber EOM (fEOM). 780 nm light, in contrary, is modulated by a free-space EOM. The left flat mirror is glued to a piezo actuator which glued to the cavity spacer.

Cavity setup

Our cavity setup is depicted on the right side of fig. 3.8. The 780 nm light is guided through a polarization-maintaining fiber and then collimated[28] into a 0.9 mm diameter beam. To avoid polarization residual amplitude modulation (RAM) (discussed later), a half-wave plate (HWP) is used to match the axis of the subsequent EOM[29]. The EOM is driven at 12.5 MHz with an amplified[30] signal generated by a Red Pitaya[31]. The beam is focused with a singlet lens of 500 mm focal length and directed towards the cavity. Numerical simulations[32] suggested it would give the best mode matching with the cavity mode.

A dichroic mirror[33] separates the reflected 780 nm light from the transmitted 960 nm light, which enters the cavity from the other side. The reflected light undergoes further reflection from a polarizing beam splitter (PBS) and is detected using an amplified photodetector (PD)[34]. The PD signal is then sent to a Red Pitaya, where it is mixed with the modulation signal to generate the error signal (ES). A home-built piezo driver[35], driven by a PID signal generated by Red Pitaya, controls

---

[28] AMS Technologies 355230-FCAPC-780

[29] Leysop 12.5MHz-RPM-LT-960

[30] Mini-Circuits ZX60-100VH+

[31] STEMlab 125-14

[32] With a very nice piece of software available online [139].

[33] Thorlabs DMSP805T

[34] Thorlabs PDA8A2

[35] Our design – great thanks to our electronic workshop!, is based on a design presented in [140]. It performs very well (better than the previously used piezo driver from Thorlabs) and with small modifications suits well our needs. We mostly simplified the design by getting rid of the DAC in favor of a manually set offset, to which an amplified and low-passed slow input is added. This modification is necessary due to the specification of Red Pitaya whose slow output is only 0 to 1.8 V, so needs amplification, and is generated with PWM, so requires a low-pass filter.

the length of a piezo actuator[36] to which one of the cavity mirrors is attached.

The home-built cavity has a finesse of approximately 2000 at 780 nm. Following recommendations from deHond et al. [141], we opted for a plano-concave design with the curvature of one mirror of 500 mm[37]. To reduce the cavity linewidth, we decided for a longer cavity design, utilizing a 250 mm Invar spacer[38] machined in our institute's mechanical workshop[39]. The cavity is housed in a teflon tube, which is enclosed within an aluminum tube, and further surrounded by another teflon tube. This assembly is securely mounted on a breadboard. We decided not to place the cavity under vacuum, as anyway it is actively stabilized. Additionally, a home-built temperature control system is implemented to stabilize the temperature of the aluminum tube, although its performance is limited, likely due to the cavity large size.

Cavity lock performance

We measured the error signal (ES) slope to be approximately 9 mV/kHz, which should meet our requirements. With a noise floor of a few mV, the locking system is capable of responding to cavity length changes corresponding to less than 1 kHz. The lock's bandwidth, estimated by increasing the gain until the system starts oscillating, is around 13 kHz. While this may seem relatively low, it is expected due to the limited bandwidth of the piezo actuators we are using.

Similar to the MTS setup, we currently lack a means of directly assessing the long-term stability of the cavity lock. However, there are indications that the stability may not be as good as we had hoped. Notably, we observe a significant amount of residual amplitude modulation (RAM), likely stemming from a slight polarization mismatch in the EOM and etalon effects (either in the EOM or somewhere down the optical path). Although careful alignment can temporarily eliminate the RAM, it tends to reappear over time, necessitating periodic realignments. Such effects have been studied before [142, 143] and a particularly promising approach is to use a wedged EOM [144]. Additionally, relocating the EOM before the optical fiber could improve the spatial uniformity of the imprinted sidebands. For more details on RAM, please refer to the discussion in sec. 3.3.1.

In addition to RAM concerns, we also face challenges arising from environmental factors. Fluctuations in ambient temperature can exceed the compensation range of

---

[36] Physik Instrumente Round PICMA PD150.31

[37] 0.5 inch fused-silica mirrors from Layertec 122294 (plane) and 122293 (concave) with reflectance of 99.8(1) % at 780 nm and 958 to 970 nm

[38] City Special Metals Invar 36

[39] The cavity finesse depends only on the intra-cavity losses, which for a typical cavity is given by $\mathcal{F} \approx 2\pi/(1 - r_1 r_2)$, where r_1 and r_2 are reflectances of the mirrors, which were assumed to be close to 1. In the same time, finesse is defined as a ratio between the cavity free spectral range, FSR and its linewidth, $\delta\nu$, $\mathcal{F} = \mathrm{FSR}/\delta\nu$. As the cavity FSR is inversely proportional to its length L, $\mathrm{FSR} = c/2L$, it straightforward to see that increasing the cavity length decreases effectively its linewidth.

the piezo driver. Furthermore, abrupt pressure changes resulting from activities like opening doors can impact the stability of the cavity. To mitigate these issues, one possible solution is to place the cavity under vacuum conditions.

3.3.3 Coupling laser lock

As previously mentioned, the optical cavity plays a role of a frequency reference for the 960 nm seed light of the coupling laser. To stabilize its frequency, we employ the Pound-Drever-Hall (PDH) method in combination with the offset sideband locking technique [145]. This approach is necessary because the desired wavelength (given by the atomic resonance) may be far from the cavity resonance.

To address this, we use a wideband fiber electro-optic modulator (fEOM)[40] to generate sidebands, with one of them resonant with the cavity. This resonant sideband then serves as the carrier frequency for the PDH method, what is schematically shown in fig. 3.7(bottom right). To drive the fEOM we use an amplified[41] signal from a small USB RF generator[42].

The light is directed towards the same setup, where a collimated beam with a diameter of 1 mm is directed towards the opposite side of the cavity. To ensure mode matching, we employ a lens with a shorter focal length compared to the 780 nm case, as the concave mirror acts as a diverging lens. Prior to entering the cavity, the light passes through a dichroic mirror, which reflects the transmitted 780 nm wavelength. Unlike the 780 nm light, there is no need for an EOM for the 960 nm light, as it is already frequency modulated within the laser itself, serving the purpose of locking the second harmonic generation (SHG) cavity. The modulation frequencies of the 780 nm and the 960 nm lights, 12.5 MHz and 20 MHz, respectively, are purposely different to avoid any cross-talk between the locking systems.

This locking mechanism not only stabilizes the absolute frequency of the laser but also narrows its linewidth, thanks to the relatively large bandwidth of the lock, which is approximately 1 MHz. This linewidth reduction is essential in our system, as phase noise can adversely affect overall efficiency, as discussed in sec. 5.2. We estimated the 960 nm laser linewidth to be around 30 kHz based on the RMS of the error signal (ES) (the laser is locked) and the measured ES slope, 2.8 mV/kHz. This is a significant accomplishment, but we are aiming to further improve. Our target is to achieve a linewidth of around 10 kHz, which would be the optimal outcome for our system.

However, there are some slow drifts caused by residual amplitude modulation (RAM). One source of RAM arises from modulating the laser diode current to achieve the necessary frequency modulation for locking the second-harmonic generation (SHG) cavity. While this modulation also introduces some amplitude modulation, we believe that this RAM component remains constant over time and should not

---

[40] iXblue NIR-MPX950-LN-10-00-P-P-FA-FA

[41] Mini-Circuits ZFL-1000VH+

[42] Windfreak SynthUSBII

pose significant issues. Subsequent laser models have addressed this concern by incorporating an EOM to directly modulate the seed light, thereby reducing this particular RAM source.

Additionally, there is some RAM originating from the fiber EOM, which we employ not only for the offset sideband generation but also to amplify the PDH sidebands. This is necessary because the current modulation in the laser is relatively small. Fortunately, this issue has been the subject of previous studies [146–148], and we are optimistic that we will find a suitable solution to mitigate this RAM problem.

3.3.4 Summary

In summary, our locking system stands as a robust solution that meets our needs. The performance of the MTS lock for the 780 nm laser appears very good, although it's challenging to precisely gauge its performance due to a lack of comparably stable frequency reference. However, the absence of observable error signal offset and, hence, offset drifts suggests that the system is performing well.

The primary limitation of the setup appears to be the RAM in the PDH locks of the cavity and the 960 nm laser. While we haven't continuously monitored the resulting offsets over extended durations, occasional checks indicate that drifts likely remain within the range of 100 kHz (based on measured error signal slopes). With known solutions available and some adjustments, we are hopeful to improve on this issue significantly.

It should be mentioned, however, that during an experiment conducted while preparing this thesis, we started periodically monitoring the photon generation efficiency's dependence on the coupling AOM frequency. This indirectly provides insights into the combined frequency drift of the 780 nm and 479 nm light sources. Notably, it is necessary to adjust the coupling light frequency by up to 2 MHz to obtain optimal generation efficiency. This suggests much larger drifts than above estimations, however, it's possible that factors beyond laser frequencies contribute to these drifts. To validate this observation, we think of using an ultra-stable cavity already used by another experiment in our group to monitor coupling light frequency drifts (as the cavity has sufficient reflectance only for this wavelength). With this method, we expect to definitively benchmark the locking setup's performance.

Another problem is the environmental impact on the cavity length, which sometimes drives away the piezo controller out of its range. We hope to solve this issue by putting the cavity under vacuum.

Beyond its good performance, our locking setup is cost-effective and scalable. While we haven't calculated exactly the setup cost, a rough estimate places the expenses at less than 7000 euros, significantly lower than, for instance, an ultra-stable cavity (excluding additional elements such as EOMs and external optics and electronics). Furthermore, if the need arises to lock another laser, the design can be duplicated using mirrors with different coatings. In principle, this locking approach can be expanded to multiple wavelengths without substantial expenses.

3.4 Experimental control

We utilize an FPGA-based device from Signadyne (now Keysight) to control our experiment and capture time-tag information from detectors. Our setup includes two analog cards with a total of 8 channels, which we mostly use to control various AOMs. Each channel operates independently and incorporates an arbitrary waveform generator (AWG) functionality. Additionally, we have a digital card with 32 output channels for simple on/off control, as well as a time-to-digital converter (TDC) featuring 4 input channels and a resolution of 320 ps. As the TDC is integrated with other cards, it is possible to perform operations conditioned on presence or lack of a photon detection. All of these components are housed within a National Instruments PXI rack.

Despite the versatility of this device, we have encountered some dissatisfaction with its performance. It exhibits occasional bugs, and unfortunately, Keysight, the company that acquired the original manufacturer, provides minimal support. Consequently, we are actively exploring alternative solutions for testing and potential future acquisitions.

Parameter	Typical value
Ensemble size	$(15\,\mu\text{m})^3$ (FWHM)
Optical depth (OD)	11 (up to 20)
# atoms	1700
Probe waist	6.5 µm
Coupling beam waist	11 µm
Coupling Rabi frequency ($\Omega_c/2\pi$)	8.5 MHz (to $90S_{1/2}$)
Excited state decay rate ($\Gamma/2\pi$)	6.067 MHz [149]
Rydberg state decoherence rate ($\gamma_r/2\pi$)	0.4 MHz

Table 3.1: Summary of typical parameters in our experiments.

Chapter 4

Single photon detection

Photon detection plays a critical role in our experiments, as it allows us to analyze the photons emitted by our system. To ensure accurate interpretation of the results, it is important to understand how photon detection works and its impact on our measurements. In this chapter, I discuss some practical aspects of single-photon detection from an experimental perspective. It does not aim to provide an exhaustive review but rather highlights experimental challenges and considerations encountered during my PhD. By addressing these challenges and incorporating proper modeling techniques, we aim to factor out the effects of photon detection on our experimental findings, in particular, the autocorrelation measurements.

4.1 Autocorrelation $g^{(2)}$

The autocorrelation function, denoted as $g^{(2)}$, is a commonly used metric for assessing the quality of single-photon emission. One of the key advantages of $g^{(2)}$ is its invariance under linear losses, making it a robust tool for evaluating the performance of single-photon sources. By looking at the shape and magnitude of the autocorrelation function, one can gain information about the photon statistics and temporal properties of the emitted light.

For a polarized parallel light beam (which is a typical situation in our experiments) propagating along z direction, $g^{(2)}$ can be expressed as [150, sec. 4.12]

$$g^{(2)}(z,\tau) = \frac{\left\langle \hat{E}^{-}(z,t)\hat{E}^{-}(z,t+\tau)\hat{E}^{+}(z,t+\tau)\hat{E}^{+}(z,t) \right\rangle}{\left\langle \hat{E}^{-}(z,t)\hat{E}^{+}(z,t) \right\rangle \left\langle \hat{E}^{-}(z,t+\tau)\hat{E}^{+}(z,t+\tau) \right\rangle}, \tag{4.1}$$

where $\hat{E}^{+}(z,t) = \sum_i u_i(z,t)\hat{a}_i$ and $\hat{E}^{-}(z,t) = \sum_i u_i^{*}(z,t)\hat{a}_i^{\dagger}$ are electric field operators, $u_i(z,t)$ are spatio-temporal modes describing the photon wave packet, $a_i^{\dagger}$ are the corresponding photon creation operators and $\langle\ \rangle$ denotes the quantum mechanical expectation value.

For a single-mode light, the above expression simplifies to [150, sec. 5.1][1]

$$g^{(2)}(0) = \frac{\langle a^\dagger a^\dagger a a\rangle}{\langle a^\dagger a\rangle^2}. \tag{4.2}$$

In particular, for a state with a Fock distribution p_k, where k corresponds to the photon number, it can be written as:

$$g^{(2)}(0) = \frac{\sum_{k=0}^{\infty} k(k-1)p_k}{\left(\sum_{k=0}^{\infty} k p_k\right)^2}. \tag{4.3}$$

From this, it can be easily seen that for a Fock state of n photons, $g^{(2)}(0) = 1 - \frac{1}{n}$. Thus, for a perfect single photon, $g^{(2)}(0) = 0$. For a photon source, where $p_1 \gg p_2 \gg p_{k>2}$ it becomes

$$g^{(2)}(0) \approx \frac{2\,p_2}{p_1^2}. \tag{4.4}$$

In such a case $g^{(2)}(0)$ is a direct measure of the multi-photon probability for a single-photon source.

In the case of coherent light, such as laser light, where Poissonian statistics apply, the value of $g^{(2)}(0)$ is equal to 1. Notably, any light with $g^{(2)}(0)$ less than 1 defies explanation by classical theory, signifying a distinct quantum phenomenon. This implies *sub-Poissonian* statistics, characterized by $\Delta k < \sqrt{\overline{k}}$, with Δk and $\overline{k}$ denoting the standard deviation and expectation value of p_k, respectively [150, p. 250].

Closely associated is the concept of *antibunching*, where the occurrence frequency of closely spaced photons is lower compared to photons with larger spacings, implying $g^{(2)}(0) < g^{(2)}(\tau)$. Both these situations are purely quantum in nature [151, ch. 6.5]. It's important to note that sub-Poissonian statistics do not necessarily imply antibunching [152], although non-classical light often exhibits both photon antibunching and sub-Poissonian photon statistics simultaneously.

4.1.1 Hanbury-Brown and Twiss

The Hanbury-Brown and Twiss (HBT) setup is a common configuration used to measure $g^{(2)}(\tau)$. It consists of a beam-splitter and two single-photon detectors (SPDs) connected to a time-tagging device, as shown in fig. 4.1(left). The use of two detectors helps overcome the limitations imposed by the dead time of the SPDs.

In our experiments, we measure the number of coincidences of detections in both detectors for different relative delays between the detections, denoted as $N_{1,2}(\tau)$. Let

---

[1] One may observe that, based on the assumption that light is emitted in a single mode, $g^{(2)}(\tau) = g^{(2)}(0)$ for any τ. However, this is an artifact of the idealized assumption. In reality, light cannot be perfectly single-mode; in particular, its frequency modes' distribution has a finite width and thus a finite coherence time. When accounting for these factors, one expects to recover $g^{(2)}(\tau) = 1$ for large τ.

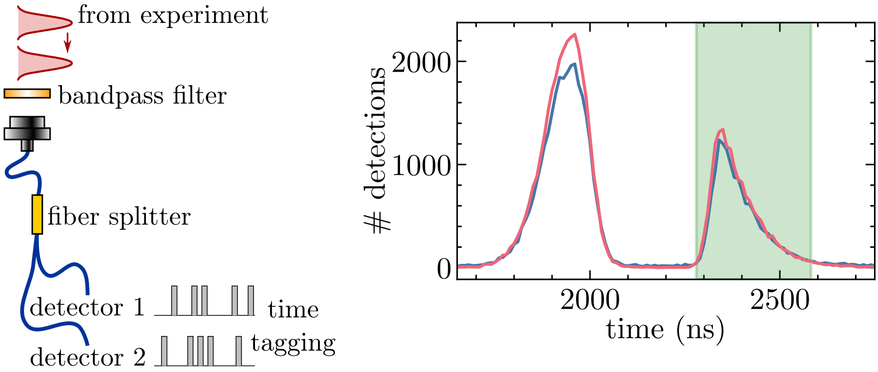

Figure 4.1: (left) The Hanbury-Brown and Twiss (HBT) setup used in our experiment. The bandpass filter blocks scattered coupling light and prevents backflash detections (if we use SPADs). The time tagging device is discussed in sec. 3.4. (right) Typical histograms of photon detections. The first peak is the leakage of the excitation pulse, the second is the retrieved single photon pulse. Two different curves correspond to the two detectors. The shaded area is the detection window in which we look for coincidences. The histograms start with a trail trigger sent by the experimental control at the beginning of each trial. The bin size is 10 ns.

N be the total number of experimental trials and $c_{1,2}(\tau) = N_{1,2}(\tau)/N$ be the mean detected coincidence number per trial. As typically $c_{1,2}(\tau) \ll 1$, it can be also seen as the probability of detecting such an event. It can be shown that the normalized probability of these events is equal to $g^{(2)}(\tau)$ given in eq. 4.1 [150, sec. 5.9]:

$$g^{(2)}(\tau) = \frac{\langle \hat{n}_1 \hat{n}_2 \rangle}{\langle \hat{n}_1 \rangle \langle \hat{n}_2 \rangle} = \frac{c_{1,2}(\tau)}{p_1 p_2} = \frac{N_{1,2}(\tau) N}{N_1 N_2}, \tag{4.5}$$

where $\hat{n}_{1(2)}$ is the number operator acting on the mode going to detector 1(2), $\langle\,\rangle$ is the expectation value, $p_{1(2)} = N_{1(2)}/N$ is the mean detected photon number and $N_{1(2)}$ is the total number of detections in detector 1(2). An example curve of $g^{(2)}(\tau)$ can be seen in fig. 4.2(right). An alternative approach to measuring $g^{(2)}(\tau)$ is by solely measuring $N_{1,2}(\tau)$ and assuming that for large delays τ, there is no correlation between the detections, resulting in $g^{(2)}(\tau) = 1$.

It is important to note that the above analysis assumes that the expectation values from eq. 4.1 depend only on the relative delay between the detections, denoted as τ, and not the absolute time t, implying that the fields are stationary. While this assumption is often valid, it is not always the case.

During the measurements in the experiment described in ch. 7, we discovered that our setup required several tens of milliseconds to "warm up" during each trapping cycle before reaching a steady-state efficiency[2]. This introduced periodicity in the

---

[2] We are still unsure about the mechanism responsible for this effect, however, it seems to be of technical rather than physical origin.

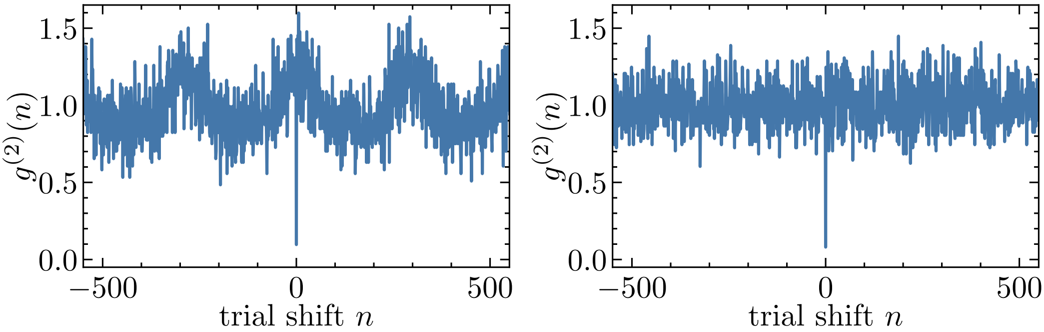

Figure 4.2: Autocorrelation $g^{(2)}$ as a function of trial shift for two sets of data: (left) where the single photon detection probability was (unexpectedly) varying during the interrogation time and (right) where only a part of the data with a constant probability was used. As we typically look for coincidences in a window that includes whole single-photon pulses (see fig. 4.1(right)), the relative delay between the detections τ is given in trial number difference n, i.e. $\tau = n\, t_{\text{trial}}$, where t_{trial} is the trail length and typically $t_{\text{trial}} = 5\,\mu\text{s}$.

photon detection probabilities. Initially unaware of this effect, we assumed the probabilities to be constant over time, resulting in periodic changes in the extracted $g^{(2)}(\tau)$, as shown in fig. 4.2(left). However, by excluding the "warm-up" periods from the data, we were able to recover the expected behavior of $g^{(2)}(\tau)$, as depicted in fig. 4.2(right).

4.1.2 Effect of noise on $g^{(2)}$

As we mentioned before, $g^{(2)}$ is independent of linear losses, however, it can be affected by noise. Especially when one tries to measure values of $g^{(2)}(0)$ close to zero, any noise is detrimental. As discussed later in sec. 4.3, most of the noise source present in our system are uncorrelated with the photon detections. We can easily evaluate the effect of uncorrelated noise detections upon $g^{(2)}$.

If we assume that the probability of detecting any type of 3-detection coincidence is negligible, the noise alters the probabilities for detection and coincidences as follows:

$$\tilde{c}_{1,2} = c_{1,2} + p_1 p_{n,2} + p_2 p_{n,1} + p_{n,1} p_{n,2} \tag{4.6}$$

$$\tilde{p}_{1(2)} = p_{1(2)} + p_{n,1(2)}. \tag{4.7}$$

Here, $p_{n,1(2)}$ is the noise probability for detector 1(2). The autocorrelation is therefore:

$$\tilde{g}^{(2)}(0) = \frac{\tilde{c}_{1,2}}{\tilde{p}_1 \tilde{p}_2} = \frac{p_{12} + p_1 p_{n,2} + p_2 p_{n,1} + p_{n,1} p_{n,2}}{p_1 p_2 + p_{n,1} p_2 + p_{n,2} p_1 + p_{n,1} p_{n,2}}, \tag{4.8}$$

which can be rewritten in terms of SNRs as

$$\tilde{g}^{(2)}(0) = \frac{g^{(2)}(0) + 1/s_1 + 1/s_2 + 1/(s_1 s_2)}{1 + 1/s_1 + 1/s_2 + 1/(s_1 s_2)}, \tag{4.9}$$

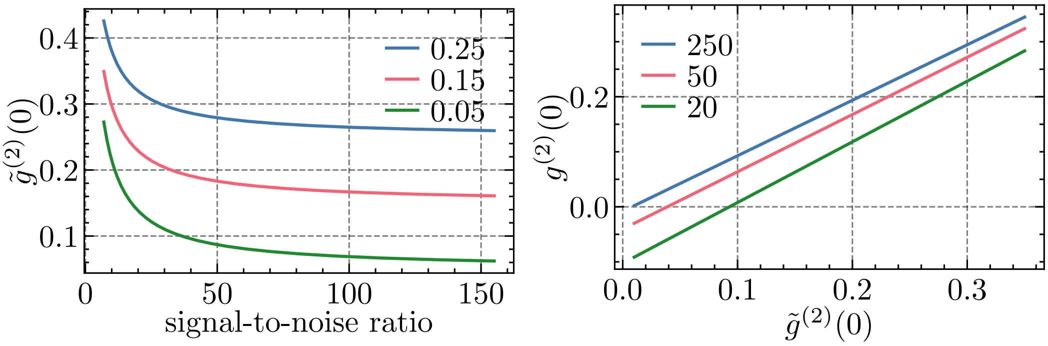

Figure 4.3: (left) The influence of noise on $g^{(2)}(0)$ for various "ideal" $g^{(2)}(0)$ values. Low SNR increases the measured $\tilde{g}^{(2)}(0)$ and only for large SNR the effect of noise becomes negligible. The effect is more pronounced for smaller $g^{(2)}(0)$. (right) Noise-corrected $g^{(2)}(0)$ as a function of the detected $\tilde{g}^{(2)}(0)$ for different values of SNR. Negative values of the noise-corrected $g^{(2)}(0)$ for smaller values of SNR correspond to the values of the detected $\tilde{g}^{(2)}(0)$ that cannot be observed with such a noise strength.

where $s_{1(2)} = p_{1(2)}/p_{n,1(2)}$ is the SNR for detector 1(2).

Assuming that SNRs are the same for both detectors, this expression finally simplifies to

$$\tilde{g}^{(2)}(0) = \frac{g^{(2)}(0) + 2/s + 1/s^2}{1 + 2/s + 1/s^2}. \tag{4.10}$$

In fig. 4.3(left) one can see the effect of finite SNR on $g^{(2)}(0)$.

4.1.3 Correcting $g^{(2)}$ for noise

If one assumes that the noise affecting $g^{(2)}$ is uncorrelated with the photon detections, which is our usual assumption, correcting for the noise means simply solving eq. 4.9 for $g^{(2)}(0)$. This gives

$$g^{(2)}(0) = \tilde{g}^{(2)}(0) - \left(1 - \tilde{g}^{(2)}(0)\right)\left(\frac{1}{s_1} + \frac{1}{s_2} + \frac{1}{s_1 s_2}\right). \tag{4.11}$$

The effect of noise correction is shown in fig. 4.3(right).

4.2 Single-photon detectors

In our group, we use two distinct types of single-photon detectors (SPDs) for visible light: semiconductor single-photon avalanche diodes (SPADs)[3] and superconducting nanowire single-photon detectors (SNSPDs)[4]. These detectors operate on vastly different principles, resulting in distinct noise characteristics for each type.

---

[3] Laser Components COUNT-10C-FC and Excelitas SPCM-AQRH-14-FC

[4] ID Quantique ID281

SPADs, similar to photodiodes, operate based on the principle of the internal photoelectric effect. When a low reverse bias voltage is applied to a photodiode, the leakage current changes linearly with the absorption of photons, resulting in the liberation of current carriers (electrons and/or holes). However, in the case of a SPAD, the reverse bias voltage is significantly higher, allowing a single carrier to trigger a self-sustaining avalanche of carriers, generating a detectable current [153, sec. 2]. SPADs offer the advantages of affordability (typically a few thousand euros) and compact device size. The typical dead time[5] ranges from 20 ns to 50 ns, and the detection efficiency at a wavelength of 780 nm can exceed 60 %.

On the other hand, SNSPDs consist of a meander structure made from superconducting wire, typically around 10 nm thick and 200 nm wide. These nanoscopic superconducting wires, when biased near the critical current (at which the superconductivity breaks down), experience local destruction of the superconducting state within picosecond timescales upon absorption of a photon. While initially only a tiny section of the wire becomes resistive, the subsequent Joule heating causes the resistive region to expand, resulting in an effective resistance in the kΩ range [154, sec. 6.2]. SNSPDs are typically bulky due to the requirement of placing them in a cryostat and are more expensive, with costs on the order of 100,000 euros. However, they offer the highest achievable detection efficiencies, exceeding 90 %. Additionally, SNSPDs might exhibit short dead times of less than 10 ns.

4.3 Single-photon detection noise

Our SPDs are sensitive to various types of noise. These noises can originate from the detection process itself, such as afterpulsing or dark counts, or they can arise from the experimental setup, such as scattered coupling light. While certain types of noise can be effectively filtered out, others pose significant challenges for removal and have to be accounted for in the post-processing.

4.3.1 Dark counts

The dark count rate refers to the average number of counts recorded by a detector per second when no light is present.

In the case of SPADs, dark counts arise from thermally generated carriers within the SPAD junction. These dark counts exhibit Poissonian statistics and serve as the internal noise source of the detector [154, sec. 4.4.2]. While they are typically constant in time, the dark count rate may increase temporarily after strong pulses

---

[5] Dead time refers to the duration after a detection event during which the system cannot produce an output signal in response to additional photons. The significance of dead time varies depending on the pulses being detected. In our experiment, where typical pulse durations are around 150 ns, the dead time poses a significant limitation on our ability to accurately determine the photon number of multi-photon pulses.

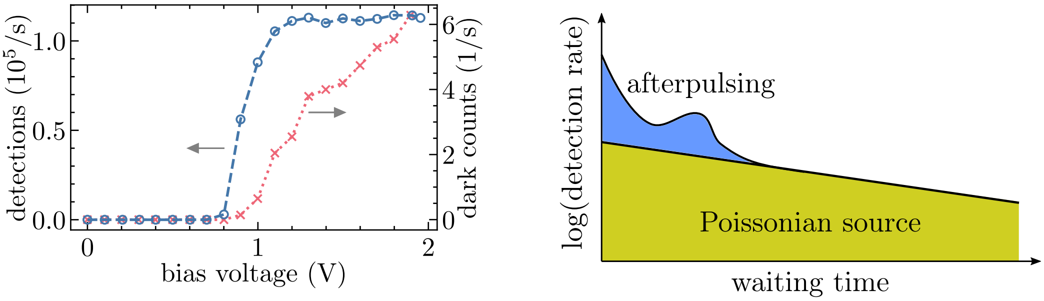

Figure 4.4: (left) Detection rate and dark count rate observed at the SNSPD as a function of bias voltage. One can see that the detection efficiency saturates before reaching the critical current (which corresponds to around 2.1 V of the bias voltage) allowing us to work with low dark count rate. (right) Schematic histogram of SPAD afterpulse detections appearing on top of the photon detections from a coherent light source as a function of waiting time between two consecutive detections. It can be easily shown that the probability of detecting a click for a given waiting time follows an exponential decay [156]. Therefore, by fitting an exponential function (black solid line) to the part of the histogram for large waiting times, one can easily identify afterpulse detections (blue part of the histogram). The typical waiting time after which no afterpulse should be detected depends on the detector and varies from 100 to 1000 ns.

that heat up the detector. For silicon SPADs, typical dark count rates fall within the range of 10 to 100 per second.

In the case of SNSPDs, it is helpful to consider dark counts as a combination of two components: intrinsic and extrinsic dark counts. Extrinsic dark counts primarily result from factors external to the nanowire, such as black-body radiation or electronic noise. On the other hand, the origin of intrinsic dark counts, remains largely unknown [155].

The dark count rate in SNSPDs is dependent on the applied bias current and can be as low as 1/s[6]. However, achieving such a low rate often comes at the expense of lower detection efficiency. This trade-off is particularly pronounced for telecom SNSPDs, where achieving maximum detection efficiency is accompanied by tens or more dark count clicks per second. In our specific case, at 780 nm, we are able to operate at the maximum detection efficiency with less than 6 dark counts per second, as illustrated in fig. 4.4(left).

Similarly to SPADs, dark counts in SNSPDs can typically be modeled using Poissonian statistics. It should be mentioned that at large bias currents, deviations from Poissonian distribution have been observed [155]. However, in our case, we do not consider this to be a significant issue since the absolute number of dark counts is very low. In particular, the count rate due to stray light collected by the fibers can be several times larger than the dark count rate.

---

[6] Similar phenomenon is observed in SPADs, but typically commercial SPADs come with preadjusted bias voltage.

4.3.2 Afterpulsing

The afterpulse probability refers to the additional probability of a detector producing a dark count after a preceding detection event. This probability can vary depending on the overall count rate, and differs from one detector to another in terms strength and for how long the dark count probability is elevated.

In the case of SPADs, afterpulsing is a well-understood phenomenon [154, sec. 4.4.3] and its chance of occurring is typically, for visible light detectors, below 0.5 %. For SNSPDs, reports vary, with some indicating no afterpulsing [157] or afterpulsing attributed to electronics rather than the detector itself [158]. However, recent studies have reported afterpulsing in SNSPDs that cannot be attributed to external factors [159].

The afterpulse probability can be measured by analyzing the histogram of time differences (waiting times) between consecutive clicks [156]. By fitting an exponential function to the long waiting times, where afterpulsing is not expected, one can extract the additional probability of detecting a click immediately after a detection event, as shown in fig. 4.4(right). However, caution must be exercised as afterpulsing events can be mixed with clicks corresponding to photons detected in the "twilight" zone, which is the final part of the detector's dead time when its efficiency is recovering. These photons can be detected, but their timing is often incorrect, leading to an aggregation of counts right after the dead time. To mitigate this, one can scan the rate of incoming photons and examine the asymptotic behavior at zero rate [154, sec. 8.4.1].

Although afterpulses are correlated with photon detections, their impact on $g^{(2)}(0)$ measurements should be minimal, see sec. 4.1.2. This is because the detection coincidence and afterpulsing are independent events, thus the probability of observing an afterpulse for a coincidence click is the same as for a regular photon detection.

4.3.3 Backflash

Backflash refers to the broad-spectrum emission emitted by a detector following a detection event. It has been observed in SPADs and studied as a potential vulnerability in quantum key distribution protocols [160, 161]. The backflash probability is often not provided in the detector datasheets. However, in a study by Pinheiro et al. [161], they reported that a similar detector to ours had a backflash probability of not less than 6.5 %. As for SNSPDs, I haven't come across any reports of backflash, and it seems unlikely to occur since there are no relaxation processes involved in the detection or reset of these detectors.

Backflash poses a particular concern in autocorrelation measurements, as it can cause cross-talk between two detectors. This occurs when light emitted by one detector is reflected by an optical element and subsequently detected by another detector. Since such events are strongly correlated, backflash can significantly impact $g^{(2)}(0)$ measurements.

We learned about the effect of backflash the hard way while conducting the experiment described in ch. 6. We noticed that our measured values of $g^{(2)}(0)$ were much higher than expected. To confirm our suspicion that backflash was responsible for this discrepancy, we conducted a simple test, as illustrated in fig. 4.5(left). We connected a SPAD under test and an SNSPD (as a reference) to two output taps of a fiber splitter. Additionally, we connected another SNSPD to one of the input taps to monitor reflections. By cross-correlating the detections of the SPAD and SNSPDs, we were able to identify various effects, including reflections from FC/PC connectors, two-photon components of the input pulses, and most importantly, backflash (as shown in fig. 4.5(right)). The element responsible for reflecting the backflash back to the detectors was a filter cavity used in the memory setup, designed to reflect all frequencies except the stored photon frequency. Moreover, when we introduced a narrow bandpass filter after the filter cavity, the backflash peak disappeared in the cross-correlation histogram, which was expected since backflash is typically a broad-spectrum emission. One should also notice, that the probability of detecting a backflash click scales linearly with the photon detection probability, while the coincidence probability scales quadratically. It means that backflash can be particularly problematic when the photon detection probability is very low.

The key takeaway from our experience is that when using SPADs for autocorrelation measurements, it is always advisable to include a band-pass filter immediately before the detector. This helps mitigate the impact of backflash on the measurement results.

4.3.4 Other noise

In addition to the discussed noises originating from the detection process, our system also experiences noise caused by scattering from different laser beams. During the relevant time window, when the photon is expected, only the coupling beam is active, and it is the sole source of noise. The majority of this noise arises from the scattering of 480 nm light on the science cell, which we effectively filter out using a band-pass filter[7]. However, there is some additional noise that cannot be eliminated with the band-pass filter. We attribute this noise to fluorescence emitted by the Rubidium atoms deposited on the walls of the science cell or the science cell glass itself. Part of this fluorescence occurs at a wavelength close to that of the photons (780 nm) and contributing approximately 40 additional detections per second. We observe that the main factor reducing this number is the bandwidth of the filter, suggesting that the fluorescence is wideband. Since these detections are expected to be uncorrelated with the photon detections, we treat them as additional dark counts and correct them using the same method described in sec. 4.1.3.

---

[7] Thorlabs FBH780-10

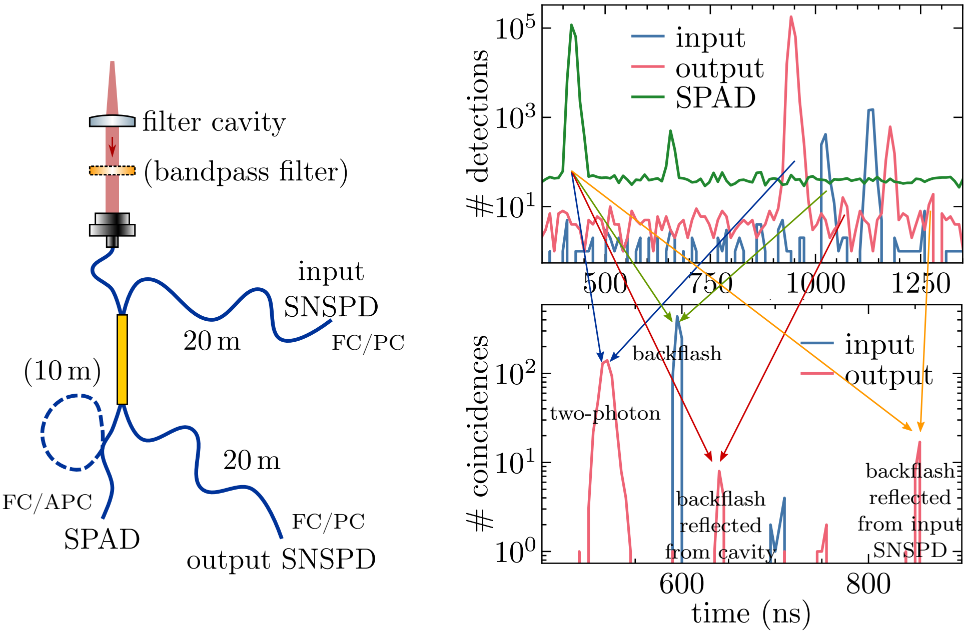

Figure 4.5: (left) Setup used to characterize backflash emitted by our SPADs. Input SNSPD allows for a direct detection of the backflash emitted by the SPAD. Output SNSPD monitors the backflash that was reflected by the filter cavity (or any other optical element). Adding the extra 10 m delay line allows us to identify the origin of different spurious (backflash and reflections) peaks in the histograms. Fibers going to SNSPDs are FC/PC-terminated what causes undesired reflections. (right) Detection histograms of SPAD, input SNSPD and output SNSPD (top) and histogram of coincidence between SPAD and input/output SNSPD detections (bottom). The two highest peaks in the top histogram correspond to the original weak 40 ns pulses detected by the SPAD and the output SNSPD. The delay of output SNSPD histogram with respect to the SPAD histogram comes from the different fiber length, but also additional delay of around 400 ns due to extra cables and electronics. One should notice that peaks identified as the backflash detections are of almost identical height in both histograms, highlighting that these events are highly correlated with the SPAD detections.

Chapter 5

Excitations in Rydberg ensembles

In this chapter, we look into the practical aspects of generating Rydberg excitations and their subsequent retrieval as single photons. I explain the processes involved in creating these excitations, and later discuss challenges posed by various noise sources that limit their generation and retrieval efficiencies.

5.1 Single-photon generation

We use the properties of Rydberg atoms and atomic ensembles to reliably and efficiently generate single photons. In our work, we employ two distinct approaches: off-resonant (OR) two-photon excitation and electromagnetically-induced transparency (EIT). Both of them create Rydberg spin waves within the atomic ensemble, which can be subsequently converted into single photons. In this section, we will explain these techniques and explore their potential for efficient and controlled single-photon generation.

5.1.1 Off-resonant single-photon generation

One common approach to single-photon generation is to use a two-photon off-resonant excitation (OR excitation) to initially excite the atoms to the Rydberg state $|r\rangle = \left|nS_{1/2}\right\rangle$, as illustrated in fig. 5.1. Following this, the Rydberg excitation is transferred using a π-pulse to a short-lived state $|e\rangle = \left|5P_{3/2}, F' = 3\right\rangle$ from which it decays, emitting a photon. The Rydberg blockade mechanism ensures that only one excitation is present in the Rydberg state, resulting in the emission of a single photon. Additionally, due to the nature of the excitation as a spin wave, the emitted photon is confined to a well-defined mode.

To achieve this, the detuning from the excited state Δ_p is set to be large, where $\Delta_p \gg \Gamma$. Under this condition, the three-level system can be approximated as a two-level system comprising only $|g\rangle$ and $|r\rangle$, connected through a field with a two-photon Rabi frequency [102, sec. 6.1]

$$\Omega_R = \frac{\Omega_p \Omega_c}{2\Delta_p}. \tag{5.1}$$

Both the probe and control fields, being far-detuned from their respective transitions, induce AC Stark shifts on $|g\rangle$ and $|r\rangle$, resulting in a shift of the two-photon resonance by

$$\delta_R = \frac{\Omega_c^2 - \Omega_p^2}{4\Delta_p}. \tag{5.2}$$

For our experimental parameters, δ_R is around 500 kHz. It should be mentioned that during the excitation process, there is a residual population in the $|e\rangle$ state. This population introduces decoherence, which is discussed along with other decoherence mechanisms in sec. 5.2. Typically, one refers to this approximation as *adiabatic elimination*.

In our experimental setup, we typically use a detuning of $\Delta_p/2\pi = 40\,\mathrm{MHz}$. This choice of detuning ensures that significant population in the $|e\rangle$ state is prevented, while also maintaining a sufficiently large two-photon Rabi frequency. This allows us to efficiently excite the atoms with pulses typically shorter than 1 µs.

To achieve efficient population transfer, different techniques can be employed. One commonly known method is the Rabi π-pulse, where the Rabi oscillation between the two states is stopped once the population is fully transferred to the Rydberg state. However, this approach is susceptible to various noise sources, such as amplitude and frequency fluctuations of the driving field [162], as well as atomic number fluctuations in the case of Rydberg ensembles [163].

A more robust alternative is the adiabatic rapid passage (ARP), where the frequency of the transferring pulse is adiabatically swept. By properly sweeping the frequency, the instantaneous eigenstates of the system are changed in a continuous manner, effectively transforming the system ground state into the excited state and, therefore, achieving population transfer. In the context of Rydberg ensembles, ARP has been studied theoretically [163, 164] and successfully demonstrated [165]. However, it was also suggested theoretically that ARP might not be well suited for performing operations where the spin wave phase needs to be well controlled, like in logic gates, as the accumulated phase depends strongly on the atoms' number [164]. Another known alternative is the stimulated Raman adiabatic passage technique (STIRAP). However, a theoretical study showed that in the resonant case it destroys the interatomic coherence and dephases the single Rydberg excitation, making it useless for our purposes [166, sec. I].

In our case, not only is the efficiency of population transfer important, but also the autocorrelation $g^{(2)}(0)$ of the retrieved photons. In strongly blockaded ensembles, where only one excitation can exist, the $g^{(2)}(0)$ value of the photons is very low [60, 62, 64, 167]. However, in our ensemble, which is slightly larger than the blockade radius, multiple Rydberg excitations can potentially exist. These coexisting excitations, however, dephase due to mutual interactions, effectively suppressing multiphoton emission [57, 79, 168, 169]. Therefore, the photons' $g^{(2)}(0)$ value depends on the number of created excitations and can be tuned by changing the population transfer efficiency (i.e. Rabi angle) [79].

To optimize the generation process, a characterization curve is typically obtained, as shown in fig. 5.1. The goal is to find a point where the $g^{(2)}(0)$ value is low while maintaining a good generation probability. As the number of excitations created in the ensemble has to be tuned, we use the typical Rabi cycle method to excite the atoms.

Finally, let's discuss the concept of the blockade radius in this context. The blockade radius is determined by the primary broadening mechanism in the excitation process [83, fig. 13], which can arise from factors such as the laser linewidth, collectively enhanced Rabi frequency, discussed in sec. 2.2.2 (resulting in power broadening[1]) or transition linewidth[2]. The blockade radius can be expressed as:

$$r_b = \sqrt[6]{\frac{C_6}{\hbar\,\delta\omega}}, \tag{5.3}$$

where $\delta\omega$ represents the frequency width of the dominant broadening mechanism. In our specific case, since we use pulses that are shorter than a full π-pulse, the dominant broadening mechanism is associated with the pulse spectrum, which can be obtained through a Fourier transform of the pulse wave shape. For typical experimental parameters with $n = 90$ and the pulse duration of 250 ns, the blockade radius is $r_b = 14\,\mu\mathrm{m}$.

5.1.2 EIT single-photon generation

Alternatively, one could use EIT for single-photon generation.

In this approach, one sends a weak coherent pulse under rEIT conditions, where the first photon is transmitted while subsequent photons are scattered due to dipole interactions (as explained in sec. 2.2.5). However, for this protocol to work, the pulse duration must be shorter than the blockade time, $\tau_b = r_b/v_g$, where v_g represents the group velocity[3]. Consequently, the pulses need to be broad in frequency, significantly

---

[1] Others report (in a different context) that in the case of population transfer with a π-pulse, one should not observe power broadening [170]. However, the Fourier limited pulse spectrum is anyway roughly equal to the Rabi frequency and, hence, results in the same blockade radius.

[2] Although in most cases, the homogenous transition linewidth is not the limiting factor, as it is typically narrow, on the order of a few kHz, the Doppler broadening might become significant, if the system is not very cold, like in our case. We estimate the Doppler broadening to be around 110 kHz.

[3] For a multi-photon pulse longer than τ_b, one can imagine a train of bins separated by approximately τ_b with each of them containing a photon. In fact, an attempt was made to realize such a source of trains of single photons, but unfortunately proved unsuccessful due to experimental limitations and the presence of not fully understood phenomena known as pollutants [61]. For a weak input pulse with on average less than 1 photon per τ_b, one also gets an irregular train of photons separated by τ_b or more. The explanation why the separation between the photons is not exactly τ_b is given in [171].

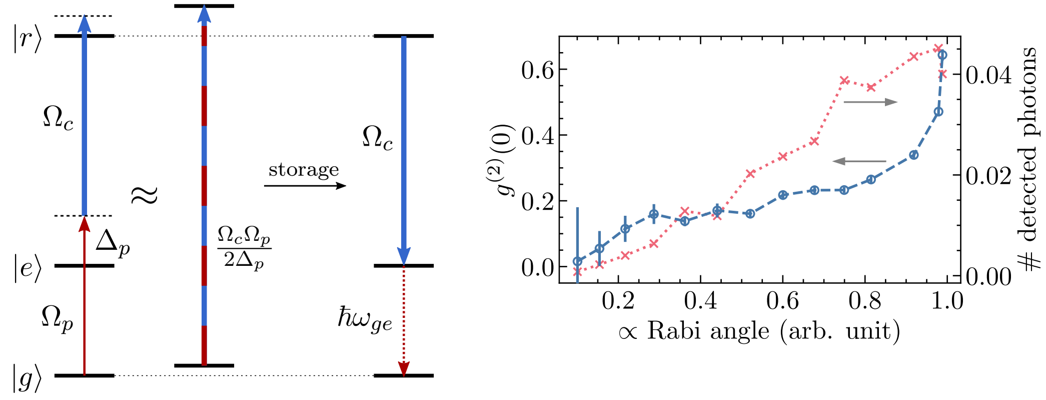

Figure 5.1: Off-resonant (OR) photon generation. (left) Schematic representation of the OR scheme. If the laser fields are far detuned from the excited state $|e\rangle$, one can approximate this system with a two-level system. However, atomic levels experience small AC Stark shifts, changing the resonance frequency (hence, the small shifts of $|g\rangle$ and $|r\rangle$). A Rydberg excitation is created with a two photon pulse with Rabi frequency $\Omega_R = \Omega_p\Omega_c/2\Delta_p$. After a programmable storage time, the excitation is transferred to the excited states from where it decays, emitting a photon. (right) A typical characterization curve of the OR photon generation at $n = 90$. Autocorrelation $g^{(2)}(0)$ and the mean detected photon number as a function of a quantity proportional to Rabi angle. One can see that there is a clear trade-off between larger number of generated photons and their quality.

broader than the EIT transparency width given by eq. 2.22, what results in losses. To implement this method successfully, two crucial requirements must be met: a high optical depth per blockade radius to lower the group velocity and assure that all the subsequent photons are scattered, denoted as $\mathrm{OD}_b = \mathrm{OD}\, r_b/L$ (where L is the ensemble length), and minimal decoherence in the Rydberg states to avoid suppression of the EIT transparency. Unfortunately, achieving these conditions is currently beyond our experimental capabilities.

Instead, our group employs an alternative approach. We send weak coherent pulses into the ensemble and, while these pulses travel under EIT conditions, we switch off the coupling beam, effectively storing the polaritons. After a programmed time, the coupling field is turned, leading to the retrieval of the stored polaritons as single photons. This technique eliminates the need for extremely short pulses, as the storage phase filters out undesirable portions of the pulse. The initial part of the pulse gets temporarily filtered, while the later part is scattered by the medium, as depicted in fig. 5.2(left).

Moreover, the storage phase enhances the nonlinearity experienced by the stored part of the pulse. This occurs for two reasons. Firstly, it arises due to the freeze of polariton propagation, a phenomenon previously observed in our group [80, fig. 3]. We believe that this effect can be understood through the following reasoning, which draws from [78]. When multiple Rydberg excitations are present, the dipole interaction disrupts the ideal EIT conditions, causing the propagating polaritons to partially occupy the excited state (unlike in the ideal EIT case, as discussed in sec. 2.2.3). As the propagation comes to a halt during storage, the decay from the excited state continues at the usual rate Γ, effectively reducing the amplitude of subsequently retrieved multiphoton states.

Secondly, multiple Rydberg excitations within the ensemble mutually dephase, leading to a suppression of multiphoton retrieval [172]. It's important to note that while a similar process exists in the OR generation technique, there are nuanced differences. In OR excitation, one general spin wave is generated, with higher order components undergoing self-dephasing. Conversely, in the EIT storage process, due to its sequential nature, one should envision multiple distinct spin waves (separated by the blockade radius) that mutually dephase. While the technical divergence from the OR technique is minimal – essentially involving setting the single-photon detuning to zero, $\Delta_p = 0$ – it's evident that these processes differ significantly in their underlying physics.

As in the case of OR excitation, an optimization curve is typically obtained, see fig. 5.2(right). Increasing the probe power leads to a greater number of polaritons in the ensemble, resulting in a higher generation probability but also a higher $g^{(2)}(0)$ value. The increase of $g^{(2)}(0)$ is discussed in more details and numerically simulated in ch. 7. The decrease in generation probability for very strong probes can be attributed to two effects.

Firstly, when a subsequent input photon scatters due to the blockade effect, the environment effectively projects the wave function of the initial polariton within a distance corresponding to the time interval between the two photon arrivals (of the first photon converted into a polariton and the second, scattered photon). This broadens the spectrum of the propagating polariton, causing it to no longer fit within the EIT transparency window and resulting in additional losses [171].

Secondly, there are what we call *pollutants*, which are Rydberg excitations that are not part of the polariton and cannot be efficiently retrieved as single photons, yet they still impose a blockade on the ensemble. These pollutants are photons scattered due to the dipole blockade or other processes, such as the aforementioned EIT filtering [61]. They remain in the ensemble due to radiation trapping [173] and with the coupling field are promoted to the Rydberg state. Although they are subsequently transferred to the excited state via the coupling field and eventually leave the ensemble, they block the ensemble for some short time. However, some of these excitations may decay to other Rydberg levels due to collisions or other processes. As these states are not coupled with the coupling field, these pollutants are stationary and have a longer lifetime, limited by the respective state's lifetime. While their impact should be less pronounced due to weaker interactions with the desired Rydberg level, they can persist for an extended duration.

In the case of EIT, the expression for the blockade radius differs as the relevant energy scale is governed by the single-atom EIT linewidth, $\gamma_{\mathrm{EIT}} = \Omega_c^2/2\Gamma$ [26]. The typical expression for the blockade radius is given as:

$$r_b = \sqrt[6]{\frac{C_6}{2\hbar\gamma_{\mathrm{EIT}}}} = \sqrt[6]{\frac{C_6\Gamma}{\hbar\Omega_c^2}}. \tag{5.4}$$

However, different expressions can be found in the literature[4]. Since the blockade radius is understood as a parameter setting the relevant length scale in the system, given different expression found in the literature, one should be careful when using it to compare different experiments. One should notice, however, that for a typical experimental parameter range, the differences between different expressions are less 25 %. For our usual experimental parameters at $n = 90$, the blockade radius is $r_b = 10.5\,\mu\mathrm{m}$.

It's worth highlighting that, in theory, photons from an EIT source are anticipated to exhibit reduced state purity due to scattering events [111], which may diminish their suitability for quantum communication applications. As of now, no experimental verification of this phenomenon has been documented. We speculated about this effect as a potential explanation for the comparatively lower visibility of the HOM interference of weak coherent states and EIT photons in comparison to photons generated via the OR method [174]. However, the available data was insufficient to draw definitive conclusions.

5.2 Decoherence in Rydberg ensembles

Decoherence sources in our system introduce limitations and imperfections in both the EIT and OR methods of single-photon generation. In this section, we discuss dephasing mechanisms affecting the stored spin wave and noise processes during spin wave creation, and how they affect the generation efficiency. We also examine specific effects exclusive to the OR excitation technique. Our aim is to understand these decoherence sources to possibly mitigate them and optimize the efficiency and fidelity of our single-photon source.

5.2.1 Decoherence of Rydberg spin wave

Decoherence processes play a critical role in our system, particularly evident in the short decay time of a stored Rydberg spin wave. It is typically less than 2 µs – over 100 times shorter than the radiative lifetime of the Rydberg state. Consequently, it

---

[4] In one of the first papers treating about the interactions of the rEIT polaritons by Gorshkov et al. [41] the blockade radius is given as $r_b = \sqrt[6]{\frac{C_6\Gamma}{2\hbar\Omega_c^2}}$, while in a seminal paper by Peyronel et al. [58] $r_b = \sqrt[6]{\frac{2C_6\Gamma}{\hbar\Omega_c^2}}$. In [61], for a situation almost identical to ours, based on a heavy theoretical consideration from [95], the blockade radius is expressed by $r_b = \sqrt[6]{\frac{C_6}{\hbar}\left(\frac{\Gamma}{\Omega_c^2} + \frac{1}{\Gamma}\right)}$. In general, the blockade radius can be also defined as a minimum distance between two rEIT polaritons and the exact expression depends on the particular problem [95].

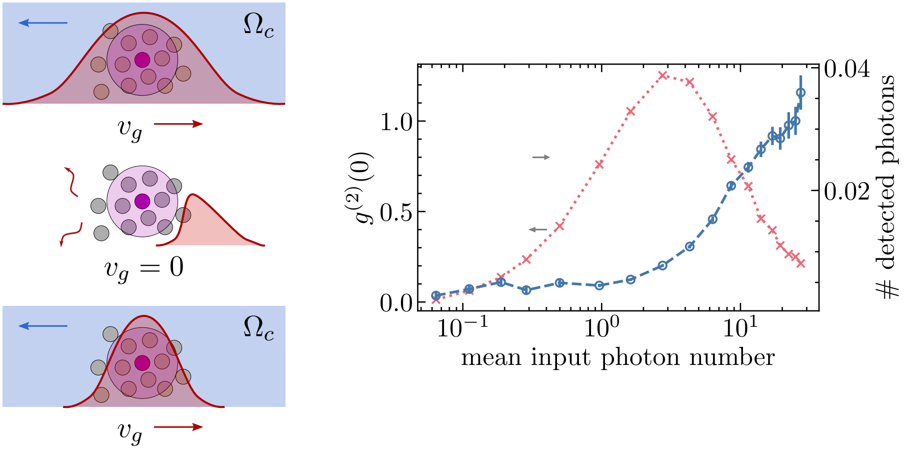

Figure 5.2: EIT photon generation. (left) Schematic representation of the EIT scheme time-filtering property. A pulse (longer than the group delay) propagates under EIT conditions, forming rEIT polaritons. When the pulse is inside the ensemble, the coupling field Ω_c is switch off, freezing the polariton propagation. Part of the pulse, that already passed through the ensemble, propagates further. Part of the pulse, that has not reached the ensemble, gets scattered. After a programmable storage time, the coupling field is turned on and the polariton continues to propagate, eventually becoming a photonic pulse. (right) A typical characterization curve of the EIT photon generation at $n = 90$. Autocorrelation $g^{(2)}(0)$ and the mean detected photon number as a function of the mean input photon number. One should notice that the pulses are longer than the group delay, so not all the photons can be stored in the medium. One can see that there is a clear trade-off between larger number of generated photons and their quality. The decrease of the generation probability for large input photon numbers is explained in the main text.

becomes imperative to identify and understand the various sources of decoherence affecting our system.

Rydberg spin waves and rEIT polaritons can be viewed as essentially the same phenomenon [61], implying that they are both susceptible to dephasing in similar if not identical ways. To understand the dephasing mechanisms in our system, let us first consider the spin wave state $|R\rangle$ immediately after its creation, at time $t = 0$. In a simplified model that neglects variations in the excitation processes among different emitters, the spin wave can be expressed as follows:

$$|R\rangle = \frac{1}{\sqrt{N}} \sum_i e^{i\Delta \boldsymbol{k} \cdot \boldsymbol{r_i}} |g_1 g_2 \dots r_i \dots g_N\rangle \,. \tag{5.5}$$

Here, $|g_i\rangle$, $|r_i\rangle$, and $\boldsymbol{r}_i$ denote the ground state, the Rydberg state, and the position of atom i, respectively. The net wave vector of the exciting field is denoted as $\Delta\boldsymbol{k}$, which in our case is the sum of the wave vectors of the probe field $\boldsymbol{k_p}$ and the coupling field $\boldsymbol{k_c}$. Since the spin wave is created in a ladder scheme, we have $\Delta\boldsymbol{k} = \boldsymbol{k_p} + \boldsymbol{k_c}$. Because the fields in our setup are counter-propagating (for reasons explained later in this section), $|\Delta \boldsymbol{k}| = |\boldsymbol{k_p}| - |\boldsymbol{k_c}|$.

One of the most readily observable consequences of spin wave dephasing is a reduction in the generation probability, η, as a function of storage time t. This decrease is often modeled by calculating the overlap squared of the time-evolved spin wave state, $|R(t)\rangle$, with respect to the initial state, $|R\rangle$ [175, app. A]:

$$\eta \propto |\langle R|R(t)\rangle|^2. \tag{5.6}$$

Here, we assume that $|R\rangle$ represents the state that can be retrieved with the highest efficiency. During the storage time, each emitter accumulates a phase $\varphi_i(t)$, which may differ among emitters due to various noise processes. Thus, we can express the overlap squared as:

$$|\langle R|R(t)\rangle|^2 = \left|\frac{1}{N}\sum_{i=1}^{N} e^{i\varphi_i(t)}\right|^2 \approx \left|\int n(\varphi(t)) e^{i\varphi(t)} d(\varphi(t))\right|^2. \tag{5.7}$$

In the last step, we take the continuous limit [176, sec. 2.4.2], and $n(\varphi(t))$ represents the probability distribution of the phases at time t. From this expression, we observe that η is maximized when the phases for all emitters evolve identically. Conversely, any discrepancy in the phase evolution of components corresponding to different emitters diminishes the efficiency.

In the following paragraphs, I will discuss different sources of the Rydberg spin wave dephasing. As a metric, I will consider the coherence time, defined as the time it takes for the single photon generation probability to decay to $1/e$. We typically observe a coherence time of 1.8 µs.

Motional dephasing

In our ensemble, the atoms exhibit thermal motion due to their finite temperature. Assuming no atom-atom collisions, the position of atom i at time t can be expressed as $\boldsymbol{r}_i(t) = \boldsymbol{r}_i + \boldsymbol{v}_i t$, where $\boldsymbol{v}_i$ is the velocity of the atom. Consequently, the phase accumulated by each atom is given by

$$\varphi_i(t) = \Delta \boldsymbol{k} \cdot (\boldsymbol{r}_i + \boldsymbol{v}_i t), \tag{5.8}$$

where we neglect the phase contribution from the kinetic part of the Hamiltonian (which cancels out when computing the fidelity). Assuming a thermal gas, we can approximate the velocity distribution to follow the Boltzmann distribution. By considering this, one can easily derive that

$$\eta \propto \exp\left\{-\frac{k_B T |\Delta \boldsymbol{k}|^2}{m} t^2\right\}, \tag{5.9}$$

which corresponds to a Gaussian function with a characteristic time $\tau = \sqrt{m/k_B T |\Delta \boldsymbol{k}|^2}$, which we can identify as the coherence time.

To minimize $\Delta\boldsymbol{k}$, we choose a geometry where the probe beam and the coupling beam are counter-propagating, giving $|\Delta\boldsymbol{k}| = |\boldsymbol{k_c}| - |\boldsymbol{k_p}|$. However, due to significant mismatch in wavelength between the probe and coupling fields, the resulting $\Delta\boldsymbol{k}$ is still large, requiring our atoms to be extensively cooled. We plot τ as a function of temperature in fig. 5.3(left). For typical experimental parameters, we find $\tau = 3.4\,\mu\mathrm{s}$, which we identify as a relevant factor, although it may not be the dominant contributor to the Rydberg state decoherence.

Another supporting point for this conclusion is the non-Gaussian nature of the observed decay in η. It exhibits characteristics that fall between a Gaussian and exponential decay, indicating the presence of an additional relevant dephasing mechanism.

For a more complete derivation, I refer the reader to [177].

Residual magnetic field

The presence of a magnetic field causes a (hyper)fine level to split into Zeeman sublevels, with the number of sublevels given by $2X + 1$, where X corresponds to the total orbital angular quantum number J for fine structure states or the total atomic angular quantum number F for hyperfine structure states. When atoms occupy different Zeeman sublevels, the presence of a non-zero magnetic field leads to dephasing, as the atoms accumulate phase at different rates due to their varying energies. To address this issue, it is common practice to optically pump all atoms into a single Zeeman sublevel. Unfortunately, we have been unable to implement Zeeman optical pumping within our setup, leaving us vulnerable to residual magnetic fields.

To mitigate this, we cancel the residual magnetic field by looking at spectra of the microwave spectroscopy on the $|F = 1\rangle$-to-$|F = 2\rangle$ transition[5]; a typical scan can be seen in fig. 5.3(right). By adjusting the current in the compensation coils, we can merge the distinct peaks associated with different transitions between Zeeman substates into a single peak. This merging signifies the absence of a background magnetic field, a crucial requirement for our experiments.

However, the resulting peak exhibits a residual width that surpasses the magnetic dipole-allowed transition width. We attribute this broadening to magnetic field gradients, which we cannot compensate with our current setup. This results in a position-dependent energy shift, over time contributing to the dephasing of the spin wave. We can typically reduce its FWHM to below 50 kHz, corresponding to a magnetic field variation of approximately 24 mG within the atomic cloud[6].

Rydberg levels are often approximated as fine structure states and, therefore, have different magnetic moments than the ground state [179, sec. 6.9]. Nevertheless,

---

[5] For details of the microwave spectroscopy setup, I refer the reader to [178, sec. 4.1.3]

[6] This estimate assumes that states that contribute the most to the splitting have the largest magnetic moment difference between the Zeeman sublevels, namely $|F = 1, m_F = 1\rangle$ and $|F = 2, m_F = 2\rangle$.

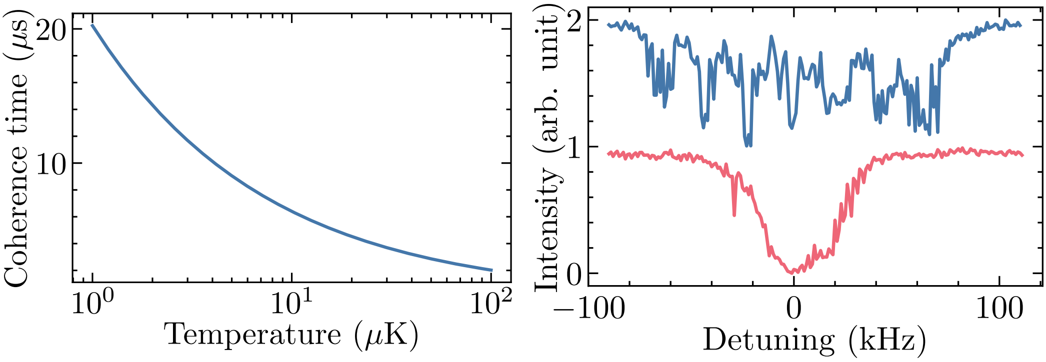

Figure 5.3: (left) Spin wave coherence time vs the ensemble temperature. Moving atoms scramble the spin wave phase, leading to lower retrieval efficiency. (right) In typical microwave spectroscopy scans of the $|5S_{1/2}, F = 1\rangle$ to $|5S_{1/2}, F = 2\rangle$ transitions, two distinct situations can be observed. In the top plot, where the magnetic field is not compensated, nine allowed transitions are visible. However, two pairs of transitions experience the same net Zeeman shift, leading to overlapping peaks. The measurement appears noisy, but the exact reason for the noise is unknown. In the bottom plot, the magnetic field is compensated, resulting in all the peaks collapsing into a single structure. The residual width of this structure, approximately 45 kHz, can be attributed to magnetic field gradients that cannot be compensated in our setup. The top curve is shifted for clarity.

the broadening of the ground state to Rydberg state transition should remain below 50 kHz[7]. Due to multitude of transitions involved in this dephasing process, it's difficult to give an exact number for τ, however, it should remain larger than 20 µs. Therefore, we do not consider this broadening to be a limiting factor for our system.

Background electric field

Stray electric fields present another potential source of decoherence in our system. Similar to the magnetic field, an electric field can induce energy shifts in the atoms. Any variation of this shift within the atomic cloud results in a position-dependent phase shift, which contributes to the dephasing of the spin wave. The large polarizability of Rydberg atoms makes them particularly sensitive to the effects of electric fields.

In the case of a homogeneous background electric field, its impact on our system is minimal. This is because all levels with $J = 0$ or $J = 1/2$ experience only a scalar Stark shift [102, sec. 7.4.2.2], given by

$$\Delta E^{(0)}_{\text{Stark}} = -\frac{1}{2}\alpha^{(0)}(J)\, E^2, \tag{5.10}$$

where J represents the total electron angular momentum, E is the electric field amplitude, and $\alpha^{(0)}(J)$ denotes the scalar polarizability which depends on the total

---

[7] We again took for this estimation states with the largest magnetic moment difference that should be connected in our excitation scheme, namely $|5S_{1/2}, F = 2, m_F = 1\rangle$ and $|nS_{1/2}, m_J = -1/2\rangle$.

electron angular momentum J, but is independent of the total atomic angular momentum F. Both the ground state and the Rydberg state would experience a shift in their energies due to the homogeneous electric field, resulting in a shift in the transition frequency but not broadening.

In the case of the EIT scheme, one might be concerned about the involvement of the excited state, which is a P-state that experiences a tensor shift dependent on the absolute value of the projection of the total atomic angular momentum $|m_F|$ [102, sec. 7.4.2.4]. However, in our context, the absolute values of the Stark shift for low-lying states are negligible. Even assuming an atmospheric potential gradient of 0.8 V/cm (which is likely an overestimation due to the presence of metallic structures partially shielding the experiment), the maximum tensor Stark shift between different m_F levels would be well below 1 Hz.

The situation changes when considering gradients of electric fields. While the ground state is minimally affected due to its small polarizability, Rydberg levels exhibit a significant susceptibility to such gradients, as indicated by their large polarizabilities (cf. Table 2.1). For instance, the $90S_{1/2}$ state can experience a broadening of 500 kHz when subjected to an electric field difference of 17 mV/cm over the length of the atomic cloud. It is unlikely to have such a strong static gradient, which would correspond to approximately 11 (V/cm)/cm for our system. However, electromagnetic radiation at relevant frequencies ranging from hundreds of kHz to tens of MHz, such as that emitted by switching-mode power supplies, could potentially cause issues. As a reference, a 50 kW AM radio station would produce a radio signal with an amplitude of about 17 mV/cm at a distance of 100 km.

It is challenging for us to quantify the exact effect of external radiation, but it is plausible that this factor could limit our coherence time, since we do not currently screen our atoms from external radiation. We also consistently observe significant day-to-day variations in the coherence time of our system, which do not exhibit any correlation with any monitored parameter. Currently, out of lack of any better explanation, we attribute these variations to fluctuations in the background electromagnetic radiation.

AC Stark shift

In our experimental setup, we do not observe decoherence due to the AC Stark shift, because we turn off the dipole trap when probing the atoms. However, it is worth discussing this phenomenon as it is a common challenge in Rydberg systems.

The AC Stark shift occurs when atoms interact with a fast oscillating electric field, which is typically provided by a far-detuned dipole trap light. This shift is proportional to the laser intensity[8]. In the case of so-called red-detuned dipole traps,

---

[8] In a general case, the relation between the electric field and the AC Stark Shift is more complicated. However, for our case of the Rydberg state being an S-state and a linear polarization of the dipole trap, the shift should be indeed proportional to the laser intensity. For details, see [102, sec. 7.7].

where the atoms are attracted towards the region of highest intensity, there can be a substantial variation in the laser intensity experienced by the atoms across the ensemble, from the center to the edges. This variation leads to a position-dependent phase shift, contributing to the dephasing of the spin wave [177].

To partially mitigate this effect, researchers have explored the use of "magic" wavelengths for the dipole trap. These are specific wavelengths where the AC Stark shifts experienced by the relevant states, namely the ground and Rydberg states, are equal. Although perfect cancellation is challenging to achieve, it is possible to make the relative shift small enough that it does not significantly impact the system's coherence [180, 181].

However, at the wavelength of our dipole trap, an additional effect known as the antitrapping of Rydberg atoms takes place. While atoms in the ground state are attracted to the highest intensity of the trapping beam, this phenomenon causes atoms in the Rydberg state to be repelled from the trap. The reason behind this behavior is that the polarizabilities of the ground and Rydberg states have opposite signs for the electric field at this specific frequency.

To circumvent these effects, we pulse the dipole trap during the interrogation time.

Mutual dephasing of Rydberg spin waves

If the ensemble is larger than the blockade radius, more than one Rydberg excitation can exist. They interact with each other, what results in a position-dependent energy shift experienced by the atoms. Over the storage time, this energy shift transforms into a position-dependent phase shift, leading to a decrease in the retrieval efficiency [168]. This dephasing effect can be observed in our system as a reduction in the storage time with increasing Rabi angle or number of input photons, depending on the excitation protocol, as shown in fig. 5.4(left).

This dephasing phenomenon occurs specifically when multiple excitations are present in the ensemble. In the case of a single excitation in the cloud, the retrieval efficiency remains unaffected. This effectively changes the outgoing pulse statistics compared to the input pulse, enhancing the single-photon nature of the emitted pulse [169]. In our system, this effect plays a role in maintaining a low autocorrelation $g^{(2)}(0)$ despite the ensemble not being fully blockaded.

Although quantifying the exact impact of this effect is challenging, based on the presented data in fig. 5.4, it appears to be a relevant factor, but not the limiting one, as at a very low number of input photons we still observe short coherence time.

Density-dependent dephasing

Another source of dephasing observed in our system arises from the relatively high peak density of our ensemble, where the average distance between atoms becomes smaller than the Rydberg atom radius. In this scenario, the valence electron of a Rydberg atom can scatter off a neutral atom, leading to the formation of a molecule

[75][9]. This molecule formation has been found to induce density-dependent dephasing [50]. Subsequently, the resonances associated with these molecular interactions were directly observed [75].

The interaction between atoms due to scattering, in a mean-field picture, is proportional to the atomic density. Since the density within the cloud is non-uniform, the relative phase shift experienced by the emitters is also non-uniform, resulting in a spin wave dephasing. We have plotted the decoherence rate, defined as the inverse of the coherence time, as a function of optical depth in fig. 5.4(right). The dependence appears to be linear, similar to the findings in [50], although the slope in our case is 1.5 times larger. The model presented in their work [175, sec. 4.4], which fits their data well, does not have any free parameters and should be suitable for our experimental conditions. We are uncertain about the reason for the discrepancy. It could be attributed to inaccurate estimation of atomic density, however, this seems unlikely.

The crucial point to consider is the behavior at zero density, which gives a coherence time of 2 µs. This suggests that even in the absence of any density-dependent dephasing, our coherence time would still be relatively short.

It is worth noting that the presence of molecular resonances not only impacts existing spin waves but also affects the blockade radius in the EIT scheme. When the binding energy of the molecules is small, their resonances can overlap with the EIT transparency window, resulting in its broadening and a reduction of the blockade radius, cf. eq. 5.4. However, this effect is predicted to be significant only for ensembles at much higher densities than ours [75].

5.2.2 Decoherence of propagating rEIT polaritons

Having discussed the various decoherence processes that can impact the existing spin wave, let's now turn our attention to the processes that affect its creation. In this section, I will focus on the noise sources that can influence rEIT (Rydberg-EIT) polaritons. In the subsequent section, I will discuss the OR (off-resonant) scheme.

Coupling laser linewidth

The presence of phase noise in the emitted laser field leads to a finite laser linewidth. Lasers are tools used to establish coherence between different atomic levels, therefore, large laser linewidth would introduce phase noise in our system and have negative impact on our experiments.

Typically, the impact of laser phase noise is modeled as a pure dephasing term [182–184]. In the case of EIT, the relevant laser is the coupling laser, and its finite linewidth increases the dephasing of the excited and Rydberg states [185, sec. IIIA]. In the absence of other dephasing mechanisms, it could be identified with γ_r in fig. 2.3(right) or eq. 2.17. The former is typically of larger concern, as the dephasing

---

[9] For a detailed explanation of this phenomenon, refer to Baur's thesis [175, sec. 4.4]

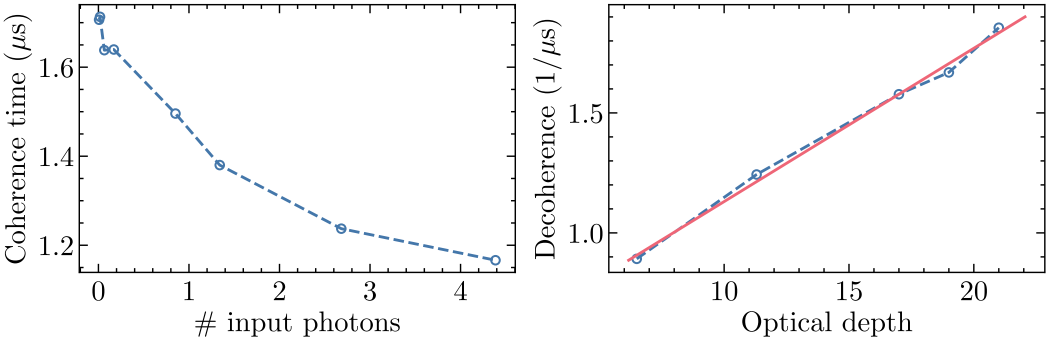

Figure 5.4: Decoherence of the rEIT polariton stored in our ensemble. (left) Coherence time of EIT storage vs number of input probe photons per blockade time. For a larger number of input photons, there is a higher chance of creating more than one Rydberg excitation in the ensemble which interact and dephase. Hence, a decrease in the coherence time with the probe photon number. For large input photon numbers, the coherence time should approach a constant value, as only a finite number of Rydberg excitations can fit in our ensemble. (right) Decoherence rate extracted from an exponential fit of the storage efficiency decay as a function of the optical depth of our ensemble. In dense ensembles, collision of electrons of the Rydberg atoms with nearby ground state atoms result in additional dephasing. The red line is a linear fit, discussed in sec. 5.2.1.

of the Rydberg state is usually the main limiting factor for establishing large EIT transparency. In our system (after the update of the locking system), the estimated linewidth of the coupling laser is around 60 kHz (for more details, see sec. 3.3.3). We can extract the dephasing rate from fits of the observed EIT spectrum to eq. 2.21. Typically, we would obtain the dephasing rate larger than 300 kHz. Based on these observations, we conclude that the laser linewidth is not the limiting factor in achieving better EIT transparency.

Finite coupling beam size

Another important consideration is the impact of the finite size of the coupling beam, which introduces an inhomogeneous Rabi frequency across the atom ensemble.

Let us recall that our single-photon source can be regarded as an EIT quantum memory designed to accommodate only a single photon. Ideally, in this memory, we should be able to populate only the so-called symmetric Dicke states [105] These are the states that form in the polariton's state. However, an inhomogeneous coupling field Rabi frequency breaks the necessary symmetry and non-symmetric Dicke states start being populated. These states cannot be efficiently mapped into photons [186, sec. 1.2.2], leading to lower single-photon generation efficiency.

To mitigate this issue, it is a common practice to employ a coupling beam significantly larger than the probe mode. In our case, the difference in size is relatively modest, with the probe mode diameter of 13 µm and the coupling mode diameter of 22 µm. To my knowledge, it has not been studied how the coupling Rabi frequency inhomogeneity affects the EIT transmission. However, considering that the variation of the coupling Rabi frequency within the probe mode is 29 % (given by the probe waist), it might be worth reducing the size of the probe mode to enhance the uniformity of the coupling Rabi frequency.

It's relevant to note that the finite size of the probe mode can also influence the coherence time consideration, as discussed in [177]. Nevertheless, in a setup with geometry similar to ours, they managed to achieve a coherence time of 30 µs, indicating that this effect has minor significance in our context.

Doppler effect

The residual motion of the atoms also introduces the Doppler effect. Although the Doppler shift for atoms moving with velocities equal to RMS of the Boltzmann distribution is approximately 50 kHz, the residual motion should have no noticeable effect on the EIT spectrum in our system. To confirm this, we performed a simple numerical computation where we integrated the susceptibility given in eq. 2.17 over the Boltzmann velocity distribution. Our results showed that only at a temperature of 10 mK did we start to observe a slight Doppler broadening effect on the EIT spectrum.

5.2.3 Decoherence in OR excitation

Off-resonant (OR) excitation is influenced by various noise processes that can impact its performance. These noise processes can be broadly classified into two categories: those that introduce decoherence and decrease the visibility of Rabi oscillations, and those that solely affect the fidelity of the Rabi flop. Similarly to the decoherence processes described above for rEIT polaritons, these noise processes are present only during the creation of the spin wave, i.e. during the Rabi flop. All the decoherence rates estimated in this section should be compared to the collectively enhanced two-photon Rabi frequency $\sqrt{N}\Omega_R/2\pi \sim 2\,\mathrm{MHz}$ (see sec. 2.2.2 and eq. 5.1) to evaluate their relevance in the excitation process [162, sec. IIIA].

Residual population in the excited state

In the OR scheme, our system can be approximated as a two-level system, as discussed in sec. 5.1.1. However, as the detuning from the intermediate (excited) state, $|e\rangle$, is finite, there is a small residual population in this state. As $|e\rangle$ is short-lived and its population decays quickly, this leads to a loss of coherence in the system and, consequently, damping of the Rabi oscillation [102, sec. 5.5.2][10]. The scattering rate

---

[10] Scattering from the excited state might also lead to a population trapping, if there exist other decay channels than only to the ground state [162, sec. IIIB]. In our case, the decay to the ground state is the only dipole-allowed process, therefore we do not consider this effect to be important in our system.

due to this residual population is given by [102, sec. 6.1.2]

$$\Gamma_{\mathrm{OR}} \approx \Gamma p_{\mathrm{res}} \approx \Gamma \left(\frac{\Omega_c}{2\Delta_p} \right)^2 , \tag{5.11}$$

where p_{res} is the residual population in the excited state. For our experimental parameters, $\Gamma_{\mathrm{OR}}/2\pi = 80\,\mathrm{kHz}$, so we don't consider it a limiting factor[11].

Laser linewidths

As discussed in sec. 5.2.2, finite laser linewidths introduces additional dephasing. This manifests as a reduction in the Rabi oscillation amplitude, as reported in [162, sec. IIIC]. However, considering that the combined linewidth of our lasers is expected to be less than 65 kHz, we anticipate that its impact on our system is small.

Doppler shifts distribution

In our ensemble, the atoms move with velocities following the Boltzmann distribution, resulting in each atom experiencing a different Doppler shift and effectively a different detuning from the resonance. In our experimental setup, the probe and coupling lasers are counter-propagating, leading to an effective wave vector magnitude of $|\Delta \boldsymbol{k}| = |\boldsymbol{k_c}| - |\boldsymbol{k_p}|$, where $\boldsymbol{k_p}$ and $\boldsymbol{k_c}$ represent the wave vectors of the probe and coupling fields, respectively. The distribution of Doppler shifts follows the Gaussian distribution with a standard deviation given by $\Delta \boldsymbol{k}\, v_{\mathrm{RMS}}$. Here, $v_{\mathrm{RMS}} = \sqrt{k_B T/m}$ corresponds to the RMS velocity obtained from the one-dimensional Boltzmann distribution, considering the temperature T and atomic mass m. In our case, FWHM of this distribution is approximately 110 kHz, therefore, we are not concerned about this effect. Moreover, we plan to improve our cooling stage to reduce the motional dephasing of the spin wave, cf. sec. 5.2.1.

Finite laser beam size

The finite size of the laser beams has already been discussed in the context of EIT polariton propagation (see sec. 5.2.2). In the OR scheme, the different Rabi frequencies experienced by individual emitters lead to a distinct phase evolution for each atom, resulting in a dephasing process. Unlike in EIT, both the coupling and

---

[11] Γ_{OR} is not necessarily the rate at which the Rabi oscillation decays. According to lecture notes from Ivan Deutsch [187], for a simplified but still realistic model, this rate is given by

$$\Gamma_{\mathrm{Rabi}} = \frac{\Omega_p \Omega_c \Gamma}{4\Delta_p^2}.$$

Since the problem is not numerically difficult and to be able to take into account all relevant effects, de Léséleuc et al. [162, sec. IIIB] analyzed this decay numerically. In any case, for our parameters, this effect should not pose a problem.

probe fields contribute to the effective Rabi frequency, amplifying the inhomogeneity even further.

In our case, the ensemble size exceeds the probe mode size, making the effective interaction region being defined by the probe waist. Within the FWHM of this interaction region, we estimate a significant variation of approximately 37 % in the effective Rabi frequency. Enlarging the difference in size between the coupling and probe beams would help reduce the contribution from the coupling field's inhomogeneity. However, this would solve only part of the problem as the variation primarily arises from the amplitude variation of the probe field, which also defines the interaction region, so simply cannot be mitigated. Unless one allows for the probe mode to be larger than the ensemble, however, such a configuration would not suitable for other purposes than photon generation.

To enhance the efficiency of population transfer, the use of composite pulses instead of typical π-pulses could mitigate partially the effect of finite laser beam size [188].

Finite dipole interaction strength

Another source of decoherence affecting OR excitation in Rydberg ensembles stems from the finite dipole interaction strength. We will follow a model introduced in [189] which they used to explain diminishing Rabi oscillation amplitude[12].

Consider an ensemble that is smaller than the blockade radius – due to the dipole interactions, the singly excited state (with one Rydberg excitation) is not coupled to the doubly excited state (with two Rydberg excitations) by the driving field. Interaction strength, however, depends on the atom's position relative to the Rydberg excitation. It means that each of the doubly excited states has different energy, depending on the relative position to the Rydberg atom. Assuming the interaction strength is significantly larger than other parameters, we can adiabatically eliminate these doubly excited states, similar to what was done with the excited state in sec. 5.1.1.

This adiabatic elimination leads to two important consequences. Firstly, it introduces an AC Stark shift that changes the resonance frequency of the $|g\rangle$ to $|r\rangle$ transition, which is position-dependent and distinct for each atom (as the interaction is position-dependent). Secondly, it couples different singly-excited states via position-dependent Raman transitions. This leads to a decay of the ideal Rydberg spin wave state, given by eq. 2.10, into this quasi-continuum of singly-excited states, reducing the Rabi oscillation amplitude[13]. It should be noted that when the interaction strength is infinite, we return to the simple picture of two collective states discussed in sec. 5.1.1.

Given the complexity of the model, it is only possible to estimate the scaling of

---

[12] For a nicely explanatory derivation, I refer the reader to Vaneecloo's thesis [186, sec. 7.1.1]

[13] One can alternatively see this as an inhomogeneous broadening mechanism whose origin is position-dependant interaction between the atoms.

this decoherence process [189]:

$$\gamma_{\text{int}} \propto \frac{N\Omega_N^2}{U} = \frac{N^2(\Omega_p\Omega_c)^2}{4\Delta_p^2 U}, \tag{5.12}$$

where Ω_N represents the collectively enhanced two-photon Rabi frequency, and U denotes the interaction strength at a distance equal to the ensemble size.

An evident approach to reduce the impact of this decoherence source is to make the blockade radius significantly larger than the ensemble size. However, in our case, the blockade radius remains smaller than the ensemble size, thereby this decoherence process is reinforced by another resulting from interactions between multiple Rydberg excitations, as discussed in sec. 5.2.1. The former acts at distances shorter than the blockade radius, while the latter operates at larger distances.

Reduced population transfer fidelity

There are several effects that can influence the effective Rabi frequency without inducing decoherence, yet leading to a decrease in π-pulse fidelity. These processes are not directly related to the decoherence of the quantum system, but rather to the ability to reproduce the same experimental conditions throughout the entire integration time.

One such effect arises from fluctuations in the number of atoms in the ensemble. As the effective Rabi frequency depends on the number of atoms within the dipole blockade, atom number fluctuations introduce uncertainty in the π-pulse area. This effect becomes more pronounced for smaller ensembles, as fluctuations are expected to follow Poisson statistics and scale with the square root of the atom number. In our case, with an estimated atom number[14] of approximately 700, the fluctuations are on the order of 4 %. We do not consider this to be a significant issue in our system.

Another factor that reduces the fidelity of a π-pulse are the slow drifts of experimental parameters, such as laser power or frequency. In our system, we observe minimal power fluctuations, and we regularly make adjustments to compensate for them, so we are not concerned about this aspect. Unfortunately, we do observe significant fluctuations of approximately 1 MHz in the coupling laser frequency, which is substantial even when considering the broadening mechanisms discussed earlier. We attribute these fluctuations to imperfections in the locking system, as discussed in sec. 3.3.3. On the other hand, we believe that the probe light frequency remains stable to within tens of kHz, so it should not pose any significant concerns.

5.2.4 Summary

Let's bring together the various sources of decoherence we've discussed and consider our options for managing them.

---

[14] We consider here only the atoms that are in the probe mode.

Motional dephasing, explored in sec. 5.2.1, emerges as a significant factor. Further cooling of the ensemble should help, as it was shown in [177]. This not only aids in mitigating motional dephasing, but also offers advantages like reducing ensemble size, as explained in sec. 3.1.2. Additionally, cooling would help mitigate the Doppler effect and its associated frequency detunings, discussed in sec. 5.2.3. Another approach one could consider is the use of an optical lattice to suppress the motion of atoms, as in [181]. However, in our case, this method would require a substantial experimental effort.

Concerning static magnetic and electric background fields, our analysis in sec. 5.2.1 and sec. 5.2.1 suggests minimal adverse effects. However, it's wise to consider the potential influence of slowly varying electric fields originating from lab equipment or external sources, possibly necessitating screening. Moreover, in cases where higher principal quantum numbers are involved, the strong polarizability scaling (refer to Table 2.1) might demand electric field compensation.

Making our ensemble strongly blockaded would be beneficial, countering the mutual dephasing of Rydberg excitations (sec. 5.2.1) and mitigating finite interaction strength effects (sec. 5.2.3). Enhanced cooling, as mentioned earlier, contributes to achieving this goal.

While laser linewidths appear to be within reasonable bounds, some aspects warrant careful attention. Certain effects, such as density-dependent dephasing (sec. 5.2.1) and non-uniform Rabi frequency (sec. 5.2.2 and sec. 5.2.3), pose challenges that might be hard to circumvent. However, increasing the size ratio between the coupling and probe modes can offer an improvement for the latter issue.

To sum up, managing decoherence in our system involves a mix of strategies. Careful cooling to minimize motional dephasing, vigilance against slowly varying electric fields, striving for stronger blockade, and optimizing mode ratios are promising approaches. By implementing these changes, we can hope for a significant in improvement in the performance of our experimental setup.

Chapter 6

Raman storage of quasideterministic single photons generated by Rydberg collective excitations in a low-noise quantum memory

This chapter describes an experiment that involved the collaboration of two distinct setups. I was responsible for the Rydberg setup, which served as the single-photon source, while my colleague, Lukas Heller, operated another cold-atomic setup used as a quantum memory. The data was collected with a help of two post-docs, Auxiliadora Padrón-Brito and Klara Theophilo. Our experimental results have been published in [190], and the content of this chapter is based on that publication. All the figures presented in this chapter are taken directly from this publication.

While finalizing our experiment, we learned about a recent experiment where a single photon generated by Rydberg atoms was stored in an atomic ensemble using electromagnetically induced transparency [191].

6.1 Motivation

To date, most of the early demonstrations of quantum repeater links with ensemble-based quantum memories are based on probabilistic light-matter entanglement sources, e.g. based on emissive quantum memories using spontaneous Raman scattering in atomic clouds [192–196], following the Duan, Lukin, Cirac, and Zoller (DLCZ) proposal [11], or by using read-write quantum memories combined with spontaneous parametric down-conversion sources [197, 198]. However, these types of probabilistic sources lead to limitations due to a trade-off between excitation probability and fidelity of the generated state. To keep the errors due to the generation of multiple pairs low, and therefore the fidelity high, the generation probability must remain low. This trade-off leads to low success probability per trial (especially for multiple-link repeaters), which limits the overall high-fidelity entanglement rate [199].

A quantum repeater architecture based on the use of deterministic single photons and absorptive ensemble-based quantum memories was proposed to overcome this limitation [12]. In this scheme, each node consists of a deterministic single-photon source and a quantum memory. The single photon is sent on a beam splitter (BS) and one output of the BS is directed towards the quantum memory while the other output is converted to telecom wavelength and sent to a central station where it is mixed with the photonic mode from another distant quantum node. It has been shown that heralded single photons (generated from probabilistic sources) can be stored in quantum memories [200, 201] with up to 87 % storage and retrieval efficiency [107, 202]. Hence, the main challenge of this scheme compared to schemes using probabilistic sources is to generate memory-compatible indistinguishable single photons on demand with high efficiency. In addition, the quantum memory should feature very low noise in order not to degrade the single photon properties.

Several approaches have been demonstrated to generate on-demand single photons using single emitters such as quantum dots, single molecules and color centers in diamond. However, most of these photons are not resonant with quantum memories and have a bandwidth much larger than the one of long-lived quantum memories. While progress has been made recently to interface photons from quantum dots and molecules to atomic vapors or rare-earth doped solids [203–206], so far high efficiency and long-lived storage of these photons has not been demonstrated. Single trapped atoms can be used to generate directly resonant and memory-compatible photons that have been interfaced with a BEC quantum memory [207], however, the efficient photon generation in a single mode requires placing the atom in a high-finesse cavity, which represents an experimentally complex task. In recent years, several experiments have shown that ensembles of Rydberg atoms could serve as a source of on-demand narrowband [57, 59, 92, 167] indistinguishable single photons [62, 174, 180]. This approach has the advantage that no high-finesse cavity is required, due to the collective nature of the single photon generation.

In this experiment, we demonstrate the storage and retrieval of an on-demand single photon generated by a collective Rydberg excitation on a low-noise Raman quantum memory located in a different cold atomic ensemble. We show that the single photons can be stored and retrieved with a signal-to-noise ratio (SNR)[1] up to 26, preserving strong antibunching. We also evaluate the performance of the built-in temporal beam splitter offered by the Raman memory. In addition, we demonstrate that the Raman memory can be used to control the single photon waveshape. These results show that single photons generated on demand by Rydberg atoms can be

---

[1] During the final round of revisions for this thesis, Stephan Dürr, one of the reviewers, pointed out that the more precise term should be “signal-to-background ratio”. However, to maintain consistency with the published paper and the conventional terminology used in the literature, we chose to retain the term “signal-to-noise ratio”.

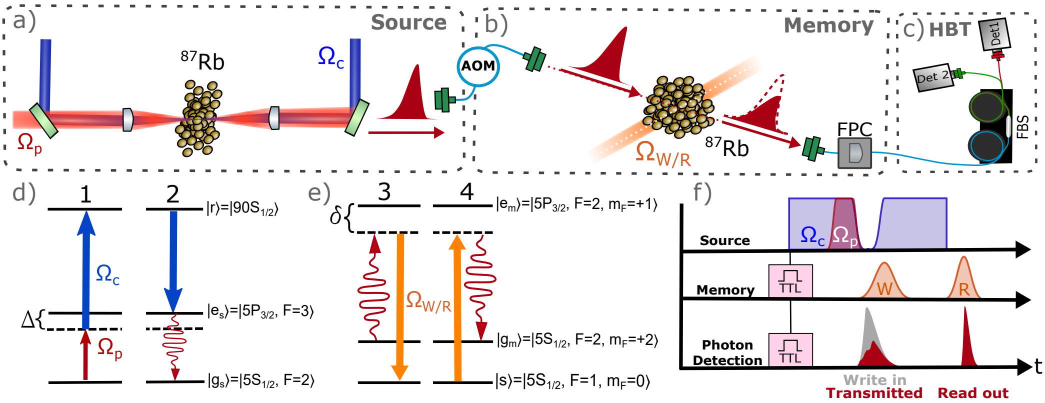

Figure 6.1: A scheme of the experimental setup, the relevant atomic levels and the experimental sequence. (a) The source. The probe (Ω_p) and the counter-propagating coupling beam (Ω_c) are tightly focused in a cold cloud of Rubidium atoms to generate the input photon. (b) The memory. A write-in control beam pulse (Ω_W) maps the incoming photon to an atomic excitation in another cold cloud of Rubidium atoms. The excitation is retrieved with a read-out control beam pulse (Ω_R) and filtered with a Fabry-Perot cavity (FPC). (c) The retrieved photon is split in a fiber-based beam-splitter (FBS) and detected with SNSPD 1 and 2 performing, effectively, an HBT measurement. The relevant atomic levels for the photon generation (d) and for the photon storage (e) are also shown. A two-photon excitation (Ω_p and Ω_c) creates a Rydberg spin wave in $|r\rangle$ (1) which is later mapped to the first excited state $|e_s\rangle$ and decays, emitting a photon (2). The emitted photon is mapped with Ω_W to a ground-state spin wave in $|s\rangle$ (3) and later retrieved with Ω_R (4). (f) The pulse sequence. The whole experiment is synchronized with TTLs sent by the source at the beginning of each generation trial.

stored in an atomic quantum memory, which is an important step towards the implementation of efficient quantum-repeater links using single-photon sources.

6.2 Experimental setup

Our experimental setup comprises two ensembles of cold ^{87}Rb atoms situated in the same laboratory, connected via 12 m of optical fiber cable. One of them is used to generate single photons in a quasi-deterministic way by exploiting the strong dipole-dipole interaction between Rydberg states (the source). Another is used to store and on-demand retrieve the generated photons in an atomic Raman memory.

6.2.1 Rydberg single-photon source

In the first step of the generation protocol, we excite the ensemble from its ground state $|g_s\rangle = |5S_{1/2}, F = 2\rangle$ to a Rydberg state $|r\rangle = |90S_{1/2}\rangle$, see fig. 6.1(d), via a two-photon excitation. We send a weak coherent probe pulse Ω_p and a strong counter-propagating coupling pulse $\Omega_c/2\pi \approx 6\,\mathrm{MHz}$, see fig. 6.1(a). The $1/e^2$ beam radius is 6.5 µm for the probe and 13 µm for the coupling mode. The probe light at a wavelength of 780 nm is red-detuned by $-40\,\mathrm{MHz}$ from the transition to the excited state $|e_s\rangle = \left|5P_{3/2}, F=3\right\rangle$. The coupling light is tuned such that the two-photon transition is resonant with the transition $|g_s\rangle \rightarrow |r\rangle$.

The number of generated Rydberg excitations is strongly limited due to the dipole blockade, as discussed in sec. 2.1.2. The blockade is a result of the strong dipole-dipole interaction between Rydberg states, which prevents a simultaneous excitation of two Rydberg atoms, if they are closer than a distance called the blockade radius. Then, if the interaction region is smaller than the volume given by the blockade radius, only one atomic excitation will be created in state $|r\rangle$ - this is called the fully blockaded regime. The Rydberg excitation is shared between all the atoms in the blockade region, forming a collective quantum superposition, termed Rydberg spin wave.

With a delay of 1 µs, a second coupling pulse is sent resonantly to the $|r\rangle \rightarrow |e_s\rangle$ transition, mapping the Rydberg spin wave onto the excited state $|e_s\rangle$ and triggering the collective emission of a single photon at 780 nm. The photon is emitted in the input mode and in forward direction thanks to collective atomic interference. It is then separated from the coupling light by a dichroic mirror and a band-pass filter, before being collected into a polarization-maintaining single-mode fiber. An electronic trigger is sent to the memory to signal each photon generation attempt.

The generated photon is guided to the second atomic ensemble, the memory. The frequency of the photon is, however, not compatible with the transitions used in the memory, so it is shifted by $-320\,\mathrm{MHz}$ with an acousto-optic modulator (AOM). As a result, the photon is now red-detuned with respect to the $|g_m\rangle \rightarrow |e_m\rangle$ transition.

6.2.2 Raman quantum memory

The Raman memory relies on coherent, adiabatic absorption of the incoming single photon [208]. A storage attempt starts with sending a control write-in pulse Ω_W coupling states $|s\rangle = \left|5S_{1/2}, F=1, m_F=0\right\rangle$ and $|e_m\rangle = \left|5P_{3/2}, F=2, m_F=+1\right\rangle$ off-resonantly by $\delta = -52\,\mathrm{MHz}$, see fig. 6.1(e). The $1/e^2$ beam radius is 69 µm for the photon and 180 µm for the coupling mode. Assuming that the $|g_m\rangle \rightarrow |e_m\rangle$ transition is lifetime-limited, the excited state coherence lifetime is $2\tau_{eg}$, with $\tau_{eg} = 26\,\mathrm{ns}$ the excited state population lifetime. Since the write-in pulse is in two-photon resonance with the input photon, the incoming photon field is transferred to a collective atomic spin excitation on $|s\rangle$. Careful tuning of the control write-in pulse shape, power and timing with respect to the input photon is required to optimize the writing efficiency into the memory. Experimentally, we find that the optimum control write-in pulse closely resembles the input photon waveshape and impinges on the cloud shortly before the photon, with $\Omega_W/2\pi \approx 48\,\mathrm{MHz}$.

To retrieve the stored excitation, after a programmable delay, we send a read-out pulse Ω_R. The read-out pulse is in the same spatial mode as the write-in pulse with the same frequency detuning δ. Owing to the collective atomic interference, the photon is emitted in the input mode in the forward direction and collected into a single-mode fiber. The bandwidth and the shape of the output photon are governed by the temporal profile and the power of the read-out pulse and can be tuned arbitrarily (see sec. 6.3.2).

The collected photons are guided to the detection setup. Depending on the measurement, it is either a superconducting nanowire single-photon detector (SNSPD) or a Hanbury Brown-Twiss (HBT) setup comprised of a fiber-based beam splitter and two SNSPDs, see fig. 6.1(c). We use a HBT setup to measure photons autocorrelation.

6.2.3 Atomic ensembles' preparation details

In this section, we provide a brief overview of the trapping details for both the source and the memory. It's important to note that in this specific experiment, the Rydberg setup is equipped with only one beam of a dipole trap, which differs from the setup described in ch. 3. This configuration leads to a lower optical depth, shorter trapping time, and a larger ensemble size.

In the source, we first load the atoms into a magneto-optical trap (MOT), later compress them and subsequently apply 7 ms of polarisation-gradient cooling. Finally, the ensemble is prepared by optical pumping to its initial ground state $|g_s\rangle = \left|5S_{1/2}, F = 2\right\rangle$. A one-dimensional dipole trap is kept on during the whole process (with a beam waist of 34 µm at an angle of 22° with respect to the probe beam, giving the effective interaction region length of 40 µm (FWHM), and a trap depth of 250 µK). The whole process results in a cloud with OD of 6 and a temperature of 40 µK. Thanks to the dipole trap, the effective interaction region, given by the overlap between the probe beam and the atomic ensemble, is still larger but comparable to the ~ 13 µm of the blockade radius. The ensemble can be interrogated for 200 ms, limited by the population lifetime of the dipole trap (400 ms), before another MOT reloading cycle has to be performed. During its interrogation time, the source attempts to generate a single photon every 4 µs with generation probability $p_{\mathrm{gen}} = 5$ to 15 %.

For the memory, the OD of the ensemble and the cloud temperature are the main parameters governing the storage and retrieval efficiency and the storage time. To achieve a dense and cold ensemble, the atoms are first loaded into a MOT for 10 ms followed by 1.5 ms of polarisation-gradient cooling. Later, the memory is optically pumped to its initial ground state $|g_m\rangle = \left|5S_{1/2}, F = 2, m_F = +2\right\rangle$, in the presence of a homogeneous magnetic bias field oriented along the photon mode. Optical pumping is helpful to avoid beating between spin waves at different Zeeman sublevels. The whole process provides us a cloud with OD of 5 and a temperature of 30 µK. OD starts dropping after 1.2 ms of interrogation time and the trapping cycle has to be repeated.

6.2.4 Limitations and challenges

One of the main challenges of this study were long integration times, which required good stability of both setups. This results mainly from two technical limitations. The first one are very different trapping cycles of the source and the memory, making the overall duty cycle very low. The resulting repetition rate of the whole experiment is 5 kHz. The second one is the passive loss in the photon transmission, which affects quadratically the coincidence probability in the HBT experiment. The total transmission from the output of the source to the detection setup, in the absence of atoms in the memory, is 10(1) %, limited by the fiber coupling after the source (0.4), the frequency-shifter AOM setup (0.62), the fiber coupling after the memory (0.83), the frequency-filtering cavity setup (0.65) and miscellaneous optical and polarisation-dependent losses (0.75). The transmission from the output of the source to the input of the quantum memory is 22 %. The SNSPDs have quantum efficiency $\sim 85\,\%$ and 3 Hz of dark counts.

The limiting factor for the quality of the single photon retrieved from the quantum memory is the introduced technical noise, which affects its SNR. The main source of noise is the leakage of the memory control pulses, which couple to the photon mode. An angle of 3 degrees between the photon mode and the coupling beam minimizes the spatial overlap and noise introduced by directional, forward scattering. The noise is further removed with a home-built narrowband Fabry-Perot filter cavity of 43.4 dB suppression (at the control pulse frequency). The remaining noise is composed of light leaking through the filter, inelastically scattered control light at the photon frequency and the detectors' dark counts.

6.3 Results

In this section we study the single photon properties of the source photons which, further on, are used as the memory input photon. Secondly, we discuss performance of the memory, commenting on its tunability.

6.3.1 Photon generation

The HBT setup is used to characterize the photons generated by the source. Photon arrival times at each SNSPD are recorded together with trigger times for each experimental trial. We compute the second order autocorrelation function as:

$$g^{(2)}(k) = \frac{c_{1,2}(k)}{p_1 p_2}, \tag{6.1}$$

where p_1 (p_2) is the probability of detection per trial with SNSPD 1 (2) and $c_{1,2}(k)$ is the probability of a coincidence between detections separated by k trials ($k = 0$ means that detections are taken within the same trial). All the probabilities are calculated within a detection time window at fixed delay after each trial trigger. We

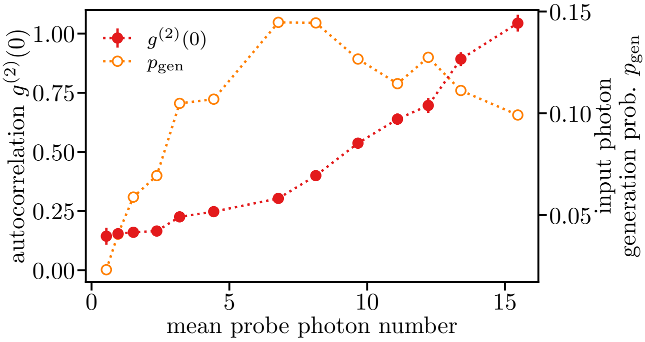

Figure 6.2: Dependence of $g^{(2)}(0)$ and p_{gen} on mean probe photon number. p_{gen} follows the Rabi cycle decreasing for the largest values of the probe power while $g^{(2)}(0)$ grows monotonically up to 1.

choose a 300 ns detection window which includes more than 95 % of the photon. For perfect single photons $g^{(2)}(0) = 0$. In practice, background noise or multi-photon components increase the $g^{(2)}(0)$. Emitted light remains non-classical for $g^{(2)}(0) < 1$ and $g^{(2)}(0) = 0.5$ marks the limit between single and multi-photon states.

In our source, we can change the emitted photon $g^{(2)}(0)$ within a range of 0.16 to 1 by varying the mean probe photon number, see fig. 6.2. For smaller probe photon number, the increase of $g^{(2)}(0)$ is accompanied by an increase of the photon generation probability p_{gen}, which is defined as $p_{\mathrm{gen}} = (p_1 + p_2)/\alpha$ where $\alpha = 0.21$ is the combined transmission and detection efficiency (of the source only - in this characterization we detected photons right after the source). However, for larger probe photon number p_{gen} decreases in accordance with the Rabi cycle. Yet, this is not accompanied by the $g^{(2)}(0)$ which continues to grow up to 1, indicating the presence of multiphoton components.

If not stated otherwise, for the following measurements, we fix $g^{(2)}(0) \approx 0.23$ and $p_{\mathrm{gen}} \approx 12$ %. The emitted photon has a steep leading edge followed by a slower exponential decay, with a full width at half maximum (FWHM) of the entire photon of $\sim$ 120 ns, see fig. 6.3 at time zero.

6.3.2 Photon storage

In this section, we demonstrate that the memory can efficiently store the generated single photon. It also offers tunability in the storage and retrieval process.

To characterize the memory performance, we first measure the temporal histogram of photon counts in 3 different situations, as shown in fig. 6.3 (left). We first detect the input single photon (orange histogram) when no storage attempt is performed, i.e. with no atoms in the memory but with control pulses. Then, a storage attempt is performed (red histogram) and one can see two peaks - the transmitted pulse, which is the part of the single input photon that is not absorbed in the storage attempt (counts in the 300 ns gray shaded window), and the stored pulse, which is

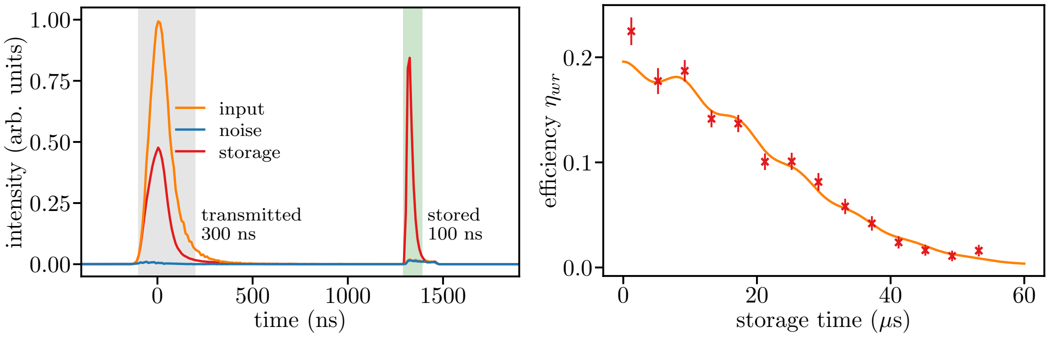

Figure 6.3: (left) Photon histogram observed at the SNSPDs after the memory. The orange histogram is the input photon alone with no storage attempt. The red histogram presents a storage attempt. The blue histogram shows the noise without input photon, but with the atoms in the memory. The gray shaded area is the detection window for the input and transmitted photon, and the green shaded area is the detection window for the stored photon (both windows include more than 95% of the respective waveforms). (right) The storage and retrieval efficiency as a function of storage time with the corresponding Gaussian fit e^{-t^2/τ^2}, where τ is the memory lifetime. The fit also includes an oscillatory term accounting for spin wave interference coming from residual population in $|5S_{1/2}, F = 2, m_F = 1\rangle$ (as an effect of imperfect Zeeman optical pumping) [209].

the excitation retrieved from a successful storage attempt (counts in the 100 ns green shaded window). Finally, we measure the noise (blue histogram) by blocking the input photon while keeping all the control pulses on and the atomic cloud present. This last measurement should contain all the information about the noise present in the experiment, in particular the noise introduced by the control pulses. We measure a corrected noise probability per trial at the output of the quantum memory, within the storage window, of $p_{\text{noise}} = 2.3(3) \times 10^{-4}$, which is derived from the detected noise probability as $p_{\text{noise}} = p^{\text{det}}_{\text{noise}}/\beta$, where $\beta = 0.34$ is the combined transmission and detection efficiency after the memory (at the photon frequency). To our knowledge, this value is among the lowest reported in ground state spin wave memories and is comparable to other quantum memories based on cold atoms or BECs [107, 200, 210–212]. We attribute this noise to the control pulse light leaking through the filter and scattering resulting from residual population on the storage transition. Four-wave mixing (FWM), which is an important source of noise in hot vapor memories, is not observed experimentally: The noise floor remains constant as a function of storage time, which would not be the case if FWM introduced additional spin waves. The control beam does not couple the atomic ground state $|g_m\rangle$ to any excited state, a necessary requirement for FWM to occur. Furthermore, the angle of 3° between control and photon mode is prohibitively large for the phase-matching condition to be satisfied [212].

The input and the noise histograms serve as a reference to calculate the storage and retrieval efficiency $\eta_{wr} = p_s/p_{\text{in}}$, where p_s and p_{in} are background-subtracted

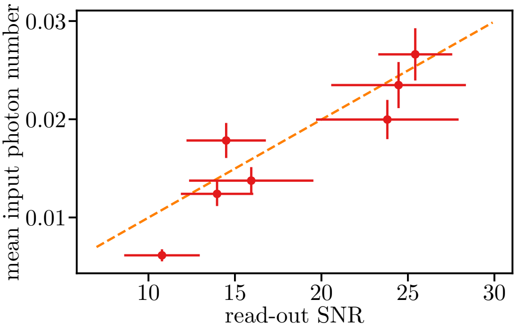

Figure 6.4: Mean number of single photons at the input of the memory as a function of the read-out SNR. Orange dashed line: linear fit that passes through zero. The slope of this line corresponds to μ_1.

probabilities of detecting a stored photon (within the 100 ns detection window) and an input photon (within the 300 ns detection window), respectively. We also calculate the write-in efficiency defined as $\eta_w = (p_{\mathrm{in}} - p_t)/p_{\mathrm{in}}$, where p_t is the background-subtracted detection probability of a transmitted photon (within the 300 ns detection window). From these two quantities, we infer the read-out efficiency $\eta_r = \eta_{wr}/\eta_w$. We obtain a maximum storage and retrieval efficiency $\eta_{wr} \approx 21\,\%$ at a storage time of 1.2 µs. For longer storage times, the motional decoherence and the decoherence due to the stray magnetic field gradients limits the efficiency with a characteristic $1/e$ decay time of 30 µs (see fig. 6.3(right)).

For the measurement shown in fig. 6.3 (left), the SNR of the retrieved photon is 24(4). For different input number of photons, we measure SNR of up to 26 (see fig. 6.4). An interesting figure of merit is the μ_1 parameter, defined as $\mu_1 = p_{\mathrm{noise}}/\eta_{wr}$, which expresses the input number of photons required to have SNR = 1 at the output. In our case, we find $\mu_1 = 1.00(7) \times 10^{-3}$ (see fig. 6.4), which is more than two orders of magnitude lower than similar ground state quantum memories based on warm atomic vapors [213–215], more than one order of magnitude lower than solid-state QMs based on rare-earth doped solids [201, 216] and similar to other quantum memories based on cold atoms [107, 200, 210–212].

Preservation of photon autocorrelation

A crucial requirement for a quantum memory is that it preserves the statistical properties of the stored photons. To show that our memory fulfills this criterion, we first adjust the mean probe photon number of the source to low values, resulting in a photon generation probability of $p_{\mathrm{gen}} \approx 3.0(3)\,\%$ (see fig. 6.2). With this setting, we expect the emitted photons to be strongly non-classical. To reduce the effect of experimental fluctuations, we collect data for 63 hours. We measure $g^{(2)}(0)$ of the input ($g^{(2)}(0) = 0.20(2)$), transmitted ($g^{(2)}(0) = 0.22(3)$) and stored photons ($g^{(2)}(0) = 0.34(7)$) and obtain values well below 0.5, see fig. 6.5. It shows that

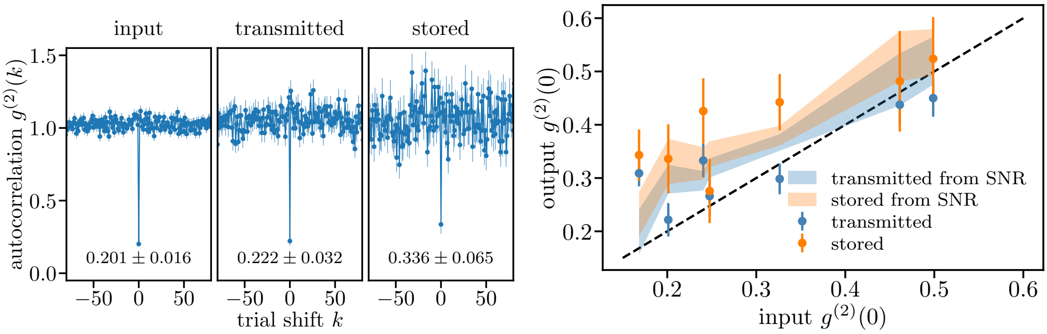

Figure 6.5: (left) Autocorrelation $g^{(2)}$ as a function of shift between trials k for the input, transmitted and stored photons. For trials separated by a shift $k \geq 1$ the clicks are uncorrelated, yielding $g^{(2)}(k) = 1$. Coincidences clicks in the same trial, $k = 0$, are much less frequent asserting the photons anti-bunching. (right) Output $g^{(2)}(0)$ of the transmitted and the stored photons as a function of the input $g^{(2)}(0)$. Dashed black line: autocorrelation after the memory equals input. Shaded areas: autocorrelation for transmitted and stored photon as expected from the model, taking into account uncertainty in $g^{(2)}_{\text{in}}(0)$ and SNR (see sec. 4.1.2).

the memory preserves the single photon nature of the input photon. One can see, however, that $g^{(2)}(0)$ of the stored photon is significantly larger than the $g^{(2)}(0)$ of the input photon. We expect that the main source of degradation of $g^{(2)}(0)$ is the uncorrelated noise introduced by the memory control pulses. We developed a simple model, discussed in sec. 4.1.2, to quantify the effect of uncorrelated noise on $g^{(2)}(0)$. The model predicts a $g^{(2)}_{m}(0) = 0.33(4)$ for stored photon taking into account a measured SNR of 11(2) and the measured input $g^{(2)}(0)$. For this data set, the model is in agreement with the measured data, within the error bars. We also performed several other measurements (with integration times of around 10 to 16 hours per data point) for different input $g^{(2)}(0)$. While the model reproduces qualitatively the trend, as one can see in fig. 6.5 (right), there is a large point to point fluctuation that we attribute to low statistics and experimental fluctuations.

Spectral properties

Our memory offers significant tunability in the write-in process that may prove useful in future hybrid quantum networks [217]. We start by showing that the memory can adapt to the input photon frequency. For that, we set the input photon detuning to $\delta = -52\,\text{MHz}$ and we vary the frequency of the control beam pulse. The maximum efficiency is observed for the two-photon resonance, see fig. 6.6 (left), achieving optimum storage conditions for the input photon.

The width of the curve depends on the spectral properties of the input photon. Bandwidth-limited photons (i.e. photons that exhibit the minimum bandwidth for a given temporal duration) are desirable because one can achieve with them a high

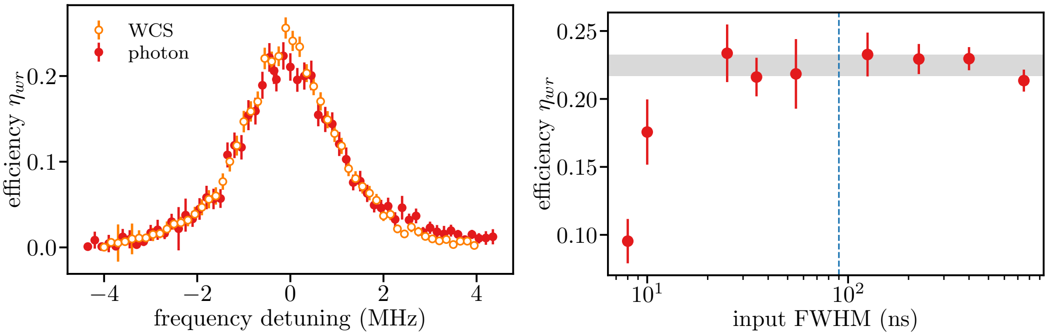

Figure 6.6: (left) Storage and retrieval efficiency versus frequency detuning of the control write-in pulse for the single photon input (red) and WCS (orange). The frequency detuning is measured from the two-photon resonance of the input photon and the write-in control beam. (right) Storage and retrieval efficiency η_{wr} as a function of the temporal duration (FWHM) of WCS input pulses with Gaussian shape. The gray horizontal shaded area represents the mean (0.225) and standard deviation (0.008) of the efficiency for input pulse durations above 25 ns. Only for pulse durations below 25 ns, corresponding to a bandwidth of about ≈17.6 MHz (assuming transform-limited Gaussian pulses), the storage and retrieval efficiency drops. We attribute this drop to limited control power and finite AOM rise time, resulting in a smaller pulse area. The blue dashed vertical line represents the minimum duration of the single photon generated by the Rydberg-based source (∼90 ns FWHM). For each data point, write-in control pulse power, shape and delay are optimized.

Hong-Ou-Mandel interference visibility over the whole duration of the pulse [218, 219]. Using the whole duration of the pulse would result in higher entanglement distribution rates. Therefore, in order to benchmark the spectral properties of the input photon, we repeat the measurement with a weak coherent state (WCS) with the same waveshape, center frequency and mean number of photons. This WCS is derived from a laser exhibiting a linewidth much smaller than the bandwidth of the pulse. As can be seen in fig. 6.6 (left), both spectra overlap very well, suggesting that the input photon is close to bandwidth-limited.

Using classical light pulses, we also performed storage at detunings $\delta = -32$ MHz and $\delta = -72$ MHz (not shown here). For these values, no significant change of storage and retrieval efficiency was observed, suggesting that the input photon detuning can be varied within this range. Eventually, the detuning will be limited by the proximity to other atomic levels.

We also study the bandwidth of our memory by sending WCS of different durations (with FWHM of 8 to 800 ns). We show the results in fig. 6.6 (right), asserting that the memory can accommodate pulses of very different lengths without changing its efficiency.

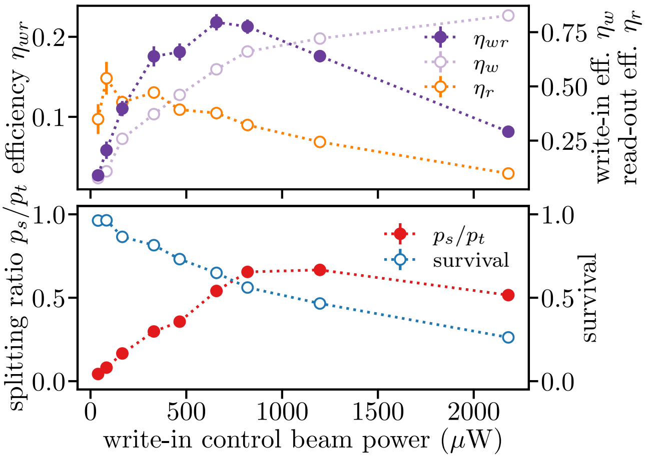

Figure 6.7: Storage efficiencies, survival probability and splitting ratio as a function of the write-in control beam power.

Tunable beam-splitter

Another interesting feature of the memory is that one can control how much of the input photon is absorbed and how much is transmitted. By varying the write-in control beam power, one can change η_w as shown in fig. 6.7 (top). This changes effectively the splitting ratio p_s/p_t between the stored and the transmitted photon pulse. Our memory can therefore be used as a temporal beam splitter [220] with a tunable splitting ratio, which may have applications in the quantum repeater architecture mentioned in the introduction [12]. Substituting the BS + QM with only the QM and guiding the transmitted light directly to the intermediate station, relaxes the requirements for storage efficiencies to approach unity. To investigate this possibility, we plot p_s/p_t, see fig. 6.7 (bottom). It peaks for intermediate values of the write-in control beam powers and decays for higher values. This stands in contrast with the monotonically growing η_w and is a result of η_r decreasing with the control power. We attribute this behavior of η_r to the asymmetrical distribution of the spin wave in the ensemble, when large write-in control powers are used [98, 208]. With increasing write power, the spin wave starts having more asymmetric shape, being mostly created at the beginning of the ensemble. This effect is known to limit the retrieval efficiency, especially in the forward retrieval configuration [221–223].

In fig. 6.7 (bottom), we also plot the survival efficiency $(p_s{+}p_t)/p_{\text{in}}$, the normalized probability of detecting a transmitted or stored photon per trial. We observe that it decreases with increasing control power due to the decrease of the read-out efficiency. With current conditions, the tunability range of p_s/p_t is limited, but we expect that backward retrieval should considerably improve the read-out efficiency at high write power, which will increase the survival probability [98]. As a first application of the single photon temporal beam splitter, we used the two temporal output modes of the memory to measure the antibunching parameter. For the measurement presented in

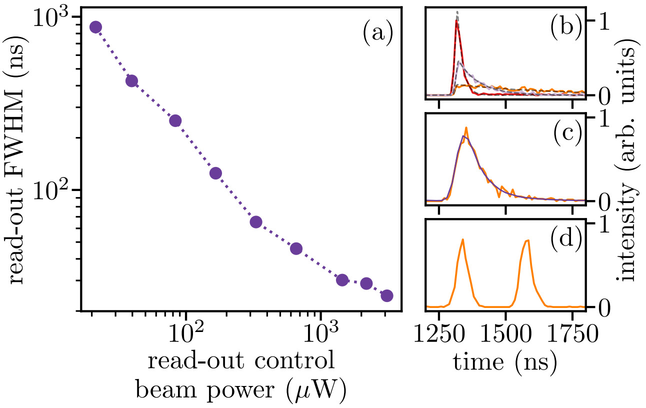

Figure 6.8: Stored photon waveshape tunability. (a) Dependence of the stored photon duration on the read-out control beam power. (b) Selected waveshapes of the stored photons from (a) and their corresponding fits. (c) Stored photon waveshape (solid orange) matching exactly the input photon waveshape (dashed blue). (d) Stored photon shaped as a time-bin qubit.

fig. 6.5, we obtain a $g^{(2)}(0) = 0.28(2)$ with a significantly increased count rate with respect to the case where we split each output mode with a standard BS.

Photon shaping

Our memory also offers shape tunability of the stored photon [224]. In particular, one can retrieve photons with very different lengths (with FWHM of 25 to 900 ns) by changing the read-out control beam power, see fig. 6.8(a, b). We read out the memory with a square-shaped pulse resulting in a steep leading edge of the retrieved photon and slower decaying trailing edge. We fit the former with a Gaussian function and the latter with an exponential and obtain the total FWHM of the photon. One can also use more complex waveforms for the read-out control pulse to shape the read-out photon, e.g. reproducing the input photon or a time-bin qubit, see fig. 6.8(c, d). This capability would allow for matching differently shaped photons emitted by different sources. We do not observe significant reduction of η_{wr} for different read-out pulse shapes, in agreement with theory [225].

6.4 Conclusions

We demonstrated storage and retrieval of an on-demand single photon generated in one Rydberg-based atomic ensemble in another cold atomic ensemble through a Raman memory protocol. We achieved a 21 % memory efficiency and a signal-to-noise ratio up to 26 for the retrieved photon, leading to μ_1 of $1.00(7) \times 10^{-3}$. This allowed us to observe only a moderate degradation of the single photon statistics. We showed the adaptability of our memory in frequency and bandwidth. Moreover, we evaluated the performances of the built-in temporal beam splitter offered by the Raman memory. Lastly, we showed that we can shape the temporal waveform of the retrieved photon by shaping the read-out pulse power and waveform. These results are a step forward in the implementation of efficient quantum-repeater links using single-photon sources. In that context, one interesting advantage of having the source and the memory residing in different ensembles is that they can be optimized independently. This allows for an efficient single-photon generation and storage and facilitates the use of multiplexed quantum memories [226, 227], which would significantly improve repeater entanglement generation rates.

Several improvements should be applied to our experiment before it can become a practical alternative. The generation efficiency of the single photon from the Rydberg ensemble could be increased by increasing the OD of the ensemble and/or by embedding the ensemble in a low finesse cavity [70]. The quality of the single photon (as measured by the autocorrelation function $g^{(2)}(0)$) could also be improved by addressing a slightly smaller ensemble and by reaching a higher principal quantum number level to increase the Rydberg blockade radius, as was shown in [62], where $g^{(2)}(0)$ values smaller than 10^{-3} have been measured. Regarding the Raman quantum memory, higher storage and retrieval efficiencies could also be reached by increasing the OD of the ensemble [107] and using backward retrieval [222], or with an impedance matched cavity. Backward retrieval will also improve the survival probability and the performances of the temporal beam-splitter. Finally, longer storage time up to 1 s could be achieved by using magnetic insensitive transitions and by loading the ensemble into an optical lattice to suppress motional induced dephasing [228].

Chapter 7

Strongly nonlinear interaction between non-classical light and a blockaded Rydberg atomic ensemble

This chapter describes another experiment that involved collaboration of two distinct setups. I was responsible for the Rydberg setup, which served as the nonlinear medium, while my colleague, Lukas Heller, operated another cold-atomic setup used as a non-classical light source. The data was collected with a help of two post-docs, Félix Hoffet and Auxiliadora Padrón-Brito. Our experimental results have been published in [229], and the content of this chapter is based on that publication. All the figures presented in this chapter are taken directly from this publication.

7.1 Motivation

The promise of dipole blockaded ensembles for quantum information processing purposes is clear. However, so far, all proof-of-concept demonstrations with blockaded ensembles have used classical weak coherent states (WCS) as inputs, although there are records of single photons being stored in Rydberg ensembles with weaker nonlinearity [51, 116]. Nevertheless, for applications in quantum networks it is crucial to demonstrate that single photons can interact with a blockaded ensemble with single-photon nonlinearity. For example, a photon-photon gate between two single photons that are part of an entangled state would allow deterministic Bell state measurements and entanglement swapping, important capabilities for scaling up quantum networks. Using single photons as inputs have also been predicted to improve the contrast of single photon transistors [52].

As a step towards these applications, we report the first experimental demonstration of the interaction and storage of a correlated single photon in a highly

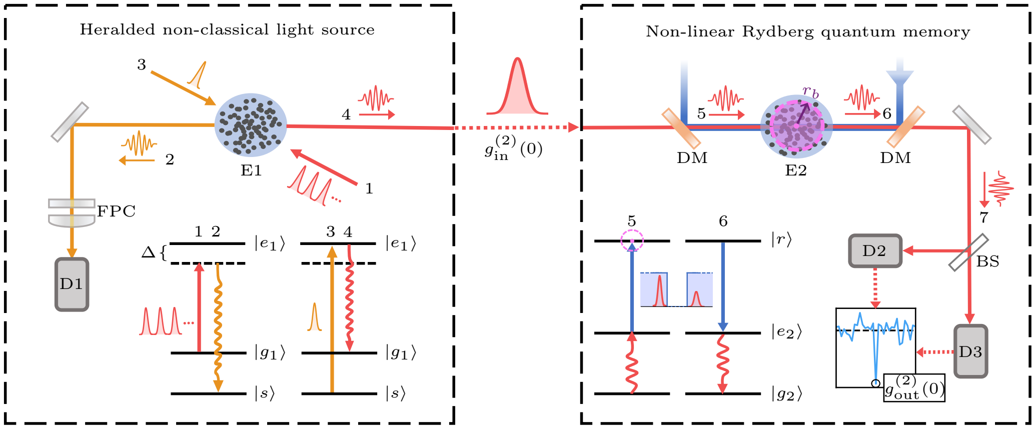

Figure 7.1: Schematic view of the experiment. A train of write pulses detuned by $\Delta/2\pi = -40\,\text{MHz}$ from the $|g\rangle \to |e\rangle$ transition is sent to E1 (step 1) until a Raman scattered photon is detected on detector D1 (step 2), heralding a collective excitation in E1. This spin-wave is then read out by a strong read pulse resonant with $|s\rangle \to |e_1\rangle$ (step 3), which produces the emission of a read photonic field in a well-defined mode (step 4). Using the nonlinearity of the dipole blockade effect, this field is then mapped to a single Rydberg excitation in E2 by means of Rydberg-EIT driven by a coupling beam (step 5). At a later time, the excitation is read out by reapplying the coupling beam (step 6) and the statistics of the field are studied in a HBT setup consisting of one beam splitter and two detectors (step 7). D1(2,3) : Single-photon detector 1(2,3); E1(2): Atomic ensemble 1(2); DM: Dichroic mirror; BS: Beam-splitter; FPC: Fabry-Perot cavity; r_b: dipole blockade radius ($\sim 10.5\,\mu\text{m}$).

nonlinear medium based on cold Rydberg atoms. We use the DLCZ protocol [11] in a cold-atomic ensemble to generate heralded non-classical states of light with a tunable multiphoton component. Those photons are then guided to another ensemble and stored in a highly excited Rydberg state using dynamical electromagnetically induced transparency (rEIT) [104, 110]. We assert the single-photon-level nonlinearity of our system by comparing autocorrelation functions $g^{(2)}(0)$ of the input and output photons, showing the first realization of single photon filtering with non-classical input states. Additionally, we demonstrate that the nonlinearity depends only on the input Fock-state distribution of the optical field.

7.2 Experimental setup

Our experimental setup consists of two ensembles of cold ^{87}Rb atoms located in the same laboratory and connected via 10 m of optical fiber cable (see fig. 7.1). The first ensemble (E1) is used to generate heralded non-classical light using the DLCZ protocol. The second ensemble (E2) is used as a nonlinear Rydberg EIT quantum memory with which the DLCZ light interacts.

7.2.1 Experimental protocol

We start by sending a train of write pulses to E1, detuned by $\Delta = -40\,\mathrm{MHz}$ from the $|g_1\rangle = |5S_{1/2}, F = 2, m_F = +2\rangle$ to $|e_1\rangle = |5P_{3/2}, F = 2, m_F = +1\rangle$ transition. With a low probability, this generates a write photon in the heralding mode which, upon detection at detector D1, heralds a collective spin excitation (spin wave) in the spin state $|s\rangle = |5S_{1/2}, F = 1, m_F = 0\rangle$. To reduce the heralding noise, we filter unwanted frequencies with a Fabry-Perot cavity in the write mode. In total, the transmission of a write photon in our setup (including its detection) is 21 %. After 1.6 µs, we then send a read pulse resonant with the $|s\rangle \rightarrow |e\rangle$ transition that maps the collective excitation into a read photon. This photon is resonant with the $|g\rangle \rightarrow |e\rangle$ transition and is emitted into a well-defined mode that depends on the phase matching conditions of the process. It is then collected in an optical fiber and sent to the nonlinear Rydberg medium. The atomic parametric interaction used in the DLCZ process creates photon pairs in a two-mode squeezed state [11, 230]. By changing the write pulse intensity, we vary the probability of creating (p) and detecting a write photon (p_w), and therefore we can tune the multiphoton probability in the read field.

The read photons are then frequency-shifted by an acousto-optical modulator (AOM) to match the $|g_2\rangle = |5S_{1/2}, F = 2\rangle \rightarrow |e_2\rangle = |5P_{3/2}, F = 3\rangle$ transition in E2. They are directed to the Rydberg medium, where they propagate under EIT conditions. The EIT coupling field is counter-propagating and resonant with the $|e_2\rangle \rightarrow |r\rangle = |90S_{1/2}\rangle$ transition. The photons propagate as Rydberg polaritons strongly interacting through van der Waals interactions, which prevent multiple Rydberg excitations in the cloud [32]. Since only one excitation can exist in the cloud at a time, only one photon can be retrieved. As a consequence, the medium response is nonlinear and the statistics of the photonic pulses are affected. Additionally, when the Rydberg polariton is propagating in the cloud, we can switch off the coupling field, freezing the polariton's propagation and effectively performing storage. This is known to enhance the nonlinearity [78, 80]. Finally, the retrieved photons are detected using single-photon detectors (D2 and D3) and their statistics are measured in a Hanbury Brown-Twiss (HBT) setup.

7.2.2 Heralded photon source

For the DLCZ source to generate photons efficiently, its optical depth (OD) must be large [18] and the coherence time of the collective spin excitation must be longer than the time between the write and the read pulse. We achieve both using standard techniques of magneto-optical trapping (MOT) assisted by a single retro-reflected beam dipole trap at 797 nm. We obtain a cloud with OD = 6 and an initial temperature of $\sim 80\,\mu\mathrm{K}$, cold enough to suppress effects of motional dephasing. However, in each trial the ground state population is swapped back and forth between $|g_1\rangle$ and $|s\rangle$ (an intrinsic property of the DLCZ protocol) effectively heating up the cloud and resulting in a short dipole-trap trapping time of the order of a few ms, much shorter than the Rydberg one.

7.2.3 Nonlinear medium

To maximize the nonlinearity of the Rydberg medium, one needs large OD in a small ensemble [26]. The characteristic length is given by the dipole blockade radius r_b – radius of a sphere around an atom excited to the Rydberg level where, due to the dipole-dipole interactions, no other atom can be excited to the Rydberg state [32]. In our case, for $n = 90$, $r_b \approx 10.5\,\mu\mathrm{m}$ [26, 86]. To achieve such a regime, we first trap our atoms in a MOT using similar techniques as in E1 and then transfer them into a small crossed dipole trap at 852 nm. In this way, we obtain a spherical cloud with OD = 11, diameter of 15 µm (FWHM) and temperature of $\sim 40\,\mu\mathrm{K}$. The EIT transparency is limited to about 60 % due to a large dephasing rate of the $|e_r\rangle \rightarrow |r\rangle$ transition, attributed to stray RF fields and motional dephasing. To avoid additional dephasing we lock the lasers to a home-build reference cavity, allowing for linewidth reduction and long-term stability, see sec. 3.3.

Because of the different trapping cycles of the two ensembles (12 ms for E1 vs 1.3 s for E2), the overall duty cycle of the experiment is limited to 5 %. Besides, passive losses affect quadratically the coincidence probability in the HBT experiment. Both factors result in long interrogation times, which makes this experiment challenging, as high stability is required for long periods of time.

7.3 Results

We now discuss our results. We start by characterizing our heralded non-classical light source. The read photons statistics can be changed by varying the write pulse intensity during the excitation stage of the DLCZ protocol (step 1 in Fig. 7.1). By increasing the write pulse intensity, and consequently increasing the probability of detecting a write photon p_w, we can tune the heralded autocorrelation $g^{(2)}_{\mathrm{in}}(0)$ of the read photons from 0.1 to 1.4, allowing us to study the response of the Rydberg medium to light with different input statistics.

The heralded DLCZ states are stored in the Rydberg medium and their storage and retrieval efficiency is measured as a function of p_w, as shown in fig. 7.2(top). For low p_w values, the efficiency is around 20 %. As p_w increases, thereby enlarging the multiphoton contribution in the heralded input field, we observe a pronounced reduction in efficiency. This behavior is consistent with the effects of the dipole blockade, which turns higher-order Fock states into one-photon states. Such dynamics have previously been reported for weak coherent states during slow-light propagation [58, 61] or storage [174] under rEIT conditions. Notably, this result marks a first demonstration of non-classical light pulse storage within a strongly nonlinear Rydberg medium.

We turn our attention to $g^{(2)}(0)$, as it is a vital metric for achieving high fidelity entanglement in quantum networks [199]. After the interaction of the DLCZ-emitted

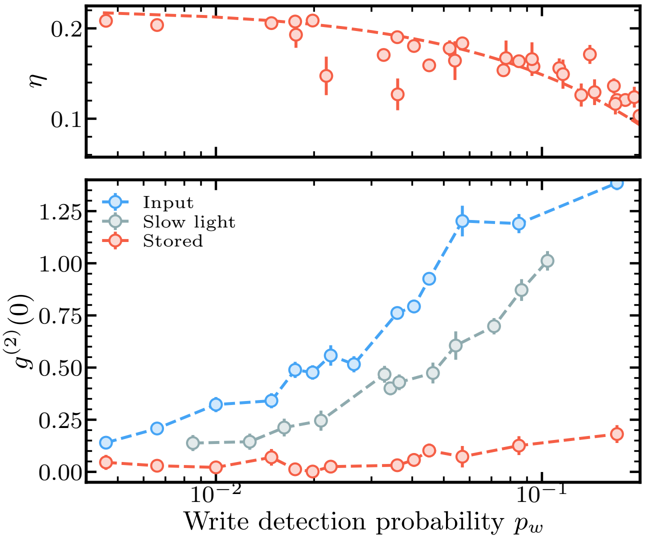

Figure 7.2: (top) Decay of the heralded single-photon storage and retrieval efficiency η as a function of detected write probability p_w. The dashed line is a guide to the eye. (bottom) Autocorrelation $g^{(2)}(0)$ of the input (blue), propagating under rEIT conditions (green), and stored (red) DLCZ read photons for different values of p_w. Values of $g^{(2)}(0)$ are obtained by integrating coincidences over the full pulse. We observe a strong reduction of the DLCZ read photons $g^{(2)}(0)$ after their storage – a clear manifestation of the strong nonlinearity of our Rydberg medium. $g^{(2)}_{\text{out}}(0)$ of pulses propagating without storage is only lowered with respect to the input due to their duration larger than the group delay (150 ns vs. $\sim$ 85 ns) and complex dynamics of propagation of such short pulses [77, 78]. This data was corrected for background noise induced by the blue coupling light and dark counts of the detectors (see sec. 4.1.3). The correction lowers the $g^{(2)}(0)$ values by ≤ 0.06.

light with our nonlinear medium, we observe a pronounced suppression of the $g^{(2)}(0)$ value, as seen in fig. 7.2(bottom), another clear indicator of the nonlinear interaction taking place. Specifically, the $g^{(2)}(0)$ for slow light experiences only a slight reduction, attributed to the pulse not being fully compressed within one blockade radius. The propagation time through the medium is around 85 ns, while the pulses are 150 ns long (FWHM). It means that the nonlinearity affects only a part of a pulse at a time, what effectively decreases the strength of the nonlinearity. The $g^{(2)}_{\text{out}}(0)$ for stored light, on the other hand, stays low for increasing value of p_w and input $g^{(2)}_{\text{in}}(0)$. This is a clear sign of nonlinearity enhancement due to storage, as previously observed in [80]. These measurements are the first observation of a $g^{(2)}(0)$ reduction and single photon filtering with a non-classical input for any kind of system.

As one can see in fig. 7.2, our $g^{(2)}_{\text{out}}(0)$ does not reach zero and rises as p_w increases, implying that the ensemble might not be under full blockade. To explain the observed trend, we develop a simple Monte Carlo simulation accounting for the influence of an imperfect blockade on different Fock states.

However, before explaining the details of our simulation, we have to introduce the concept of multiphoton strength ζ. As we later discuss, not only do we validate our model with the collected $g^{(2)}_{\mathrm{out}}(0)$ data for DLCZ photons, but we also study the response of our medium with input coherent states. The multiphoton strength ζ facilitates the representation of the results for both data sets on a single plot.

7.3.1 Estimation of multiphoton strength ζ

For a Fock state distribution of the incoming state

$$p_k = \langle k| \hat{\rho}_{\mathrm{in}} |k\rangle , \tag{7.1}$$

where $\hat{\rho}_{\mathrm{in}}$ is the incoming state and $|k\rangle$ is k-photon Fock state, the multiphoton strength ζ is defined as the probability of having two or more photons in a pulse normalized to the probability of having at least one photon:

$$\zeta = \frac{\sum_{k\geq 2} p_k}{\sum_{k\geq 1} p_k}. \tag{7.2}$$

This choice is motivated by the fact that multiphoton components adversely impact the performance of quantum networks. In contrast, the mean photon number provides limited insights into the underlying Fock state distribution, making multiphoton strength a more informative metric.

We now explain how we estimate the input pulse Fock state distribution and describe the effect of different optical elements on this distribution.

Transfer matrix formalism

Any element affecting Fock state distribution, let say a beam splitter or transmission losses, can be described by a matrix M, such that the distribution after this element can be expressed as

$$p'_k = M_{kl} p_l, \tag{7.3}$$

where M_{kl} are elements of the matrix and the summation over the repeating indices is implicit. For this matrix to preserve the normalization of the Fock state distribution, i.e. $\sum_k p'_k = 1$, it's necessary that its columns sum up to 1.

Virtually any element can be expressed as such a matrix. A typical example would be a beam splitter or any other lossy element with transmission t. If we aim to determine the Fock state distribution after this element, the matrix elements for this operation are described by the binomial probability mass function:

$$M_{kl} = \binom{l}{k} t^k (1-t)^{l-k}. \tag{7.4}$$

Consider another example: a perfect single-photon filter, such as a Rydberg ensemble that's both perfectly blockaded and perfectly transmissive. This filter transforms all higher order Fock components into 1-photon component. The matrix representation for such a filter would be:

$$M = \begin{pmatrix} 1 & 0 & 0 & 0 & \cdots \\ 0 & 1 & 1 & 1 & \cdots \\ 0 & 0 & 0 & 0 & \cdots \\ \vdots & \vdots & \vdots & \vdots & \ddots \end{pmatrix}. \tag{7.5}$$

Generally, lossy operations are represented by upper triangular matrices. However, if one were to model elements adding photons, such as detector dark counts, using this approach, the matrix would exclusively have elements in the lower triangle. A nice bonus of this formalism is how straightforward it is to back-propagate any operation just by inverting its matrix representation (provided that the matrix is not singular).

Knowing how we can easily account for transmission losses in our system, we can estimate what is the Fock state distribution at the input of the Rydberg cloud.

Coherent state

Determining the Fock state distribution for a coherent state is a straightforward task because it follows the Poisson distribution. Moreover, any linear element retains this characteristic. Therefore, for a coherent state, the Fock state distribution is expressed as

$$p_k = e^{-|\alpha|^2} \frac{|\alpha|^{2k}}{k!}, \tag{7.6}$$

where $|\alpha|^2 = \mu_{\text{in}}$, with μ_{in} being the mean input photon number, derived from the back-propagation of loss from the detection probabilities at single-photon detectors. Finally, one obtains multiphoton strength ζ using eq. 7.2.

DLCZ single photons

Determining the Fock state distribution for the DLCZ read photon at the Rydberg ensemble's input is more complex. We start by considering that the DLCZ produces a two-mode squeezed state for the write and read photons

$$|\Psi_{w,r}\rangle = \sqrt{1-p} \sum_{n=0}^{\infty} p^{n/2} |n_w, n_r\rangle, \tag{7.7}$$

with p being the probability that at least one excitation is generated. We are interested in the Fock state distribution in the read mode, conditioned on a prior detection in the write mode. We model the detection of a write photon by the following POVM operator, which takes into account transmission and detection efficiencies (t_w) and models non-photon-number-resolving detection:

$$\hat{\Pi}_{\text{det}} = \sum_{n=1}^{\infty} [1 - (1 - t_w)^n] |n_w\rangle \langle n_w|. \tag{7.8}$$

The resulting conditional density matrix for the read-mode $\hat{\rho}_{r|w}$ can be written as:

$$\begin{aligned}\hat{\rho}_{r|w} =& \frac{\mathrm{Tr}_w\left[\hat{\Pi}_{\mathrm{det}}\hat{\rho}_{w,r}\right]}{\mathrm{Tr}_{w,r}\left[\hat{\Pi}_{\mathrm{det}}\hat{\rho}_{w,r}\right]}\\ =&(1-p)t_w^{-1}\left[1-p(1-t_w)\right]\\ &\times\sum_{n=1}^{\infty}p^{n-1}\left[1-(1-t_w)^n\right]\left|n_r\right\rangle\left\langle n_r\right|,\end{aligned} \tag{7.9}$$

where $\hat{\rho}_{w,r} = \left|\Psi_{w,r}\right\rangle\left\langle\Psi_{w,r}\right|$. We can identify $\hat{\rho}_{w,r}$ with $\hat{\rho}_{\mathrm{in}}$ from eq. 7.1 and use the above-described transfer matrix formalism to account for the losses between the setups $t_r = T\eta_a = 0.15$, with T being the transmission factor between the two experiments and η_a being the DLCZ read-out efficiency. The remaining task to determine multiphoton strength is to figure out the value of p in eq. 7.7.

Due to losses between the generation of DLCZ photons and their detection, it would be difficult to directly measure their Fock state distribution and infer p[1]. Instead, we estimate it from the auto-correlation function $g^{(2)}(0)$, which is independent of linear losses and is bijective for given losses t_r. To obtain p, we find a probability distribution $p_k = \left\langle k\right|\hat{\rho}_{r|w}\left|k\right\rangle$ that yields given $g^{(2)}(0)$. A general formula for the auto-correlation function $g^{(2)}(0)$ of an arbitrary state is

$$g^{(2)}(0) = \frac{\langle a^\dagger a^\dagger a a\rangle}{\langle a^\dagger a\rangle^2} = \frac{\sum\limits_{k=0}^{\infty}k(k-1)p_k}{\left[\sum\limits_{k=0}^{\infty}kp_k\right]^2}. \tag{7.10}$$

Then, from p, we can infer the input Fock state distribution and the corresponding multiphoton strength ζ.

Having explained how to estimate the Fock state distribution at the input of the nonlinear medium, we can now describe our method to simulate the effect of the partial dipole blockade on this distribution.

7.3.2 Monte Carlo simulation of the partial blockade

In our numerical simulation, we simplify the problem to one dimension. This choice is motivated by the directionality of polariton propagation and the small transverse extent of the probe mode. We also assume the ensemble has a uniform density distribution over its length, determined by the cloud's FWHM. Additionally, we model the dipole blockade as a binary effect: if two polaritons are closer than the

---

[1] Alternatively, one could infer the generated two-mode squeezed state eq. 7.7 based on the measured p_w, but this would require very careful calibration of losses in the write path, which, from our experience, can be challenging.

blockade radius, the later-arriving one gets scattered; otherwise, both propagate without losses. This approximation is referred to as the hard-sphere model [111, 171].

It's important to note that this is an effective model, and some physical aspects of the problem are not addressed. Specifically, the binary blockade is a good approximation only in ensembles with a very high optical depth [61, 171]. However, by storing the photons, we amplify the nonlinearity [80] – any photon not stored as a polariton, even if unscattered, is essentially filtered in time by the storage process. We also overlook the dephasing interactions between polaritons during storage [172], which can be viewed as another nonlinearity booster. As mentioned later, both of these factors might be the reason why the model's blockade radius matches so closely with what's expected from the usual formula for blockade radius [26]. It would be worthwhile to vary the storage time and see if this affects the determined blockade radius. Additionally, we do not account for more nuanced effects that especially arise at high multiphoton strengths, such as dissipative interactions [171] and pollutants [61]. Both are likely to elevate the measured $g^{(2)}(0)$ by diminishing the $g^{(2)}(0)$ expression's denominator. Though, we observe pollutant effects only when ζ is near 1. Overall, our simulation should be seen as a tool that offers an intuition of how the medium modifies the Fock state distribution of stored pulses.

In our simulation, we start by randomly selecting a number of positions within the cloud corresponding to the number of a specific input Fock state. Sequentially analyzing these positions, we determine the probability of polariton presence at each spot by considering the blockade effect. To clarify, there may be scenarios where the third polariton survives without being lost, even if it's located closer than the blockade radius to the second one. This can happen if the second polariton was previously scattered by the first. We repeat this process 1×10^5 times for each Fock state to determine the probability distribution of survival and conversion into other Fock states. The derived distributions are then integrated as columns in a transfer matrix, capturing the influence of (partial) blockade on the input Fock state distribution.

To determine the Fock state distribution after the storage in the Rydberg ensemble, we utilize the transfer matrix formalism described earlier. For DLCZ photons, we begin with eq. 7.9 as the input state and compute its Fock state distribution. Subsequently, this is modified by matrices that factor in transmission losses between setups ($t_{\text{losses}} = 0.15$), the fact that the input pulse cannot be fully compressed within the medium (resulting in a part only of the pulse being effectively stored which we model as a beam slitting operation, $\eta_{\text{compression}} = 0.6$), and half the linear losses during EIT propagation $(\sqrt{\eta_{\text{EIT}}} = \sqrt{0.6})$[2]. Estimating the second factor is somewhat challenging due to complex propagation dynamics of such short pulses under rEIT conditions [77, 78]. Nonetheless, the precise value influences our simulation results only weakly, evident in fig. 7.3 where the limits of the shaded area correspond to

---

[2] The remaining linear losses during EIT propagation do not affect the measured $g^{(2)}(0)$, however, they need to be included in the calculation of the storage and retrieval efficiency, as it is shown in the next section.

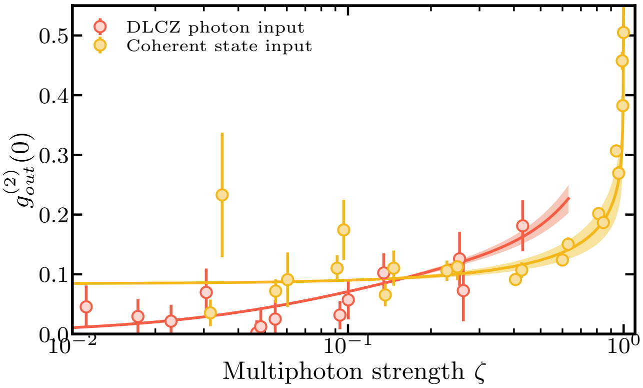

Figure 7.3: Autocorrelation $g^{(2)}_{\mathrm{out}}(0)$ of DLCZ read photons (red circles) and coherent states (yellow circles) after their storage in the nonlinear medium, for different values of multi-photon strength ζ of the input state. The solid lines in the corresponding colors represent the Monte Carlo simulation results discussed in the main text. The shaded area corresponds to uncertainty of estimating losses before the storage.

$\eta_{\mathrm{compression}}$ being 0.45 and 0.75. Finally, the matrix derived from the Monte Carlo simulation is used to account for the blockade effect.

This procedure can be concisely represented by:

$$p' = M^{\mathrm{blockade}}\, M^{\sqrt{\mathrm{EIT}}}\, M^{\mathrm{compression}}\, M^{\mathrm{losses}}\, p\ , \tag{7.11}$$

where elements of p are $p_k = \langle k|\, \hat{\rho}_{r|w}\, |k\rangle$ with $\hat{\rho}_{r|w}$ as per eq. 7.9. The matrices, M, are defined as outlined above.

In the case of coherent states, we don't need to account for the transmission losses, because by backpropagation we calculate directly the state right before the cloud.

Simulation results

The model replicates well the observed $g^{(2)}_{\mathrm{out}}(0)$ data for both DLCZ photons and WCS, as shown in fig. 7.3, where we set the blockade radius to $r_b = 10.5\,\mu\mathrm{m}$, aligning with the value calculated for our experimental parameters [26]. While the blockade radius traditionally pertains to rEIT conditions without storage, and the hard-sphere model suits very high OD regime [61, 171], we attribute the agreement between the data and the simulation to storage enhancing the medium nonlinearity, akin to an OD boost [80].

Using our simulation, we can explain the distinct $g^{(2)}_{\mathrm{out}}(0)$ patterns observed for DLCZ photons and WCS. In most cases, 2-photon state is converted into 1-photon state, but occasionally the imperfect blockade allows for its survival. Higher order components get transformed into either 1- or 2-photon states, with the 2-photon conversion probability rising with k. At low ζ, $g^{(2)}_{\mathrm{out}}(0)$ values primarily reflect the

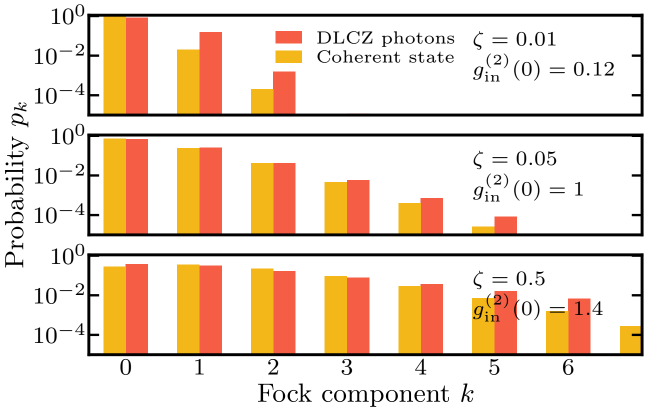

Figure 7.4: Simulated input Fock state distribution of DLCZ read photon and coherent state for the same values of ζ. We plot it for $\zeta = \{0.01, 0.05, 0.5\}$, corresponding to $g^{(2)}_{\rm in}(0) = \{0.12, 1, 1.4\}$ of the DLCZ generated light field. Coherent states have always $g^{(2)}_{\rm in}(0) = 1$ whatever the ζ value. The transmission losses are included in the computation of the Fock state distributions.

amplitude of 2-photon states, meaning $g^{(2)}_{\rm out}(0) \approx 2\,p_2/(p_1)^2$. For WCS, since the input $g^{(2)}_{\rm in}(0) = 1$ at any ζ, post-storage $g^{(2)}_{\rm out}(0)$ remains flat at lower ζ values, determined by the 2-photon state's survival probability. However, as ζ grows, higher-order components emerge, leading to an increase in $g^{(2)}_{\rm out}(0)$. Conversely, DLCZ photons show an increasing $g^{(2)}_{\rm in}(0)$ trend with ζ. After storage, the trend persists, but the values diminish due to the blockade. The stored DLCZ photon $g^{(2)}_{\rm out}(0)$ intersects the stored WCS $g^{(2)}_{\rm out}(0)$ when the input DLCZ photons have $g^{(2)}_{\rm in}(0) \approx 1$.

It's worth noting that due to the ensemble being only partially blockaded, the nonlinearity becomes sensitive to the shape of the input Fock state distribution. This is precisely why the $g^{(2)}_{\rm out}(0)$ of DLCZ photons raises more rapidly than that of WCS – the tail of the DLCZ Fock state distribution is longer than of WCS at larger values of ζ, as one can see in fig. 7.4.

This simulation can also be employed to mimic results from slow-light propagation without storage. To adjust for pulses that cannot be entirely compressed within the medium, one might consider expanding the medium size to align with the pulse length. Yet, to align with the experimentally observed results, when using the blockade radius extracted from storage data, the medium needs to be more than twice as large as above reasoning would indicate. This discrepancy is most probably caused by two factors. Firstly, unlike stored pulses, propagating pulses don't benefit from the two nonlinearity-enhancing effects mentioned earlier in this section. Consequently, the nonlinearity they experience is weaker. Secondly, previous observations have indicated that the initial parts of pulses undergoing rEIT propagation exhibit minimal reduction in $g^{(2)}(0)$ [77, 78].

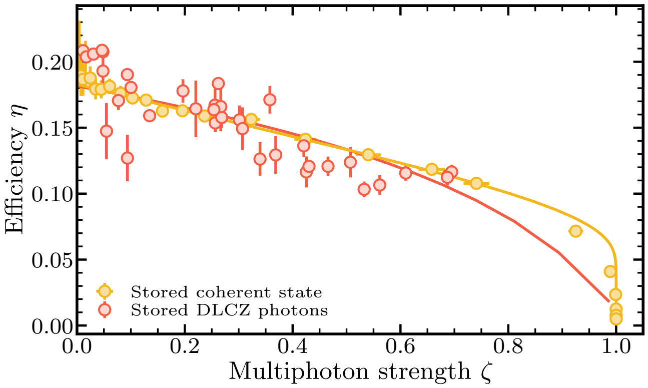

Figure 7.5: Rydberg memory efficiency as a function of multiphoton strength ζ for storage and retrieval of DLCZ photons (red circles) and WCS state (yellow circles). The solid lines of corresponding colors show the model prediction. The predicted faster efficiency decay for DLCZ photons at large ζ comes from the fact that the corresponding Fock state distribution has a longer tail towards higher-order multiphoton components than for WCS.

7.3.3 Effect of the partial blockade on the storage efficiency

Understanding the impact of the partial blockade on the pulse's Fock state distribution, we can re-examine the efficiency data and simulate its decay with respect to ζ. We start by describing how we model the effect of the blockade on the storage efficiency.

Once the Fock state distribution of the pulses post-blockade is determined, simulating the storage and retrieval efficiency is straightforward. One needs to account for two factors, the remaining linear losses during EIT propagation ($\sqrt{\eta_{\text{EIT}}} = \sqrt{0.6}$) and the retrieval efficiency ($\eta_r = 0.41$). This efficiency is deduced by matching the simulated efficiency with the experimental results at very low multiphoton strengths, where the influence of the blockade is negligible.

Given these considerations, the efficiency for the DLCZ photons can be calculated as:

$$\eta = \frac{\mu_s}{\mu_{\text{in}}} = \frac{\eta_r \sum_{k=0}^{\infty} k M_{kl}^{\sqrt{\text{EIT}}} p_l'}{\sum_{k=0}^{\infty} k M_{kl}^{\text{losses}} p_l} = \frac{\eta_r \sqrt{\eta_{\text{EIT}}} \sum_{k=0}^{\infty} k\, p_k'}{t_{\text{losses}} \sum_{k=0}^{\infty} k\, p_k}, \tag{7.12}$$

where the last equality comes from the linearity of the losses. Here, μ_{in} and μ_s denote the mean input and retrieved photon numbers, respectively. p_l and p_l' represent the elements of Fock state distributions as in eq. 7.11. We use the same method to estimate the storage and retrieval efficiency for coherent states.

The comparison between our simulations and the experimental data for both DLCZ photons and WCS is depicted in fig. 7.5. While our simulation aligns well with the WCS data, there's a some discrepancy for the DLCZ data at higher ζ values. This inconsistency likely stems from the uncertainty in determining ζ for this dataset. It's derived from the correspondence of ζ to the measured p_w, and accurate calibration of transmission losses of the write photon is crucial for its reliability[3].

It's worth noting that both models align with the experimental data for WCS and DLCZ photons, despite many parameters, like mean photon number, experimental rate or input $g^{(2)}_{\text{in}}(0)$, being very different. Given that these models focus exclusively on the input Fock state distribution, this suggests that the Rydberg medium's nonlinear response is determined by this distribution, which confirms the prevailing understanding of the Rydberg ensemble nonlinearity.

7.4 Conclusions and outlook

In this work, we employed a DLCZ quantum memory as a heralded source of non-classical light, examining its interplay with Rydberg nonlinearity during storage under EIT conditions in an atomic ensemble. This constitutes the first experiment where a non-classical state is stored in such a highly nonlinear medium, a crucial prerequisite for their applications in quantum networks. The photon's autocorrelation $g^{(2)}(0)$ was strongly reduced due to this interaction, demonstrating single photon filtering with quantum input light. With a simple simulation, we explained the role of partial blockade of the ensemble in this process. By comparing the results with quantum light and weak coherent states, we showed that the input Fock state distribution dictates the response of the medium, which aligns with established understandings of such systems. Our results show a proof of principle that correlated single photons can be stored in a Rydberg medium with single photon level nonlinearity. This represents a step towards the realization of photon-photon gates with true single photons.

---

[3] Such calibration concerns don't affect the $g^{(2)}_{\text{out}}(0)$ data, as ζ is determined from measured input $g^{(2)}_{\text{in}}(0)$, which is independent of the linear losses' calibration of the write photon.

Chapter 8

Conclusion & Outlook

The four-year duration of my PhD has been a significant and formative period in my life. It has provided ample opportunities for academic growth and personal development. Being surrounded by many smart people has not only fostered scientific discussions, but also offered valuable moments for broader conversations. Overall, this experience has played a crucial role in shaping me both professionally and personally.

During my PhD, we conducted a series of experiments utilizing strongly interacting Rydberg states in cold atomic ensembles to generate effective interactions among photons. Our work included a successful implementation of a building block of a quantum repeater with deterministic single-photon sources, where we explored the unique flexibility offered by Raman memory, which holds promise for future quantum repeater applications. Furthermore, we demonstrated for the first time the interaction and storage of single photons in a highly non-linear medium based on cold Rydberg atoms, marking a novel contribution in this field. Thanks to a Monte Carlo simulation, we got an intuitive understanding of the effect of the (partial) Rydberg blockade upon an arbitrary input Fock state distribution and confirmed that the medium's response depends solely on the input Fock state distribution. These results can be seen as a step towards realization of deterministic photon-photon gates based on Rydberg ensembles.

My work on the Rydberg system led me to a conclusion, that the physics of our Rydberg ensemble is very interesting, yet very complex. The presence of multiple Rydberg excitations make our system a complex many-body system. While significant progress has been made in explaining phenomena in this regime, there is still much to explore, and theoretical understanding remains an active area of research.

Given our group's focus on quantum repeaters, I believe it would be beneficial to rebuild our experiment so that one could work in the regimes where the physics is simpler or already well understood, while keeping in mind the ultimate goal of building a functional quantum repeater. In particular, this would require addressing the issue of short coherence time of Rydberg excitations.

There are two potential avenues for utilizing Rydberg ensembles in quantum repeaters. The first is a deterministic source of quantum light, i.e. single photons, entangled-photon pairs or light-matter entanglement. We have successfully achieved generation of single photons and demonstrated their quality through interference with DLCZ photons in a Hong–Ou–Mandel (HOM) experiment [231] (this experiment was performed while writing this thesis and, therefore, its results are not included here). Nevertheless, there is ample room for improvement, particularly in terms of generation efficiency and autocorrelation of the photons. The use of small, strongly blockaded ensembles has proven successful in this regard [62, 64]. By making slight adjustments to the setup, it would be possible to generate entangled photon pairs [65] or even photon trains [66], which are valuable resources for quantum repeaters. Another potential upgrades could be a ring cavity around the ensemble, significantly improving photon collection efficiency [70], or using a magical wavelength optical lattice to trap atoms continuously and suppress the motional dephasing [181]. Unfortunately, any of these improvements couldn't be implemented in the current setup due to the lack of space, what necessitates a major setup makeover.

With the enhanced setup, there is potential for extending the single-photon generation protocol to produce on-demand photon pairs at different wavelengths. This would involve transferring the Rydberg excitation, following the usual storage process, to a higher excited state carefully chosen to permit only one decay channel, resulting in the emission of two photons. An interesting candidate for this process is the state $\left|4D_{5/2}, F'' = 4\right\rangle$, which would yield photons at 780 nm and 1529 nm, corresponding to the transitions $\left|5S_{1/2}, F = 2\right\rangle \rightarrow \left|5P_{3/2}, F' = 3\right\rangle$ and $\left|5P_{3/2}, F' = 3\right\rangle \rightarrow \left|4D_{5/2}, F'' = 4\right\rangle$, respectively. A similar, but probabilistic protocol was already demonstrated in [232]. The aforementioned ring cavity could further improve the efficiency of this process by enhancing the first transition.

Rydberg ensembles also offer promising potential for quantum repeaters in the form of quantum gates, particularly the crucial CNOT gate for entanglement swapping. Unlike linear-optical CNOT gates, which have limited efficiency (typically to $1/9$ [64]), Rydberg-based gates provide the possibility for near-perfect efficiency. There are two possible avenues to explore for building such gates.

The first approach leverages the blockade effect [32, 39, 41, 42, 44, 47], requiring a small ensemble. This approach has the advantage that the gate fidelity is weakly dependent on experimental parameters [29, sec. 1A]. However, achieving high efficiency is difficult due to the need for photon storage, which remains an outstanding challenge. The highest efficiency photonic CNOT gate achieved so far, with 40 % efficiency, was primarily limited by the storage efficiency of the gate photon [49].

An alternative approach is to utilize interactions between counter-propagating Rydberg polaritons, which eliminates the need for photon storage and potentially offers higher efficiencies. However, in this case, the gate fidelity may depend on experimental parameters such as the Rabi frequency [40, 45], or require working with extremely dense ensembles [233] (if the protocol is extended to counter-propagating pulses). This approach would require a significantly larger ensemble than the blockade radius, which is in contrast to the requirement for efficient single-photon generation.

Nevertheless, it should be feasible to design a setup capable of generating an ensemble of two different sizes, potentially by adopting a geometry similar to previous works [82, sec. 5.3.4] or [234, sec. 3.5].

In summary, the field of Rydberg physics is a dynamic and captivating area of research, with a multitude of proposals and demonstrations contributing to the advancement of quantum technologies and the exploration of fundamental physics. Although many things have been understood and demonstrated, there is still a large room for scientific activity in this field.

Bibliography

1. Dowling, J. P. & Milburn, G. J. "Quantum Technology: The Second Quantum Revolution". *Philosophical Transactions of the Royal Society of London. Series A: Mathematical, Physical and Engineering Sciences* (2003) (cit. on p. 15).
2. "The Most Important Developments in Human History". Norwich University Online. `https://online.norwich.edu/academic-programs/resources/most-important-developments-human-history` (2023) (cit. on p. 15).
3. Kimble, H. J. "The Quantum Internet". *Nature* **453,** 1023–1030 (7198 2008) (cit. on pp. 15, 17).
4. Wehner, S., Elkouss, D. & Hanson, R. "Quantum Internet: A Vision for the Road Ahead". *Science* **362,** eaam9288 (2018) (cit. on p. 15).
5. Dieks, D. "Communication by EPR Devices". *Physics Letters A* **92,** 271–272 (1982) (cit. on p. 15).
6. Wootters, W. K. & Zurek, W. H. "A Single Quantum Cannot Be Cloned". *Nature* **299,** 802–803 (5886 1982) (cit. on p. 15).
7. Bennett, C. H. *et al.* "Teleporting an Unknown Quantum State via Dual Classical and Einstein-Podolsky-Rosen Channels". *Phys. Rev. Lett.* **70,** 1895–1899 (1993) (cit. on p. 16).
8. Pirandola, S., Laurenza, R., Ottaviani, C. & Banchi, L. "Fundamental Limits of Repeaterless Quantum Communications". *Nat Commun* **8,** 15043 (1 2017) (cit. on p. 16).
9. Briegel, H.-J., Dür, W., Cirac, J. I. & Zoller, P. "Quantum Repeaters: The Role of Imperfect Local Operations in Quantum Communication". *Phys. Rev. Lett.* **81,** 5932–5935 (1998) (cit. on p. 16).
10. Pan, J.-W., Bouwmeester, D., Weinfurter, H. & Zeilinger, A. "Experimental Entanglement Swapping: Entangling Photons That Never Interacted". *Phys. Rev. Lett.* **80,** 3891–3894 (1998) (cit. on p. 16).
11. Duan, L.-M., Lukin, M. D., Cirac, J. I. & Zoller, P. "Long-Distance Quantum Communication with Atomic Ensembles and Linear Optics". *Nature* **414,** 413–418 (2001) (cit. on pp. 16, 89, 104, 105).
12. Sangouard, N. *et al.* "Long-Distance Entanglement Distribution with Single-Photon Sources". *Phys. Rev. A* **76,** 050301 (2007) (cit. on pp. 16, 90, 100).
13. Sangouard, N. *et al.* "Robust and Efficient Quantum Repeaters with Atomic Ensembles and Linear Optics". *Phys. Rev. A* **77,** 062301 (2008) (cit. on p. 16).

14. Jiang, L. *et al.* "Quantum Repeater with Encoding". *Phys. Rev. A* **79,** 032325 (2009) (cit. on p. 16).
15. Sinclair, N. *et al.* "Spectral Multiplexing for Scalable Quantum Photonics Using an Atomic Frequency Comb Quantum Memory and Feed-Forward Control". *Phys. Rev. Lett.* **113,** 053603 (2014) (cit. on p. 16).
16. Krovi, H. *et al.* "Practical Quantum Repeaters with Parametric Down-Conversion Sources". *Appl. Phys. B* **122,** 52 (2016) (cit. on p. 16).
17. Collins, O. A., Jenkins, S. D., Kuzmich, A. & Kennedy, T. A. B. "Multiplexed Memory-Insensitive Quantum Repeaters". *Phys. Rev. Lett.* **98,** 060502 (2007) (cit. on p. 16).
18. Simon, C. *et al.* "Quantum Repeaters with Photon Pair Sources and Multimode Memories". *Phys. Rev. Lett.* **98,** 190503 (2007) (cit. on pp. 16, 105).
19. Wu, Y., Liu, J. & Simon, C. "Near-Term Performance of Quantum Repeaters with Imperfect Ensemble-Based Quantum Memories". *Phys. Rev. A* **101,** 042301 (2020) (cit. on p. 16).
20. Azuma, K., Tamaki, K. & Lo, H.-K. "All-Photonic Quantum Repeaters". *Nat Commun* **6,** 6787 (1 2015) (cit. on p. 16).
21. Calsamiglia, J. & Lütkenhaus, N. "Maximum Efficiency of a Linear-Optical Bell-state Analyzer". *Appl Phys B* **72,** 67–71 (2001) (cit. on pp. 16, 17).
22. Adams, C. S., Pritchard, J. D. & Shaffer, J. P. "Rydberg Atom Quantum Technologies". *J. Phys. B: At. Mol. Opt. Phys.* **53,** 012002. arXiv: `1907.09231` (2020) (cit. on pp. 16, 23).
23. Chang, D. E., Vuletić, V. & Lukin, M. D. "Quantum Nonlinear Optics — Photon by Photon". *Nature Photon* **8,** 685–694 (9 2014) (cit. on p. 17).
24. Knill, E., Laflamme, R. & Milburn, G. J. "A Scheme for Efficient Quantum Computation with Linear Optics". *Nature* **409,** 46–52 (6816 2001) (cit. on p. 17).
25. Reiserer, A. & Rempe, G. "Cavity-Based Quantum Networks with Single Atoms and Optical Photons". *Rev. Mod. Phys.* **87,** 1379–1418 (2015) (cit. on p. 17).
26. Firstenberg, O., Adams, C. S. & Hofferberth, S. "Nonlinear Quantum Optics Mediated by Rydberg Interactions". *J. Phys. B: At. Mol. Opt. Phys.* **49,** 152003 (2016) (cit. on pp. 18, 29, 31, 73, 106, 111, 112).
27. Gallagher, T. F. "Rydberg Atoms" 1st ed. (Cambridge University Press, 1994) (cit. on pp. 18, 21, 22).
28. Šibalić, N. & Adams, C. S. "Rydberg Physics" (IOP Publishing, 2018) (cit. on p. 18).
29. Saffman, M., Walker, T. G. & Mølmer, K. "Quantum Information with Rydberg Atoms". *Rev. Mod. Phys.* **82,** 2313–2363 (2010) (cit. on pp. 18, 22, 23, 118).
30. Browaeys, A. & Lahaye, T. "Many-Body Physics with Individually Controlled Rydberg Atoms". *Nat. Phys.* **16,** 132–142 (2020) (cit. on p. 18).
31. Morgado, M. & Whitlock, S. "Quantum Simulation and Computing with Rydberg-interacting Qubits". *AVS Quantum Science* **3,** 023501 (2021) (cit. on p. 18).
32. Lukin, M. D. *et al.* "Dipole Blockade and Quantum Information Processing in Mesoscopic Atomic Ensembles". *Phys. Rev. Lett.* **87,** 037901 (2001) (cit. on pp. 18, 28, 105, 106, 118).

33. Jaksch, D. *et al.* "Fast Quantum Gates for Neutral Atoms". *Phys. Rev. Lett.* **85,** 2208–2211 (2000) (cit. on p. 18).
34. Wilk, T. *et al.* "Entanglement of Two Individual Neutral Atoms Using Rydberg Blockade". *Phys. Rev. Lett.* **104,** 010502 (2010) (cit. on p. 18).
35. Isenhower, L. *et al.* "Demonstration of a Neutral Atom Controlled-NOT Quantum Gate". *Phys. Rev. Lett.* **104,** 010503 (2010) (cit. on p. 18).
36. Maller, K. M. *et al.* "Rydberg-Blockade Controlled-Not Gate and Entanglement in a Two-Dimensional Array of Neutral-Atom Qubits". *Phys. Rev. A* **92,** 022336 (2015) (cit. on p. 18).
37. Levine, H. *et al.* "Parallel Implementation of High-Fidelity Multiqubit Gates with Neutral Atoms". *Phys. Rev. Lett.* **123,** 170503 (2019) (cit. on p. 18).
38. Liu, Y., Li, L. & Ma, Y. "Hybrid Rydberg Quantum Gate for Quantum Network". *Phys. Rev. Res.* **4,** 013008 (2022) (cit. on p. 18).
39. Oh, E., Lai, X., Wen, J. & Du, S. "Distributed Quantum Computing with Photons and Atomic Memories". *Advanced Quantum Technologies* **6,** 2300007 (2023) (cit. on pp. 18, 118).
40. Friedler, I., Petrosyan, D., Fleischhauer, M. & Kurizki, G. "Long-Range Interactions and Entanglement of Slow Single-Photon Pulses". *Phys. Rev. A* **72,** 043803 (2005) (cit. on pp. 18, 118).
41. Gorshkov, A. V., Otterbach, J., Fleischhauer, M., Pohl, T. & Lukin, M. D. "Photon-Photon Interactions via Rydberg Blockade". *Phys. Rev. Lett.* **107,** 133602 (2011) (cit. on pp. 18, 36, 74, 118).
42. Paredes-Barato, D. & Adams, C. S. "All-Optical Quantum Information Processing Using Rydberg Gates". *Phys. Rev. Lett.* **112,** 040501 (2014) (cit. on pp. 18, 118).
43. Khazali, M., Heshami, K. & Simon, C. "Photon-Photon Gate via the Interaction between Two Collective Rydberg Excitations". *Phys. Rev. A* **91,** 030301 (2015) (cit. on p. 18).
44. Das, S. *et al.* "Photonic Controlled-Phase Gates through Rydberg Blockade in Optical Cavities". *Phys. Rev. A* **93,** 040303 (2016) (cit. on pp. 18, 118).
45. Bienias, P. & Buechler, H. P. "Two Photon Conditional Phase Gate Based on Rydberg Slow Light Polaritons". *J. Phys. B: At. Mol. Opt. Phys.* **53,** 054003. arXiv: `1909.04920 [cond-mat, physics:physics, physics:quant-ph]` (2020) (cit. on pp. 18, 118).
46. Guo, C.-Y., Yan, L.-L., Zhang, S., Su, S.-L. & Li, W. "Optimized Geometric Quantum Computation with a Mesoscopic Ensemble of Rydberg Atoms". *Phys. Rev. A* **102,** 042607 (2020) (cit. on p. 18).
47. Khazali, M. "All-Optical Quantum Information Processing via a Single-Step Rydberg Blockade Gate". *Opt. Express, OE* **31,** 13970–13980 (2023) (cit. on pp. 18, 118).
48. Tiarks, D., Schmidt-Eberle, S., Stolz, T., Rempe, G. & Dürr, S. "A Photon–Photon Quantum Gate Based on Rydberg Interactions". *Nature Phys* **15,** 124–126 (2019) (cit. on pp. 18, 28).
49. Stolz, T. *et al.* "Quantum-Logic Gate between Two Optical Photons with an Average Efficiency above 40%". *Phys. Rev. X* **12,** 021035 (2022) (cit. on pp. 18, 28, 118).

50. Baur, S., Tiarks, D., Rempe, G. & Dürr, S. "Single-Photon Switch Based on Rydberg Blockade". *Phys. Rev. Lett.* **112,** 073901 (2014) (cit. on pp. 18, 81).

51. Yu, Y.-C. *et al.* "Experimental Demonstration of Switching Entangled Photons Based on the Rydberg Blockade Effect". *Sci. China Phys. Mech. Astron.* **63,** 110312 (2020) (cit. on pp. 18, 103).

52. Gorniaczyk, H., Tresp, C., Schmidt, J., Fedder, H. & Hofferberth, S. "Single-Photon Transistor Mediated by Interstate Rydberg Interactions". *Phys. Rev. Lett.* **113,** 053601 (2014) (cit. on pp. 18, 28, 103).

53. Tiarks, D., Baur, S., Schneider, K., Dürr, S. & Rempe, G. "Single-Photon Transistor Using a Förster Resonance". *Phys. Rev. Lett.* **113,** 053602 (2014) (cit. on pp. 18, 28).

54. Tresp, C. *et al.* "Single-Photon Absorber Based on Strongly Interacting Rydberg Atoms". *Phys. Rev. Lett.* **117,** 223001 (2016) (cit. on p. 19).

55. Stiesdal, N. *et al.* "Controlled Multi-Photon Subtraction with Cascaded Rydberg Superatoms as Single-Photon Absorbers". *Nat Commun* **12,** 4328 (1 2021) (cit. on p. 19).

56. Saffman, M. & Walker, T. G. "Creating Single-Atom and Single-Photon Sources from Entangled Atomic Ensembles". *Phys. Rev. A* **66,** 065403 (2002) (cit. on pp. 19, 27).

57. Dudin, Y. O. & Kuzmich, A. "Strongly Interacting Rydberg Excitations of a Cold Atomic Gas". *Science* **336,** 887–889 (2012) (cit. on pp. 19, 28, 71, 90).

58. Peyronel, T. *et al.* "Quantum Nonlinear Optics with Single Photons Enabled by Strongly Interacting Atoms". *Nature* **488,** 57–60 (2012) (cit. on pp. 19, 35, 74, 106).

59. Li, L. & Kuzmich, A. "Quantum Memory with Strong and Controllable Rydberg-level Interactions". *Nat Commun* **7,** 13618 (2016) (cit. on pp. 19, 90).

60. Craddock, A. N. *et al.* "Quantum Interference between Photons from an Atomic Ensemble and a Remote Atomic Ion". *Phys. Rev. Lett.* **123,** 213601 (2019) (cit. on pp. 19, 70).

61. Bienias, P. *et al.* "Photon Propagation through Dissipative Rydberg Media at Large Input Rates". *Phys. Rev. Research* **2,** 033049 (2020) (cit. on pp. 19, 20, 71, 73–75, 106, 111, 112).

62. Ornelas-Huerta, D. P. *et al.* "On-Demand Indistinguishable Single Photons from an Efficient and Pure Source Based on a Rydberg Ensemble". *Optica, OPTICA* **7,** 813–819 (2020) (cit. on pp. 19, 28, 70, 90, 102, 118).

63. Ripka, F., Kübler, H., Löw, R. & Pfau, T. "A Room-Temperature Single-Photon Source Based on Strongly Interacting Rydberg Atoms". *Science* **362,** 446–449. pmid: `30361371` (2018) (cit. on p. 19).

64. Shi, S. *et al.* "High-Fidelity Photonic Quantum Logic Gate Based on near-Optimal Rydberg Single-Photon Source". *Nat Commun* **13,** 4454 (1 2022) (cit. on pp. 19, 28, 70, 118).

65. Sun, P.-F. *et al.* "Deterministic Time-Bin Entanglement between a Single Photon and an Atomic Ensemble". *Phys. Rev. Lett.* **128,** 060502 (2022) (cit. on pp. 19, 28, 118).

66. Yang, C.-W. *et al.* "Sequential Generation of Multiphoton Entanglement with a Rydberg Superatom". *Nat. Photon.* **16,** 658–661 (9 2022) (cit. on pp. 19, 118).

67. Ye, G.-S. *et al.* "A Photonic Entanglement Filter with Rydberg Atoms". *Nat. Photon.,* 1–6 (2023) (cit. on pp. 19, 28).

68. Spong, N. L. R. *et al.* "Collectively Encoded Rydberg Qubit". *Phys. Rev. Lett.* **127,** 063604 (2021) (cit. on pp. 19, 28).

69. Xu, W. *et al.* "Fast Preparation and Detection of a Rydberg Qubit Using Atomic Ensembles". *Phys. Rev. Lett.* **127,** 050501 (2021) (cit. on pp. 19, 28).

70. Yang, C.-W. *et al.* "Deterministic Measurement of a Rydberg Superatom Qubit via Cavity-Enhanced Single-Photon Emission". *Optica, OPTICA* **9,** 853–858 (2022) (cit. on pp. 19, 102, 118).

71. Mei, Y., Li, Y., Nguyen, H., Berman, P. R. & Kuzmich, A. "Trapped Alkali-Metal Rydberg Qubit". *Phys. Rev. Lett.* **128,** 123601 (2022) (cit. on p. 19).

72. Ornelas-Huerta, D. P. *et al.* "Tunable Three-Body Loss in a Nonlinear Rydberg Medium". *Phys. Rev. Lett.* **126,** 173401 (2021) (cit. on pp. 19, 36).

73. Liang, Q.-Y. *et al.* "Observation of Three-Photon Bound States in a Quantum Nonlinear Medium". *Science* **359,** 783–786 (2018) (cit. on pp. 19, 36).

74. Stiesdal, N. *et al.* "Observation of Three-Body Correlations for Photons Coupled to a Rydberg Superatom". *Phys. Rev. Lett.* **121,** 103601 (2018) (cit. on pp. 19, 36).

75. Gaj, A. *et al.* "From Molecular Spectra to a Density Shift in Dense Rydberg Gases". *Nat Commun* **5,** 4546 (1 2014) (cit. on pp. 19, 81).

76. Cantu, S. H. *et al.* "Repulsive Photons in a Quantum Nonlinear Medium". *Nat. Phys.* **16,** 921–925 (9 2020) (cit. on pp. 19, 36).

77. Möhl, C. *et al.* "Photon Correlation Transients in a Weakly Blockaded Rydberg Ensemble". *J. Phys. B: At. Mol. Opt. Phys.* **53,** 084005 (2020) (cit. on pp. 19, 33, 107, 111, 113).

78. Padrón-Brito, A. *et al.* "Transient Dynamics of the Quantum Light Retrieved from Rydberg Polaritons". *New J. Phys.* **23,** 063009 (2021) (cit. on pp. 19, 33, 72, 105, 107, 111, 113).

79. Li, Y., Mei, Y., Nguyen, H., Berman, P. R. & Kuzmich, A. "Dynamics of Collective-Dephasing-Induced Multiatom Entanglement". *Phys. Rev. A* **106,** L051701 (2022) (cit. on pp. 19, 71).

80. Distante, E., Padrón-Brito, A., Cristiani, M., Paredes-Barato, D. & de Riedmatten, H. "Storage Enhanced Nonlinearities in a Cold Atomic Rydberg Ensemble". *Phys. Rev. Lett.* **117,** 113001 (2016) (cit. on pp. 19, 36, 72, 105, 107, 111, 112).

81. Marinescu, M., Sadeghpour, H. R. & Dalgarno, A. "Dispersion Coefficients for Alkali-Metal Dimers". *Phys. Rev. A* **49,** 982–988 (1994) (cit. on p. 22).

82. Ornelas-Huerta, D. P. *Experiments with Strongly-Interacting Rydberg Atoms*. PhD thesis (University of Maryland, 2020) (cit. on pp. 22, 25, 29, 31, 34, 119).

83. Löw, R. *et al.* "An Experimental and Theoretical Guide to Strongly Interacting Rydberg Gases". *J. Phys. B: At. Mol. Opt. Phys.* **45,** 113001 (2012) (cit. on pp. 22, 23, 71).

84. Li, W., Mourachko, I., Noel, M. W. & Gallagher, T. F. "Millimeter-Wave Spectroscopy of Cold Rb Rydberg Atoms in a Magneto-Optical Trap: Quantum Defects of the Ns, Np, and Nd Series". *Phys. Rev. A* **67,** 052502 (2003) (cit. on p. 22).

85. Šibalić, N., Pritchard, J., Adams, C. & Weatherill, K. "ARC: An Open-Source Library for Calculating Properties of Alkali Rydberg Atoms". *Computer Physics Communications* **220,** 319–331 (2017) (cit. on p. 23).

86. Weber, S. *et al.* "Calculation of Rydberg Interaction Potentials". *J. Phys. B: At. Mol. Opt. Phys.* **50,** 133001 (2017) (cit. on pp. 23, 26, 106).

87. Browaeys, A., Barredo, D. & Lahaye, T. "Experimental Investigations of the Dipolar Interactions between Single Rydberg Atoms". *J. Phys. B: At. Mol. Opt. Phys.* **49,** 152001. arXiv: `1603.04603 [physics, physics:quant-ph]` (2016) (cit. on p. 22).

88. Walker, T. G. & Saffman, M. "Consequences of Zeeman Degeneracy for the van Der Waals Blockade between Rydberg Atoms". *Phys. Rev. A* **77,** 032723 (2008) (cit. on p. 23).

89. Nipper, J. *et al.* "Atomic Pair-State Interferometer: Controlling and Measuring an Interaction-Induced Phase Shift in Rydberg-Atom Pairs". *Phys. Rev. X* **2,** 031011 (2012) (cit. on p. 25).

90. Ryabtsev, I. I., Tretyakov, D. B., Beterov, I. I. & Entin, V. M. "Observation of the Stark-Tuned Förster Resonance between Two Rydberg Atoms". *Phys. Rev. Lett.* **104,** 073003 (2010) (cit. on p. 25).

91. Gorniaczyk, H. *et al.* "Enhancement of Rydberg-mediated Single-Photon Nonlinearities by Electrically Tuned Förster Resonances". *Nat Commun* **7,** 12480 (2016) (cit. on p. 25).

92. Maxwell, D. *et al.* "Storage and Control of Optical Photons Using Rydberg Polaritons". *Phys. Rev. Lett.* **110,** 103001 (2013) (cit. on pp. 25, 90).

93. Maxwell, D. *et al.* "Microwave Control of the Interaction between Two Optical Photons". *Phys. Rev. A* **89,** 043827 (2014) (cit. on p. 25).

94. Tretyakov, D. B. *et al.* "Controlling the Interactions of a Few Cold Rb Rydberg Atoms by Radio-Frequency-Assisted Forster Resonances". *Phys. Rev. A* **90,** 041403 (2014) (cit. on p. 25).

95. Bienias, P. *et al.* "Scattering Resonances and Bound States for Strongly Interacting Rydberg Polaritons". *Phys. Rev. A* **90,** 053804 (2014) (cit. on pp. 25, 74).

96. Bienias, P. *Few-Body Quantum Physics with Strongly Interacting Rydberg Polaritons*. PhD thesis (Universität Stuttgart, 2016) (cit. on p. 25).

97. Gaëtan, A. *et al.* "Observation of Collective Excitation of Two Individual Atoms in the Rydberg Blockade Regime". *Nature Physics* **5,** 115–118 (2009) (cit. on p. 26).

98. Gorshkov, A. V., André, A., Lukin, M. D. & Sørensen, A. S. "Photon Storage in Λ-type Optically Dense Atomic Media. II. Free-space Model". *Phys. Rev. A* **76,** 033805 (2007) (cit. on pp. 28, 100).

99. Mewes, C. & Fleischhauer, M. "Decoherence in Collective Quantum Memories for Photons". *Phys. Rev. A* **72,** 022327 (2005) (cit. on p. 28).

100. Paris-Mandoki, A. *et al.* "Free-Space Quantum Electrodynamics with a Single Rydberg Superatom". *Phys. Rev. X* **7,** 041010 (2017) (cit. on p. 28).

101. Vaneecloo, J., Garcia, S. & Ourjoumtsev, A. "Intracavity Rydberg Superatom for Optical Quantum Engineering: Coherent Control, Single-Shot Detection, and Optical π Phase Shift". *Phys. Rev. X* **12,** 021034 (2022) (cit. on p. 28).

102. Steck, D. A. *Quantum and Atom Optics*. lecture notes. 2022 (cit. on pp. 29, 31, 38, 39, 70, 78, 79, 83, 84).
103. Tresp, C. *Rydberg Polaritons and Rydberg Superatoms - Novel Tools for Quantum Nonlinear Optics*. PhD thesis (Universität Stuttgart, 2017) (cit. on p. 31).
104. Fleischhauer, M. & Lukin, M. D. "Dark-State Polaritons in Electromagnetically Induced Transparency". *Phys. Rev. Lett.* **84,** 5094–5097 (2000) (cit. on pp. 34, 35, 104).
105. Fleischhauer, M. & Lukin, M. D. "Quantum Memory for Photons: Dark-state Polaritons". *Phys. Rev. A* **65,** 022314 (2002) (cit. on pp. 34, 82).
106. Hsiao, Y.-F. *et al.* "Highly Efficient Coherent Optical Memory Based on Electromagnetically Induced Transparency". *Phys. Rev. Lett.* **120,** 183602 (2018) (cit. on p. 35).
107. Cao, M., Hoffet, F., Qiu, S., Sheremet, A. S. & Laurat, J. "Efficient Reversible Entanglement Transfer between Light and Quantum Memories". *Optica, OPTICA* **7,** 1440–1444 (2020) (cit. on pp. 35, 90, 96, 97, 102).
108. Dudin, Y. O., Li, L. & Kuzmich, A. "Light Storage on the Time Scale of a Minute". *Phys. Rev. A* **87,** 031801 (2013) (cit. on p. 35).
109. Pritchard, J. D. *et al.* "Cooperative Atom-Light Interaction in a Blockaded Rydberg Ensemble". *Phys. Rev. Lett.* **105,** 193603 (2010) (cit. on p. 35).
110. Petrosyan, D., Otterbach, J. & Fleischhauer, M. "Electromagnetically Induced Transparency with Rydberg Atoms". *Phys. Rev. Lett.* **107,** 213601 (2011) (cit. on pp. 36, 104).
111. Gorshkov, A. V., Nath, R. & Pohl, T. "Dissipative Many-Body Quantum Optics in Rydberg Media". *Phys. Rev. Lett.* **110,** 153601 (2013) (cit. on pp. 36, 74, 111).
112. Gärttner, M. & Evers, J. "Nonlinear Absorption and Density-Dependent Dephasing in Rydberg Electromagnetically-Induced-Transparency Media". *Phys. Rev. A* **88,** 033417 (2013) (cit. on p. 36).
113. Bienias, P. "Few-Body Quantum Physics with Strongly Interacting Rydberg Polaritons". *Eur. Phys. J. Spec. Top.* **225,** 2957–2976 (2016) (cit. on p. 36).
114. Firstenberg, O. *et al.* "Attractive Photons in a Quantum Nonlinear Medium". *Nature* **502,** 71–75 (7469 2013) (cit. on p. 36).
115. Tiarks, D., Schmidt, S., Rempe, G. & Dürr, S. "Optical Pi Phase Shift Created with a Single-Photon Pulse". *Sci. Adv.* **2,** e1600036 (2016) (cit. on p. 36).
116. Distante, E. *A Quantum Light-Matter Interface with Rydberg Polaritons in a Cold Atomic Ensemble*. PhD thesis (ICFO - The Institute of Photonic Sciences, 2017) (cit. on pp. 37, 38, 42, 44, 103).
117. Padrón-Brito, M. A. *Quantum Nonlinear Optics at the Single-Photon Level with Cold Rydberg Atoms*. PhD thesis (ICFO - The Institute of Photonic Sciences, 2021) (cit. on pp. 37, 38).
118. Foot, C. J. "Atomic Physics". *Oxford Master Series in Physics* **7. Atomic, Optical, and laser physics.** 331 pp. (Oxford University Press, Oxford ; New York, 2005) (cit. on pp. 38, 39).

119. Petrich, W., Anderson, M. H., Ensher, J. R. & Cornell, E. A. "Behavior of Atoms in a Compressed Magneto-Optical Trap". *J. Opt. Soc. Am. B, JOSAB* **11,** 1332–1335 (1994) (cit. on p. 39).

120. Weiss, D. S., Riis, E., Shevy, Y., Ungar, P. J. & Chu, S. "Optical Molasses and Multilevel Atoms: Experiment". *J. Opt. Soc. Am. B, JOSAB* **6,** 2072–2083 (1989) (cit. on p. 39).

121. Koschorreck, M. *Generation of Spin Squeezing in an Ensemble of Cold Rubidium 87*. PhD thesis (ICFO - The Institute of Photonic Sciences, 2010) (cit. on p. 42).

122. Appel, J., MacRae, A. & Lvovsky, A. I. "Versatile Digital GHz Phase Lock for External Cavity Diode Lasers". *Meas. Sci. Technol.* **20,** 055302. arXiv: `0809.3607 [physics, physics:quant-ph]` (2009) (cit. on p. 44).

123. McCarron, D. J., King, S. A. & Cornish, S. L. "Modulation Transfer Spectroscopy in Atomic Rubidium". *Meas. Sci. Technol.* **19,** 105601 (2008) (cit. on pp. 46–48).

124. Zhe Li, L., Eon Park, S., Noh, H.-R., Park, J.-D. & Cho, C.-H. "Modulation Transfer Spectroscopy for a Two-Level Atomic System with a Non-Cycling Transition". *J. Phys. Soc. Jpn.* **80,** 074301 (2011) (cit. on pp. 47, 48).

125. Raj, R. K., Bloch, D., Snyder, J. J., Camy, G. & Ducloy, M. "High-Frequency Optically Heterodyned Saturation Spectroscopy Via Resonant Degenerate Four-Wave Mixing". *Phys. Rev. Lett.* **44,** 1251–1254 (1980) (cit. on p. 47).

126. Negnevitsky, V. & Turner, L. D. "Wideband Laser Locking to an Atomic Reference with Modulation Transfer Spectroscopy". *Opt. Express, OE* **21,** 3103–3113 (2013) (cit. on p. 48).

127. Noh, H.-R., Park, S. E., Li, L. Z., Park, J.-D. & Cho, C.-H. "Modulation Transfer Spectroscopy for 87Rb Atoms: Theory and Experiment". *Opt. Express, OE* **19,** 23444–23452 (2011) (cit. on p. 48).

128. Preuschoff, T., Schlosser, M. & Birkl, G. "Optimization Strategies for Modulation Transfer Spectroscopy Applied to Laser Stabilization". *Opt. Express, OE* **26,** 24010–24019 (2018) (cit. on pp. 49, 50).

129. Lee, S. *et al.* "Compact Modulation Transfer Spectroscopy Module for Highly Stable Laser Frequency". *Optics and Lasers in Engineering* **146,** 106698 (2021) (cit. on pp. 49, 51, 52).

130. Wiegand, B., Leykauf, B., Jördens, R. & Krutzik, M. "Linien: A Versatile, User-Friendly, Open-Source FPGA-based Tool for Frequency Stabilization and Spectroscopy Parameter Optimization". *Review of Scientific Instruments* **93,** 063001 (2022) (cit. on p. 50).

131. Neuhaus, L. *et al.* "PyRPL (Python Red Pitaya Lockbox) — An Open-Source Software Package for FPGA-controlled Quantum Optics Experiments". in *2017 Conference on Lasers and Electro-Optics Europe & European Quantum Electronics Conference (CLEO/Europe-EQEC)* 2017 Conference on Lasers and Electro-Optics Europe & European Quantum Electronics Conference (CLEO/Europe-EQEC) (IEEE, Munich, Germany, 2017), 1–1 (cit. on p. 50).

132. Luda, M. A., Drechsler, M., Schmiegelow, C. T. & Codnia, J. "Compact Embedded Device for Lock-in Measurements and Experiment Active Control". *Review of Scientific Instruments* **90,** 023106 (2019) (cit. on p. 50).

133. Jaatinen, E., Hopper, D. J. & Back, J. "Residual Amplitude Modulation Mechanisms in Modulation Transfer Spectroscopy That Use Electro-Optic Modulators". *Meas. Sci. Technol.* **20,** 025302 (2008) (cit. on p. 51).
134. Jaatinen, E. & Hopper, D. J. "Compensating for Frequency Shifts in Modulation Transfer Spectroscopy Caused by Residual Amplitude Modulation". *Optics and Lasers in Engineering* **46,** 69–74 (2008) (cit. on p. 51).
135. Long, J.-B., Yang, S.-J., Chen, S. & Pan, J.-W. "Magnetic-Enhanced Modulation Transfer Spectroscopy and Laser Locking for ^{87}Rb Repump Transition". *Opt. Express, OE* **26,** 27773–27786 (2018) (cit. on p. 51).
136. Stremler, F. G. "Introduction to Communication Systems" 3rd ed. 757 pp. (Addison-Wesley Pub. Co, Reading, Mass, 1990) (cit. on p. 53).
137. Black, E. D. "An Introduction to Pound–Drever–Hall Laser Frequency Stabilization". *American Journal of Physics* **69,** 79–87 (2001) (cit. on p. 53).
138. Nagourney, W. G. "Quantum Electronics for Atomic Physics". 381 pp. (Oxford University Press, Oxford ; New York, 2010) (cit. on p. 53).
139. Noël, V. P. *et al.* "Tools and Tutorial on Practical Ray Tracing for Microscopy". *Neurophotonics* **8,** 010801 (2021) (cit. on p. 54).
140. Pisenti, N. C., Restelli, A., Reschovsky, B. J., Barker, D. S. & Campbell, G. K. "An Ultra-Low Noise, High-Voltage Piezo-Driver". *Review of Scientific Instruments* **87,** 124702 (2016) (cit. on p. 54).
141. De Hond, J., Cisternas, N., Lochead, G. & van Druten, N. J. "Medium-Finesse Optical Cavity for the Stabilization of Rydberg Lasers". *Appl. Opt.* **56,** 5436 (2017) (cit. on p. 55).
142. Bi, J., Zhi, Y., Li, L. & Chen, L. "Suppressing Residual Amplitude Modulation to the 10\^{-7} Level in Optical Phase Modulation". *Appl. Opt., AO* **58,** 690–694 (2019) (cit. on p. 55).
143. Shen, H., Li, L., Bi, J., Wang, J. & Chen, L. "Systematic and Quantitative Analysis of Residual Amplitude Modulation in Pound-Drever-Hall Frequency Stabilization". *Phys. Rev. A* **92,** 063809 (2015) (cit. on p. 55).
144. Li, Z., Ma, W., Yang, W., Wang, Y. & Zheng, Y. "Reduction of Zero Baseline Drift of the Pound–Drever–Hall Error Signal with a Wedged Electro-Optical Crystal for Squeezed State Generation". *Opt. Lett., OL* **41,** 3331–3334 (2016) (cit. on p. 55).
145. Thorpe, J. I., Numata, K. & Livas, J. "Laser Frequency Stabilization and Control through Offset Sideband Locking to Optical Cavities". *Opt. Express* **16,** 15980 (2008) (cit. on p. 56).
146. Diehl, J. F., Sunderman, C. E., Singley, J. M., Urick, V. J. & Williams, K. J. "Control of Residual Amplitude Modulation in Lithium Niobate Phase Modulators". *Opt. Express, OE* **25,** 32985–32994 (2017) (cit. on p. 57).
147. Li, Z. *et al.* "Investigation and Cancellation of Residual Amplitude Modulation in Fiber Electro-Optic Modulator Based Frequency Modulation Gas Sensing Technique". *Sensors and Actuators B: Chemical* **196,** 23–30 (2014) (cit. on p. 57).
148. Yu, Y., Wang, Y. & Pratt, J. R. "Active Cancellation of Residual Amplitude Modulation in a Frequency-Modulation Based Fabry-Perot Interferometer". *Review of Scientific Instruments* **87,** 033101 (2016) (cit. on p. 57).

149. Steck, D. A. "Rubidium 87 D Line Data". 2015 (cit. on p. 58).
150. Loudon, R. "The Quantum Theory of Light" 3rd ed. 438 pp. (Oxford University Press, Oxford ; New York, 2000) (cit. on pp. 59–61).
151. Fox, M. "Quantum Optics: An Introduction". *Oxford Master Series in Physics* **15.** 378 pp. (Oxford University Press, Oxford ; New York, 2006) (cit. on p. 60).
152. Zou, X. T. & Mandel, L. "Photon-Antibunching and Sub-Poissonian Photon Statistics". *Phys. Rev. A* **41,** 475–476 (1990) (cit. on p. 60).
153. Zappa, F., Tisa, S., Tosi, A. & Cova, S. "Principles and Features of Single-Photon Avalanche Diode Arrays". *Sensors and Actuators A: Physical* **140,** 103–112 (2007) (cit. on p. 64).
154. "Single-Photon Generation and Detection: Experimental Methods in the Physical Sciences" (eds Migdall, A., Polyakov, S., Fan, J. & Bienfang, J.) *Experimental Methods in the Physical Sciences* **volume 45.** 569 pp. (Elsevier/AP, Academic Press is an imprint of Elsevier, Amsterdam ; Boston, 2013) (cit. on pp. 64, 66).
155. Cakste, A. & Andrae, M. *Statistical Analysis of Dark Counts in Superconducting Nanowire Single Photon Detectors*. MA thesis (KTH Royal Institute of Technology, 2022) (cit. on p. 65).
156. Humer, G. *et al.* "A Simple and Robust Method for Estimating Afterpulsing in Single Photon Detectors". *Journal of Lightwave Technology* **33,** 3098–3107 (2015) (cit. on pp. 65, 66).
157. Autebert, C. *et al.* "Direct Measurement of the Recovery Time of Superconducting Nanowire Single-Photon Detectors". *Journal of Applied Physics* **128,** 074504 (2020) (cit. on p. 66).
158. Burenkov, V., Xu, H., Qi, B., Hadfield, R. H. & Lo, H.-K. "Investigations of Afterpulsing and Detection Efficiency Recovery in Superconducting Nanowire Single-Photon Detectors". *Journal of Applied Physics* **113,** 213102 (2013) (cit. on p. 66).
159. Raupach, S. M. F., Sidorova, M. & Semenov, A. D. "Photon-Number Dependent Afterpulsing in Superconducting Nanostrip Single-Photon Detectors". arXiv: `2303.17861 [cond-mat, physics:physics]`. `http://arxiv.org/abs/2303.17861` (2023). preprint (cit. on p. 66).
160. Meda, A. *et al.* "Quantifying Backflash Radiation to Prevent Zero-Error Attacks in Quantum Key Distribution". *Light Sci Appl* **6,** e16261–e16261 (6 2017) (cit. on p. 66).
161. Pinheiro, P. V. P. *et al.* "Eavesdropping and Countermeasures for Backflash Side Channel in Quantum Cryptography". *Opt. Express, OE* **26,** 21020–21032 (2018) (cit. on p. 66).
162. De Léséleuc, S., Barredo, D., Lienhard, V., Browaeys, A. & Lahaye, T. "Analysis of Imperfections in the Coherent Optical Excitation of Single Atoms to Rydberg States". *Phys. Rev. A* **97,** 053803 (2018) (cit. on pp. 70, 83, 84).
163. Beterov, I. I. *et al.* "Deterministic Single-Atom Excitation via Adiabatic Passage and Rydberg Blockade". *Phys. Rev. A* **84,** 023413 (2011) (cit. on p. 70).
164. Beterov, I. I. *et al.* "Quantum Gates in Mesoscopic Atomic Ensembles Based on Adiabatic Passage and Rydberg Blockade". *Phys. Rev. A* **88,** 010303 (2013) (cit. on p. 70).

165. Zhou, M.-T. *et al.* "Experimental Creation of Single Rydberg Excitations via Adiabatic Passage". *Phys. Rev. A* **102,** 013706 (2020) (cit. on p. 70).

166. Petrosyan, D. & Mølmer, K. "Stimulated Adiabatic Passage in a Dissipative Ensemble of Atoms with Strong Rydberg-state Interactions". *Phys. Rev. A* **87,** 033416 (2013) (cit. on p. 70).

167. Li, J. *et al.* "Semideterministic Entanglement between a Single Photon and an Atomic Ensemble". *Phys. Rev. Lett.* **123,** 140504 (2019) (cit. on pp. 70, 90).

168. Bariani, F., Goldbart, P. M. & Kennedy, T. A. B. "Dephasing Dynamics of Rydberg Atom Spin Waves". *Phys. Rev. A* **86,** 041802 (2012) (cit. on pp. 71, 80).

169. Bariani, F. & Kennedy, T. A. B. "Retrieval of Multiple Spin Waves from a Weakly Excited, Metastable Atomic Ensemble". *Phys. Rev. A* **85,** 033811 (2012) (cit. on pp. 71, 80).

170. Vitanov, N. V. *et al.* "Power Broadening Revisited: Theory and Experiment". *Optics Communications* **199,** 117–126 (2001) (cit. on p. 71).

171. Zeuthen, E., Gullans, M. J., Maghrebi, M. F. & Gorshkov, A. V. "Correlated Photon Dynamics in Dissipative Rydberg Media". *Phys. Rev. Lett.* **119,** 043602 (2017) (cit. on pp. 71, 73, 111, 112).

172. Busche, H. *et al.* "Contactless Nonlinear Optics Mediated by Long-Range Rydberg Interactions". *Nature Phys* **13,** 655–658 (2017) (cit. on pp. 73, 111).

173. Sadler, D. P. *et al.* "Radiation Trapping in a Dense Cold Rydberg Gas". *Phys. Rev. A* **95,** 013839 (2017) (cit. on p. 73).

174. Padrón-Brito, A., Lowinski, J., Farrera, P., Theophilo, K. & de Riedmatten, H. "Probing the Indistinguishability of Single Photons Generated by Rydberg Atomic Ensembles". *Phys. Rev. Research* **3,** 033287 (2021) (cit. on pp. 74, 90, 106, 135).

175. Baur, S. E. *A Single-Photon Switch and Transistor Based on Rydberg Blockade*. PhD thesis (Technischen Universitat Munchen, 2014) (cit. on pp. 76, 81).

176. Hoffet, F. *Highly-Efficient Entanglement Transfer into and out of Cold-Atom Quantum Memories*. PhD thesis (Sorbonne Université, 2022) (cit. on p. 76).

177. Schmidt-Eberle, S., Stolz, T., Rempe, G. & Dürr, S. "Dark-Time Decay of the Retrieval Efficiency of Light Stored as a Rydberg Excitation in a Noninteracting Ultracold Gas". *Phys. Rev. A* **101,** 013421 (2020) (cit. on pp. 77, 80, 83, 87).

178. Albrecht, B. *Quantum Control of Single Spin Excitations in Cold Atomic Quantum Memories*. PhD thesis (ICFO - The Institute of Photonic Sciences, 2015) (cit. on p. 77).

179. Peyronel, T. (M. M. *Quantum Nonlinear Optics Using Cold Atomic Ensembles*. PhD thesis (Massachusetts Institute of Technology, 2013) (cit. on p. 77).

180. Li, L., Dudin, Y. O. & Kuzmich, A. "Entanglement between Light and an Optical Atomic Excitation". *Nature* **498,** 466–469 (2013) (cit. on pp. 80, 90).

181. Lampen, J., Nguyen, H., Li, L., Berman, P. R. & Kuzmich, A. "Long-Lived Coherence between Ground and Rydberg Levels in a Magic-Wavelength Lattice". *Phys. Rev. A* **98,** 033411 (2018) (cit. on pp. 80, 87, 118).

182. Agarwal, G. S. "Exact Solution for the Influence of Laser Temporal Fluctuations on Resonance Fluorescence". *Phys. Rev. Lett.* **37,** 1383–1386 (1976) (cit. on p. 81).

183. Agarwal, G. S. "Quantum Statistical Theory of Optical-Resonance Phenomena in Fluctuating Laser Fields". *Phys. Rev. A* **18,** 1490–1506 (1978) (cit. on p. 81).
184. Hotter, C., Plankensteiner, D. & Ritsch, H. "Continuous Narrowband Lasing with Coherently Driven V-level Atoms". *New J. Phys.* **22,** 113021 (2020) (cit. on p. 81).
185. Fleischhauer, M., Imamoglu, A. & Marangos, J. P. "Electromagnetically Induced Transparency: Optics in Coherent Media". *Rev. Mod. Phys.* **77,** 633–673 (2005) (cit. on p. 81).
186. Vaneecloo, J. *Nonlinear Quantum Optics with a Single Rydberg Superatom Coupled to a Medium-Finesse Cavity*. PhD thesis (Sorbonne Université, 2022) (cit. on pp. 82, 85).
187. Deutsch, I. H. *Three-Level Atoms: Adiabatic Elimination*. lecture notes. University of New Mexico, 2019 (cit. on p. 84).
188. McGuirk, J. M., Foster, G. T., Fixler, J. B., Snadden, M. J. & Kasevich, M. A. "Sensitive Absolute-Gravity Gradiometry Using Atom Interferometry". *Phys. Rev. A* **65,** 033608 (2002) (cit. on p. 85).
189. Dudin, Y. O., Li, L., Bariani, F. & Kuzmich, A. "Observation of Coherent Many-Body Rabi Oscillations". *Nature Phys* **8,** 790–794 (2012) (cit. on pp. 85, 86).
190. Heller, L., Lowinski, J., Theophilo, K., Padrón-Brito, A. & de Riedmatten, H. "Raman Storage of Quasideterministic Single Photons Generated by Rydberg Collective Excitations in a Low-Noise Quantum Memory". *Phys. Rev. Applied* **18,** 024036 (2022) (cit. on pp. 89, 135).
191. Yu, Y. *et al. Measurement-Device-Independent Verification of a Quantum Memory*. 2021. arXiv: `2104.14723 [physics, physics:quant-ph]` (cit. on p. 89).
192. Chou, C. W. *et al.* "Measurement-Induced Entanglement for Excitation Stored in Remote Atomic Ensembles". *Nature* **438,** 828–832 (7069 2005) (cit. on p. 89).
193. Chou, C.-W. *et al.* "Functional Quantum Nodes for Entanglement Distribution over Scalable Quantum Networks". *Science* **316,** 1316–1320 (2007) (cit. on p. 89).
194. Felinto, D. *et al.* "Conditional Control of the Quantum States of Remote Atomic Memories for Quantum Networking". *Nature Phys* **2,** 844–848 (12 2006) (cit. on p. 89).
195. Yu, Y. *et al.* "Entanglement of Two Quantum Memories via Fibres over Dozens of Kilometres". *Nature* **578,** 240–245 (7794 2020) (cit. on p. 89).
196. Yuan, Z.-S. *et al.* "Experimental Demonstration of a BDCZ Quantum Repeater Node". *Nature* **454,** 1098–1101 (7208 2008) (cit. on p. 89).
197. Lago-Rivera, D., Grandi, S., Rakonjac, J. V., Seri, A. & de Riedmatten, H. "Telecom-Heralded Entanglement between Multimode Solid-State Quantum Memories". *Nature* **594,** 37–40 (7861 2021) (cit. on p. 89).
198. Liu, X. *et al.* "Heralded Entanglement Distribution between Two Absorptive Quantum Memories". *Nature* **594,** 41–45 (7861 2021) (cit. on p. 89).
199. Sangouard, N., Simon, C., de Riedmatten, H. & Gisin, N. "Quantum Repeaters Based on Atomic Ensembles and Linear Optics". *Rev. Mod. Phys.* **83,** 33–80 (2011) (cit. on pp. 90, 106).

200. Ding, D.-S. *et al.* "Raman Quantum Memory of Photonic Polarized Entanglement". *Nature Photon* **9,** 332–338 (5 2015) (cit. on pp. 90, 96, 97).

201. Seri, A. *et al.* "Quantum Correlations between Single Telecom Photons and a Multimode On-Demand Solid-State Quantum Memory". *Phys. Rev. X* **7,** 021028 (2017) (cit. on pp. 90, 97).

202. Wang, Y. *et al.* "Efficient Quantum Memory for Single-Photon Polarization Qubits". *Nat. Photonics* **13,** 346–351 (5 2019) (cit. on p. 90).

203. Akopian, N., Wang, L., Rastelli, A., Schmidt, O. G. & Zwiller, V. "Hybrid Semiconductor-Atomic Interface: Slowing down Single Photons from a Quantum Dot". *Nature Photon* **5,** 230–233 (4 2011) (cit. on p. 90).

204. Kroh, T. *et al.* "Slow and Fast Single Photons from a Quantum Dot Interacting with the Excited State Hyperfine Structure of the Cesium D1-line". *Sci Rep* **9,** 13728 (1 2019) (cit. on p. 90).

205. Siyushev, P., Stein, G., Wrachtrup, J. & Gerhardt, I. "Molecular Photons Interfaced with Alkali Atoms". *Nature* **509,** 66–70 (7498 2014) (cit. on p. 90).

206. Tang, J.-S. *et al.* "Storage of Multiple Single-Photon Pulses Emitted from a Quantum Dot in a Solid-State Quantum Memory". *Nat Commun* **6,** 8652 (1 2015) (cit. on p. 90).

207. Lettner, M. *et al.* "Remote Entanglement between a Single Atom and a Bose-Einstein Condensate". *Phys. Rev. Lett.* **106,** 210503 (2011) (cit. on p. 90).

208. Nunn, J. *et al.* "Mapping Broadband Single-Photon Wave Packets into an Atomic Memory". *Phys. Rev. A* **75,** 011401 (2007) (cit. on pp. 92, 100).

209. Albrecht, B., Farrera, P., Heinze, G., Cristiani, M. & de Riedmatten, H. "Controlled Rephasing of Single Collective Spin Excitations in a Cold Atomic Quantum Memory". *Phys. Rev. Lett.* **115,** 160501 (2015) (cit. on p. 96).

210. Lettner, M. *Ein Bose-Einstein-Kondensat Als Quantenspeicher Für Zwei-Teilchen-Verschränkung.* PhD thesis (Technische Universität München, 2011) (cit. on pp. 96, 97).

211. Saglamyurek, E., Hrushevskyi, T., Cooke, L., Rastogi, A. & LeBlanc, L. J. "Single-Photon-Level Light Storage in Cold Atoms Using the Autler-Townes Splitting Protocol". *Phys. Rev. Res.* **1,** 022004 (2019) (cit. on pp. 96, 97).

212. Saglamyurek, E. *et al.* "Storing Short Single-Photon-Level Optical Pulses in Bose–Einstein Condensates for High-Performance Quantum Memory". *New J. Phys.* **23,** 043028 (2021) (cit. on pp. 96, 97).

213. Wolters, J. *et al.* "Simple Atomic Quantum Memory Suitable for Semiconductor Quantum Dot Single Photons". *Phys. Rev. Lett.* **119,** 060502 (2017) (cit. on p. 97).

214. Thomas, S. E. *et al.* "Raman Quantum Memory with Built-in Suppression of Four-Wave-Mixing Noise". *Phys. Rev. A* **100,** 033801 (2019) (cit. on p. 97).

215. Namazi, M., Kupchak, C., Jordaan, B., Shahrokhshahi, R. & Figueroa, E. "Ultralow-Noise Room-Temperature Quantum Memory for Polarization Qubits". *Phys. Rev. Appl.* **8,** 034023 (2017) (cit. on p. 97).

216. Gündoğan, M., Ledingham, P. M., Kutluer, K., Mazzera, M. & de Riedmatten, H. "Solid State Spin-Wave Quantum Memory for Time-Bin Qubits". *Phys. Rev. Lett.* **114,** 230501 (2015) (cit. on p. 97).

217. Maring, N. *et al.* "Photonic Quantum State Transfer between a Cold Atomic Gas and a Crystal". *Nature* **551,** 485–488 (7681 2017) (cit. on p. 98).
218. Hong, C. K., Ou, Z. Y. & Mandel, L. "Measurement of Subpicosecond Time Intervals between Two Photons by Interference". *Phys. Rev. Lett.* **59,** 2044–2046 (1987) (cit. on p. 99).
219. Legero, T., Wilk, T., Kuhn, A. & Rempe, G. "Time-Resolved Two-Photon Quantum Interference". *Appl. Phys. B* **77,** 797–802 (2003) (cit. on p. 99).
220. Reim, K. F. *et al.* "Multipulse Addressing of a Raman Quantum Memory: Configurable Beam Splitting and Efficient Readout". *Phys. Rev. Lett.* **108,** 263602 (2012) (cit. on p. 100).
221. Sheremet, A. S. *et al.* "Quantum Memory for Light via a Stimulated Off-Resonant Raman Process: Beyond the Three-Level Λ-scheme Approximation". *Phys. Rev. A* **82,** 033838 (2010) (cit. on p. 100).
222. Vernaz-Gris, P. *et al.* "High-Performance Raman Memory with Spatio-Temporal Reversal". *Opt. Express, OE* **26,** 12424–12431 (2018) (cit. on pp. 100, 102).
223. Chen, Y.-H. *et al.* "Coherent Optical Memory with High Storage Efficiency and Large Fractional Delay". *Phys. Rev. Lett.* **110,** 083601 (2013) (cit. on p. 100).
224. Farrera, P. *et al.* "Generation of Single Photons with Highly Tunable Wave Shape from a Cold Atomic Ensemble". *Nat Commun* **7,** 13556 (2016) (cit. on p. 101).
225. Nunn, J. *Quantum Memory in Atomic Ensembles.* MA thesis (University of Bath, 2008) (cit. on p. 101).
226. Heller, L., Farrera, P., Heinze, G. & de Riedmatten, H. "Cold-Atom Temporally Multiplexed Quantum Memory with Cavity-Enhanced Noise Suppression". *Phys. Rev. Lett.* **124,** 210504 (2020) (cit. on p. 102).
227. Pu, Y.-F. *et al.* "Experimental Realization of a Multiplexed Quantum Memory with 225 Individually Accessible Memory Cells". *Nat Commun* **8,** 15359 (1 2017) (cit. on p. 102).
228. Wang, X.-J. *et al.* "Cavity-Enhanced Atom-Photon Entanglement with Subsecond Lifetime". *Phys. Rev. Lett.* **126,** 090501 (2021) (cit. on p. 102).
229. Lowinski, J. *et al.* "Strongly Non-Linear Interaction between Non-Classical Light and a Blockaded Rydberg Atomic Ensemble". arXiv: `2309.08257 [quant-ph]`. `http://arxiv.org/abs/2309.08257` (2023). preprint (cit. on pp. 103, 135).
230. Hammerer, K., Sørensen, A. S. & Polzik, E. S. "Quantum Interface between Light and Atomic Ensembles". *Rev. Mod. Phys.* **82,** 1041–1093 (2010) (cit. on p. 105).
231. Hoffet, F., Lowinski, J., Heller, L. & Riedmatten, H. de. *Almost Perfect Indistinguishability between Single Photons Emitted from Different Atomic Ensemble Quantum Nodes.* in preparation. 2023 (cit. on pp. 118, 135).
232. Chanelière, T. *et al.* "Quantum Telecommunication Based on Atomic Cascade Transitions". *Phys. Rev. Lett.* **96,** 093604 (2006) (cit. on p. 118).
233. Thompson, J. D. *et al.* "Symmetry-Protected Collisions between Strongly Interacting Photons". *Nature* **542,** 206–209 (7640 2017) (cit. on p. 118).
234. Stiesdal, N. *Collective Atom-Light Interactions with Rydberg Superatoms.* PhD thesis (University of Southern Denmark, 2022) (cit. on p. 119).

Publication list

Publications arising from this work

Heller, L., Lowinski, J., Theophilo, K., Padrón-Brito, A. & de Riedmatten, H. "Raman Storage of Quasideterministic Single Photons Generated by Rydberg Collective Excitations in a Low-Noise Quantum Memory". *Phys. Rev. Applied* **18,** 024036 (2022)[1]

Lowinski, J., Heller, L., Hoffet, F., Padrón-Brito, A., Theophilo, K. & de Riedmatten, H. "Strongly Non-Linear Interaction between Non-Classical Light and a Blockaded Rydberg Atomic Ensemble". arXiv: `2309.08257 [quant-ph]`. `http://arxiv.org/abs/2309.08257` (2023). preprint[2]

Related publications

Padrón-Brito, A., Lowinski, J., Farrera, P., Theophilo, K. & de Riedmatten, H. "Probing the Indistinguishability of Single Photons Generated by Rydberg Atomic Ensembles". *Phys. Rev. Research* **3,** 033287 (2021)

Hoffet, F., Lowinski, J., Heller, L. & Riedmatten, H. de. *Almost Perfect Indistinguishability between Single Photons Emitted from Different Atomic Ensemble Quantum Nodes.* in preparation. 2023[3]

---

[1] L.H. and J.L. contributed equally to this work.

[2] L.H. and J.L. contributed equally to this work.

[3] F.H. and J.L. contributed equally to this work.